Towards a tool for diabetic foot diagnosis using a 3D modeling based on thermographic and visible spectrum images

Rafael Bayareh-Mancilla

Rafael Bayareh-Mancilla. Towards a tool for diabetic foot diagnosis using a 3D modeling based on thermographic and visible spectrum images. Automatic. Université de Lorraine; Centro de Investigación y de Estudios Avanzados del Instituto Politécnico Nacional (Mexico), 2022. English. NNT : 2022LORR0142 . tel-03855749

HAL Id: tel-03855749

https://hal.univ-lorraine.fr/tel-03855749

Submitted on 16 Nov 2022

IAEM ED-77
Centre de Recherche en Automatique de Nancy - CRAN

CENTRO DE INVESTIGACIÓN Y DE ESTUDIOS AVANZADOS DEL INSTITUTO POLITÉCNICO NACIONAL

Thèse

Présentée et soutenue publiquement pour l'obtention du titre de

DOCTEUR DE l'UNIVERSITE DE LORRAINE

Mention : **Automatique, Traitement du Signal et des Images, Génie Informatique**

par **Rafael BAYAREH-MANCILLA**

Sous la direction de **VERA-HERNÁNDEZ**

Towards a Tool for Diabetic Foot Diagnosis using a 3D Modeling Based on Thermographic and Visible Spectrum Images

Présentée et soutenue le 5 octobre 2022

Membres du jury :

Directeur(s) de thèse :	M. Arturo VERA-HERNANDEZ	Professeur, Centro de Investigación y de Estudios Avanzados del IPN, Unidad Zacatenco, Mexique
Co-Directeur de thèse :	M. Didier WOLF	PU, Université de Lorraine, CRAN
Président de jury	M. Christian DAUL	PU, Université de Lorraine, CRAN
Rapporteurs	M. Wilfrido GÓMEZ-FLORES	Professeur, Centro de Investigación y de Estudios Avanzados del IPN, Unidad Tamaulipas, Mexique
	M. Mouloud ADEL	Professeur Institut Fresnel UMR-CNRS 7249. Enseignant au Département Informatique et Interactions de l'UFR Sciences. Faculté des Sciences et Techniques de Saint Jérôme, Marseille
Examinateurs	Mme. Josefina GUTIÉRREZ-MARTÍNEZ	PhD, Instituto Nacional de Rehabilitación, Mexique
	M. Lorenzo LEIJA-SALAS	Professeur, Centro de Investigación y de Estudios Avanzados del IPN, Unidad Zacatenco, Mexique
	M. Sergio Arturo CUEVAS-RODRÍGUEZ	Chercheur du groupe coopératif sur le cancer du sein de la société mexicaine d'oncologie.

CENTER FOR RESEARCH AND ADVANCED
STUDIES OF THE NATIONAL POLYTECHNIC INSTITUTE

CAMPUS ZACATENCO
ELECTRICAL ENGINEERING DEPARTMENT
BIOELECTRONICS SECTION

Towards a Tool for Diabetic Foot Diagnosis using a 3D Modeling Based on Thermographic and Visible Spectrum Images

Thesis presented by

Rafael Bayareh Mancilla

to obtain the Degree of

Doctor in Science

in the Specialty of

Electrical Engineering

Thesis Directors

Dr. Arturo Vera Hernández
Dr. Didier Wolf

Mexico City October 2022

CENTRO DE INVESTIGACIÓN Y DE ESTUDIOS
AVANZADOS DEL INSTITUTO POLITÉCNICO NACIONAL

UNIDAD ZACATENCO
DEPARTAMENTO DE INGENIERÍA ELÉCTRICA
SECCIÓN DE BIOELECTRÓNICA

Una herramienta para el diagnóstico del pie diabético mediante un modelado 3D basado en imágenes termográficas y de espectro visible

Tesis que presenta

Rafael Bayareh Mancilla

para obtener el Grado de

Doctor en Ciencias

en la Especialidad de

Ingeniería Eléctrica

Directores de tesis

Dr. Arturo Vera Hernández
Dr. Didier Wolf

Ciudad de México Octubre 2022

Acknowledgment

In the name of Allah, the most gracious and the most merciful. First and foremost, I am thankful to Almighty Allah for giving me the strength, knowledge, ability, and opportunity to undertake this study and complete it satisfactorily, as well for the experiences you placed in my path.

My gratitude to the Center for Research and Advanced Studies of the IPN and the Université de Lorraine, for allowing me to carry out my doctoral studies and opening the doors as my second home, sheltering my days of effort and dreams to overcome my academic studies.

To my family, Hossein, Teresa, and Amir for encouraging me to follow the path of discipline, for cultivating the seed of curiosity, for being my example of simplicity, humanity, and humbleness.

My deeply and special gratitude to my thesis directors and advisors, Dr. Arturo Vera Hernández, Dr. Didier Wolf, Dr. Lorenzo Leija Salas, Dr. Christian Daul, and Dr. Josefina Gutiérrez Martínez; whose help, mentoring and advice were necessary for the completion of this thesis and my doctoral and cultural formation.

To my brother Hamzeh and his wife Paola, for supporting me and sheltering me like a second family during my academic and personal formation.

I would also like to show my deep appreciation to Dr. Citlalli Trujillo, Dr. Wilfrido Gómez, and Dr. Benito Granados for all their support in academic mentoring, their fraternal support, and all the times they lent me her hand to expand my academic horizons.

My sincere gratitude to Dr. Álvaro and his wife Dr. Violeta for sheltering me like a second family during my residence in France. Without their help, my studies would not have had the same warmth and fraternity.

My special gratitude to my colleagues and friends Tấn Bình Phan, Sophie Tran, and Anthony Reinness for the lessons, warmth, and humanity that they always offered me during my internship.

Thanks to Hugo Zepeda Peralta and Rubén Pérez Valladares for their collaboration in this thesis through technical and scientific assistance. Also, for all their technical support and interest in my learning, for inspiring in me the serenity and patience least required in life.

Not last, my thanks to Alfonzo Toriz for accompanying me in the writing of this thesis and for sharing his knowledge with me, which I take with me as a great learning experience in life and an example of youth inspiration.

Thanks to the National Council of Science and Technology (CONACyT) for the support provided during my doctoral studies.

This thesis is dedicated to all those whose scientific efforts
slowly move the gears of progress.

- Rafael Bayareh Mancilla

Abstract

Medical infrared thermography is a quantitative method for identifying irregular temperatures for medical diagnosis. Because abnormal body temperature is a natural sign of illness, this modality's data can be used to detect disease or physiological abnormalities, such as diabetic foot which is the subject of this thesis According to the International Diabetes Federation, nearly half a million people were diagnosed with diabetes mellitus in 2019. Peripheral neuropathy may affect 40 % to 60 % of individuals because of diabetic foot issues. Amputation below the knee joint as a preventive operation is a common risk among these individuals, and it is estimated that one amputation occurs every 30 seconds around the world. Currently, MRI, radiography, and thermography, together with image processing techniques, are among the medical imaging modalities utilized to diagnose the diabetic foot early. Medical infrared thermography, on the other hand, is a non-contact, non-invasive, and non-ionizing passive approach. Infrared imaging of the diabetic foot is still mostly reliant on 2D images that only show a portion of the anatomy. In this scenario, a 3D thermal model would allow for better observation and inspection of the region of interest, which includes the plantar, lateral, and dorsal areas. The use of 3D modeling for the diagnosis of the diabetic foot has been documented in a few articles at the publication of this thesis.

The proposed method employs a series of merged infrared and visible spectrum images as data input for the 3D point cloud estimation and surface reconstruction, based on Structure from Motion and Multi-view Stereo methods. However, segmentation in thermal images is a task that remains manually performed since the detection of descriptive features is almost impossible in false-color images. Therefore, this thesis presents an automatic segmentation method based on the processing of radiometric information before generating a false-color image. Radiometric data processing is an alternative to digital image processing due to the feasibility to remove thermal interferences (e.g. lamp, thermal shadows, or even patient body parts) based on temperature threshold criteria, improving color contrast, and segmenting the region of interest, and combine onto visible spectrum images.

The fused multimodal images were used as input information for the estimation of the 3D surface of the foot. The obtained model was provided with a temperature scale related to the radiometric data obtained by each volunteer, as well as the possibility to rotate the model to observe each viewpoint. The findings show that the 3D multimodal model is feasible, allowing for better and faster visualization of temperature distribution during diabetic foot diagnosis. The contribution of this thesis concerns the acquisition of a 3D model with thermal information and automatic segmentation in thermal images for multimodal fusion. The perspective is the clinical validation to pilot test the assistance in the diagnosis of diabetic foot. However, from the experimental/theoretical perspective, it is contemplated to study the accuracy of image registration with the proposed method of automatic segmentation, and the thermal and spatial accuracy of the 3D models carried out with phantoms.

Keywords: diabetic foot; thermal 3D surface; IR radiometric processing; medical thermography.

Resumen

La termografía infrarroja médica es un método cuantitativo para identificar la temperatura irregular para el diagnóstico médico. Dado que la temperatura corporal anormal es un signo natural de enfermedad, los datos de esta modalidad pueden utilizarse para detectar enfermedades o anomalías fisiológicas, como el pie diabético que es el objeto de esta tesis Según la Federación Internacional de Diabetes, en 2019 se diagnosticó diabetes mellitus a casi medio millón de personas. La neuropatía periférica puede afectar a entre el 40 % y el 60 % de los individuos por problemas de pie diabético. La amputación por debajo de la articulación de la rodilla como operación preventiva es un riesgo común entre estos individuos, y se estima que se produce una amputación cada 30 segundos en todo el mundo. En la actualidad, la resonancia magnética, la radiografía y la termografía, junto con las técnicas de procesamiento de imágenes, son algunas de las modalidades de imagen médica que se utilizan para el diagnóstico precoz del pie diabético. La termografía médica por infrarrojos, en cambio, es un método pasivo sin contacto, no invasivo y no ionizante. Las imágenes infrarrojas del pie diabético siguen dependiendo en su mayoría de imágenes 2D que sólo muestran una parte de la anatomía. En este escenario, un modelo térmico en 3D permitiría una mejor observación e inspección de la región de interés, que incluye las zonas plantar, lateral y dorsal. El uso de la modelización 3D para el diagnóstico del pie diabético se ha documentado en algunos artículos en el momento de la publicación de esta tesis.

El método propuesto emplea una serie de imágenes fusionadas de espectro infrarrojo y visible como entrada de datos para la estimación de la nube de puntos 3D y la reconstrucción de la superficie, basándose en los métodos Structure from Motion y Multi-view Stereo. Sin embargo, la segmentación en imágenes térmicas es una tarea que sigue realizándose manualmente, ya que la detección de características descriptivas es casi imposible en imágenes de falso color. Por ello, esta tesis presenta un método de segmentación automática basado en el procesamiento de la información radiométrica antes de generar una imagen en falso color. El procesamiento de datos radiométricos es una alternativa al procesamiento de imágenes digitales debido a la posibilidad de eliminar interferencias térmicas (por ejemplo, lámparas, sombras térmicas o incluso partes del cuerpo del paciente) basándose en criterios de umbral de temperatura, mejorar el contraste de color, segmentar la región de interés y combinar en imágenes de espectro visible.

Las imágenes multimodales fusionadas se utilizaron como información de entrada para la estimación de la superficie 3D del pie. El modelo obtenido se dotó de una escala de temperatura relacionada con los datos radiométricos obtenidos por cada voluntario, así como de la posibilidad de rotar el modelo para observar cada punto de vista. Los resultados muestran que el modelo multimodal 3D es factible, permitiendo una mejor y más rápida visualización de la distribución de la temperatura durante el diagnóstico del pie diabético. La contribución de esta tesis se refiere a la adquisición de un modelo 3D con información térmica y la segmentación automática en imágenes térmicas para la fusión multimodal. La perspectiva es la validación clínica para probar la asistencia en el diagnóstico del pie diabético. Sin embargo, desde la perspectiva experimental/teórica, se contempla estudiar la precisión del registro de imágenes con el método propuesto de segmentación automática, y la precisión térmica y espacial de los modelos 3D realizados con fantomas.

Palabras clave: pie diabético; superficie térmica 3D; procesamiento radiométrico IR; termografía médica.

Résumé étendu

Mots-clés : pied diabétique ; surface thermique 3D ; traitement radiométrique IR.

La thermographie infrarouge médicale constitue une méthode quantitative d'identification des températures anormales pour le diagnostic médical. Une température corporelle anormale étant un signe naturel de maladie, les données de cette modalité peuvent être utilisées pour détecter des maladies ou des anomalies physiologiques, comme le pied diabétique qui est le sujet de cette thèse. Selon la Fédération internationale du diabète, près d'un demi-million de personnes ont été diagnostiquées avec un diabète sucré en 2019. La neuropathie périphérique peut toucher 40 à 60 % des sujets en raison de problèmes liés au pied diabétique. La visualisation infrarouge du pied diabétique repose encore principalement sur des images 2D qui ne montrent qu'une partie de l'anatomie. Dans ce scénario, un modèle thermique 3D permettrait une meilleure observation et inspection de la région d'intérêt, qui comprend les zones plantaire, latérale et dorsale. L'utilisation de la modélisation 3D pour le diagnostic du pied diabétique a été documentée dans quelques articles au moment de la publication de cette thèse.

Cette thèse propose donc d'obtenir des modèles thermiques 3D du pied, en utilisant une série d'images infrarouges et visibles fusionnées comme données d'entrée pour l'estimation du cloud de points 3D et la reconstruction de surface, basée sur les méthodes Structure from Motion et Multi-view Stereo. Pour réaliser la fusion d'images, il est nécessaire de segmenter les images thermiques. Cependant, cette tâche reste manuelle puisque la détection des caractéristiques descriptives est presque impossible dans les images en fausses couleurs. Par conséquent, une nouvelle méthode de segmentation automatique, basée sur le traitement des données radiométriques avant de générer une image en fausses couleurs, est présentée dans cette thèse.

La thermographie médicale offre des avantages significatifs dans la détection de plusieurs maladies par le biais des différences de température et de l'asymétrie thermique gauche-droite. La nature de l'imagerie 2D peut présenter un inconvénient en termes d'inspection du temps lorsqu'un scénario d'évaluation d'images multiples est présenté (analyse d'une succession d'images multiples et d'un nombre élevé d'images). De plus, l'examen d'images 2D avec un champ de vision limité (field of view - FOV) peut ne révéler qu'une partie de l'anatomie. Dans ce contexte, un modèle

thermique 3D pourrait être essentiel pour déterminer le pied comme une entité unique plutôt que par des vues partielles. La thermographie infrarouge a démontré son potentiel pour mesurer les différences de température de surface d'un patient sans contact. C'est une technique non invasive qui ne présente aucun risque pour le patient puisqu'elle mesure la température émise par le corps du patient au lieu de lui fournir de l'énergie (technique passive). Le fait que la thermographie ne puisse pas fournir d'imagerie sous-cutanée peut être limitatif puisque plusieurs auteurs ont proposé le concept de tomographie IRT, mais elle peut cependant aider à l'évaluation et au suivi des symptômes. De nombreuses disciplines médicales, ainsi que d'autres branches des sciences de la santé, ont publié des études établissant leur utilité dans l'évolution des altérations dues à une évolution pathologique. Le coût des équipements diminuant, ces études sont de plus en plus courantes. L'étude de la thermographie dans de multiples domaines de la médecine doit se poursuivre pour mieux comprendre ses applications cliniques potentielles et décider des troubles pour lesquels elle pourrait être utile. Des informations récentes suggèrent qu'elle gagne en popularité en tant que technologie non invasive et sans contre-indications, de plus en plus largement disponible.

Des facteurs externes peuvent affecter la mesure de la température de la surface de la peau, comme l'humidité relative, la température ambiante, les courants d'air et les interférences thermiques. Ces facteurs doivent être pris en compte dans la thermographie IR médicale. Cette section compare également plusieurs techniques actuelles de traitement d'image liées à la nouvelle proposition de thèse, qui est le traitement des données radiométriques IR. Ces données sont collectées sous forme de matrices et traitées comme un signal. Les informations du capteur peuvent être acquises uniquement sous forme d'informations numériques à partir de signaux électriques, ou elles peuvent être exprimées sous forme de température. Le principal avantage du traitement de ces informations par le traitement du signal avant le traitement de l'image numérique, est la segmentation et la correction des couleurs lorsque les données sont traitées préalablement comme un signal au lieu d'une image en fausses couleurs. Une région très contrastée de la zone d'intérêt sera recrééе à partir du traitement des données, avec un fond d'image homogène. Par-dessus cela, le Region of Interest (RoI) peut être récupéré sur un fond transparent. La segmentation est le résultat de cette étape, et elle fournit des données pertinentes pour la fusion multimodale du spectre visible et des images en fausses couleurs (c'est-à-dire les images thermiques).

La raison fondamentale de la segmentation du pied est d'éviter les interférences thermiques qui pourraient fausser les résultats et conduire à une mauvaise interprétation, même dans un environnement contrôlé. Comme nous l'avons démontré dans ce chapitre, les méthodes traditionnelles ne peuvent pas segmenter automatiquement le pied à partir d'une image dans le pire des cas : environnement non contrôlé, interférences thermiques, et gradient de température comme celui de la scène. En raison de ces limitations, la segmentation manuelle par un spécialiste est couramment demandée, ce qui constitue un inconvénient en termes de temps et d'effort lors de la manipulation d'une collection de plusieurs images. Par conséquent, il est proposé dans cette thèse de segmenter le RoI sur la base de l'information radiométrique (matrice de données de capteur ou matrice de température) afin que la scène puisse être homogénéisée, ce qui conduira également à améliorer la cartographie des couleurs uniquement dans le pied. Une autre raison majeure de segmenter le pied est de superposer l'image en fausses couleurs sur une scène à partir d'une image en lumière visible, afin de détecter plus de caractéristiques qui peuvent améliorer l'étape de reconstruction de la surface. La quantité de caractéristiques détectées dans les images en fausses couleurs est généralement limitée, ce qui conduit à une mauvaise correspondance des valeurs aberrantes et, dans le meilleur des cas, à une surface de mauvaise qualité. Les algorithmes traditionnels de traitement d'images pour la segmentation d'images thermiques en vue d'une fusion multimodale ont, d'autre part, des limites. Bien qu'il soit désormais possible de segmenter manuellement, les propriétés thermiques des informations recueillies sont statiques, ce qui impose des restrictions. Lorsque l'on travaille avec une grande collection d'images, la segmentation selon le critère de seuil d'une température spécifique présente plusieurs avantages, notamment la possibilité d'améliorer le contraste du RoI et d'automatiser la procédure. Les images superposées sont essentielles comme entrée pour l'étape SfM.

The fused multimodal images were used as input information for the estimation of the 3D surface of the foot. A collection of merged multimodal images is necessary for ensuring an accurate surface reconstruction. The required multimodal image is a false-color RoI superimposed into a visible light scene. This multimodal registration task is difficult, especially when there are interferences attributable to acquisition protocol mistakes (e.g. objects with heat sources or the personnel themselves).

Le modèle 3D obtenu était doté d'une échelle de température liée aux données radiométriques obtenues par chaque volontaire, ainsi que de la possibilité de faire pivoter le modèle pour observer chaque point de vue. La contribution de cette thèse concerne l'acquisition d'un modèle 3D avec des informations thermiques et la segmentation automatique dans les images thermiques pour la fusion multimodale. Il est important de souligner qu'à ce stade, les données d'entrée seront les images multimodales superposées (images thermiques et du spectre visible). Ces images seront traitées par la détection de caractéristiques descriptives (i.e. SIFT), la mise en correspondance de points clés, la génération d'un cloud de points 3D, la génération d'un cloud de points dense, et finalement la reconstruction d'une surface et d'une texture 3D. Les différentes étapes d'un pipeline comprenant une méthode SfM incrémentale, l'étape MVS, le maillage de la surface et la texturation de l'objet ont été présentées aussi. La construction itérative de clouds de points à l'aide de techniques SfM incrémentielles produit des clouds de points épars sur une surface étendue. Ces clouds de points épars peuvent être densifiés dans l'étape MVS, qui est une méthode fiable et précise pour une variété d'applications, y compris celles relatives à la reconstruction d'images multimodales.La méthode proposée dans cette thèse, ce n'est pas la meilleure solution pour déterminer la température par région. Cette façon de procéder rend le résultat dépendant de l'interprétation par l'utilisateur de la coloration d'une zone spécifique. Cependant, même dans l'IRT 2D, où les images sont affichées à côté d'une barre latérale de température, cette technique est fréquemment utilisée. Cette approche a également été utilisée dans cette thèse car l'IRT est une mesure relative et indirecte qui dépend de la prédiction de la température concernant la quantité d'énergie IR enregistrée. De plus, comme les éléments de la matrice de température du RoI sont de tailles différentes, la normalisation de la température concernant les minima et maxima détectés dans chaque image fournit une approximation adéquate pour afficher les informations thermiques à côté du modèle.

Les résultats démontrent la faisabilité et l'utilité de l'extraction et du traitement des données radiométriques pour récupérer une image IR segmentée combinée dans une scène texturée en lumière visible. Avant d'interpréter les cartes thermiques comme des images, une approche de traitement radiométrique IR peut éliminer les interférences thermiques de fond en utilisant des seuils comme critères de segmentation. Dans des conditions, telles qu'un environnement contrôlé et l'élimination des sources de chaleur dans lesquelles le $\Delta T < 2,6$ % par rapport au RoI, cette stratégie conduit à l'automatisation du processus quel que soit le RoI visé. La segmentation du réseau thermique serait inadéquate dans d'autres circonstances. D'autre part, les protocoles de thermographie médicale recommandent un échantillonnage dans un environnement contrôlé pour éviter les facteurs d'interférence. Nos recherches montrent que la méthode proposée est précise lorsque ces directives sont respectées. Seul un étalonnage thermique par rapport à un thermomètre de référence sur un corps dont la distribution thermique est connue a été effectué, avec une correction de $\Delta T = 0{,}4°C$. En outre, l'imprécision de ΔT due au facteur d'émissivité angulaire a été ajustée (erreur ≈ 10 % près de 90°), ce qui est une difficulté courante dans la recherche sur la thermographie 3D. Sans ajustement angulaire, les deux ensembles présentaient une erreur de distribution de 4,74°C en moyenne.

Le procédé COLMAP nécessite une étape précise de reconnaissance et de mise en correspondance des caractéristiques pour la reconstruction des surfaces, ce qui ne peut être garanti lorsque seules des images IR avec peu de textures sont utilisées. Par conséquent, les images en lumière visible ont été requises comme données supplémentaires pour l'approche SfM afin de générer des surfaces de manière fiable et précise. Comme l'a démontré le modèle 3D de l'ensemble S2 (volontaire 2), la précision qualitative d'une surface 3D est déterminée par la qualité des images plutôt que par le nombre de points clés. Bien que S1 (volontaire 1) présentait 42 % de caractéristiques significatives en moins que S2 (volontaire 2), la reconstruction était visuellement adéquate. L'amélioration du capteur de lumière visible par l'utilisation de caméras plus récentes, avec une résolution plus élevée et des pixels plus petits, pourrait être une solution. Cependant, comme ils ne couvrent que la surface du modèle où la distribution des couleurs est directement proportionnelle à l'intensité de la température, les réseaux radiométriques IR étaient essentiels pour déterminer les images IR qui ont été utilisées comme méthode de "texture d'enveloppement". Comme le modèle est affiché avec une échelle de température, il est important d'attribuer la distribution des couleurs de manière appropriée à l'intensité de la température du RoI. L'émissivité angulaire étant un problème en thermographie, la température a été corrigée pour l'angle de capture. Le ΔT selon la référence de l'échantillon a été suggéré comme étant un problème linéaire, donc la précision de la matrice de température a été corrigée. L'ajustement de l'erreur n'a pas influencé la distribution des couleurs dans le RoI mais a influencé l'échelle avec le modèle 3D.

La perspective de cette méthode est qu'elle peut être appliquée à une segmentation supplémentaire du RoI à l'aide d'applications de données radiométriques, telles que des appareils de thermographie IR portables et des prototypes basés sur des systèmes embarqués. Par exemple, cette étude a été menée à l'aide d'un équipement thermographique construit pour un usage général/industriel, avec des dimensions et une manipulation qui pourraient permettre de mener de futures investigations dans des laboratoires de recherche ou des établissements de santé.

Table of Contents

Chapter 1

Medical Context and Scientific Objectives

Contents

1.1 Medical Context

This chapter covers the basics of diabetes, the complications it might entail, and the advantages of implementing 3D thermal modeling for possible early detection via foot surface temperature distribution assessment. Although medical thermography provides significant advantages in the detection of several illnesses through temperature differences and left-right thermal asymmetry, the nature of 2D imaging may present a disadvantage in terms of timing inspection when a multiple picture assessment scenario is presented (analysis of a succession of multiple and a high number of images). Furthermore, the examination of 2D images with a limited field of view (FOV) may reveal only a portion of the anatomy. In this context, a 3D thermal model could be essential for determining the foot as a single entity rather than by partial views. This section presents a review of medical advances in the detection of diabetic foot based on medical imaging techniques. The medical context section highlights the difficulties in diagnosing the complication.

1.1.1 Diabetes Mellitus and Diabetic Foot

According to the International Diabetes Federation (IDF), 463 million people were diagnosed with diabetes mellitus (DM) in 2019, and the cases are expected to reach 578 million by 2030, and 700 million by 2045. DM is a chronic illness whose origin relates to raised levels of glucose in the blood which cannot metabolize insulin, nor produce enough insulin. The absence of insulin, or the failure of cells to respond to it, leads to high levels of blood glucose (hyperglycemia), which is the clinical indicator of diabetes [1]. The diagnosis criteria limits have changed over the years. The last update was published in 2016 by the World Health Organization (WHO) [2], resumed in Table 1.

Table 1: WHO diagnosis criteria according to glucose concentrations. Diabetes is diagnosed if one or more of the parameters are higher than the limit given in each column [2].

	Fasting plasma glucose	Two-hour plasma glucose	HbA1c	Random plasma glucose
Diabetes mellitus	7.0 mmol/L	11.1 mmol/L	48 mmol/mol	11.1 mmol/mol
Impaired glucose tolerance	7.0 mmol/L	11.1 mmol/L	-	-
Impaired fasting glucose	6.1-6.9 mmol/L	7.8 mmol/L	-	-

The IDF defined 3 types of diabetes [2]: Type I Diabetes, Type II Diabetes and Gestational Diabetes. However, there are other less common types of diabetes such as monogenic diabetes, which is a consequence of genetic mutation. It usually appears in young maturity and the neonatal stage. From 4% to 13% of diabetes in children is due to monogenic diabetes. Secondary diabetes arises as a complication of other diseases, such as hormonal disorders or diseases of the pancreas [3]. Although the etiology of type I and II diabetes (the most common) are well established, some factors trigger this disease. These factors are ethnicity, family history of diabetes, history of gestational diabetes, and advanced age. The increase in the population with type 2 diabetes is related to aging, economic development, increased urbanization, unhealthy diets, and decreased physical activity. In contrast to people with type 1 diabetes, many people with type 2 diabetes do not require daily insulin treatment to survive. The treatment for type 2 diabetes is the adoption of a healthy diet, increasing physical activity, and maintaining a normal body weight [1].

People with DM have an increased risk of developing life-threatening problems. High blood glucose levels can trigger heart diseases involving consequences on blood vessels, eyes, kidneys, and nervous system. Complications of DM can be prevented or controlled by maintaining blood sugar, blood pressure, and cholesterol levels as close to normal as possible [4]. Several complications can be detected early with diagnosis programs that allow for treatments to prevent diabetes progression.

A common complication is poor circulation in the feet because of damage to the blood vessels. These problems increase the risk of ulceration and infection, requesting an amputation in the worst case. Frequently, diabetic foot carries a risk for DM patients since it could lead to amputation below the knee joint as a preventive procedure. Furthermore, DM is responsible for a lower limb amputation every 30 seconds. However, with monitoring and health control, amputation can be prevented. Even when a patient suffers an amputation, the remaining leg (or even the patient's life) can be saved. Because of these risks, people with diabetes must have their feet examined regularly [5]. A secondary problem is the appearance of foot ulcers as a consequence of two chronic diseases: peripheral neuropathy and vascular insufficiency. The DF etiology is defined by the following factors [4,6]:

- Diabetic neuropathy is defined as the presence of symptoms of peripheral nervous system dysfunction. This is one of the most frequent microvascular complications in the DM population, which prevalence increases as the time evolution of diabetes, age, hyperglycemia, and its duration increase. It is the most important risk factor associated with the presence of foot ulcers.
- Peripheral vascular disease (PVD), is associated with the presence of neuropathy. PVD is a determining risk factor in the evolution of foot lesions toward amputation.
- Biomechanical alterations are characterized by changes in the points of support during walking or in a static position, which induces the appearance of calluses and/or pressure ulcers.
- Various factors: Time (elders than 40 years), Evolution (10 years with DM), smoking, low socioeconomic status (diet), and living alone (stress).

Among the patients diagnosed with one or more elevated glucose factors, about 40% to 60% will suffer from peripheral neuropathy, as a result of DF complications [7]. Usually, DF carries a risk for DM patients leading to non-traumatic Lower Extremity Amputation (LEA) below the knee joint as a preventive procedure [8,9]. Furthermore, the annual prevalence of DF is nearly 2% and is responsible for an LEA every 30 seconds [5,10]. DF complications can be affected by sociocultural factors such as socioeconomic status, lack of or inadequate footwear, and ignorance of DM treatments and care [11]. Several factors are involved in general the presence of peripheral vascular disease, neuropathy, and ulcers on the lower limb and foot [12].

Diabetic complications such as infection, ulcers, or gangrene are the prominent signs of diabetes late diagnosis and hospitalization. Often, foot ulcers precede lower-limb amputation, being the most common etiology of peripheral arterial disease (PAD), neuropathy, excessive foot-ware pressures, deformity, and trauma [13]. A classification of ulcers can assist in preventive treatment and approach. The classification is based on wound category centered on parameters such as ischemia, neuropathy, infection, location, and tissue loss [14]. The most accepted system classification for diabetic foot based on ulcer presence is the Wagner classification, which considers the existence of gangrene, necrosis, or osteomyelitis. This classification is presented in Table 2 [15]. Figure 1 depicts the progression of the diabetic foot according to Wager's classification.

Table 2: Wagner Ulcer Classification System.

Grade	Lesion
0	No open lesions; may have deformity or cellulitis
1	Superficial diabetic ulcer (partial or full thickness)
2	Ulcer extension to ligament, tendon, joint capsule, or deep fascia without abscess or osteomyelitis
3	Deep ulcer with abscess, osteomyelitis, or joint sepsis
4	Gangrene localized to a portion of the forefoot or heel
5	Extensive gangrenous involvement of the entire foot

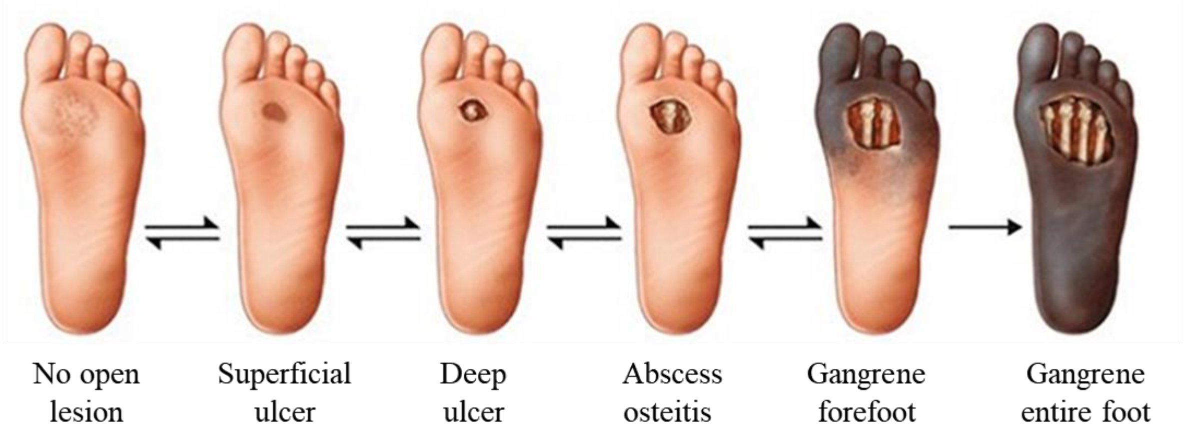

Figure 1: Dysvascular foot breakdown according to the Wagner ulcer classification, the illustrations were taken from [16].

1.1.2 Early Diagnosis of the Diabetic Foot

Diabetic ulcers are the most prevalent foot lesions that result in amputation of the lower limbs. Physicians play a critical role in the prevention or early detection of diabetic foot complications. Diabetic foot typically requires a full understanding of the amputation risk factors, routine evaluation, and diligent regular inspection. Early or quick treatment of ulcers can often prevent complications of DF and even reduce or eliminate the possibility of amputation. The objective of early diagnosis is to aid in the quick healing of the lesion and to prevent recurrence once the lesion has healed. Multidisciplinary management protocols that focus on prevention, education, periodic examinations, and therapeutic footwear have proved to a significant reduction in the incidence of lower extremity amputations [17]. Diabetic neuropathy, structural foot deformity, and peripheral artery occlusive disease are the most prominent risk factors for ulcer formation. A thorough physical examination, supplemented with monofilament neuropathy testing and noninvasive testing for vascular insufficiency, can identify people at risk for foot ulcers and detect those who already have ulcers or other diabetic foot problems [18].

Exhaustive and systematic evaluation and categorization of foot ulcers help to establish appropriate treatment. Some quick ways of diagnosis and clinical evolution are [18,19]:

- Monofilament testing is a low-cost, simple-to-use, and portable test for detecting the loss of protective sensibility in healthy feet, as suggested by practice standards. The nylon monofilament test formally called the Semmes-Weinstein monofilament (SWM) test, verifies for damages to the nervous system. This test intends to detect a lack of sensibility on the sole. The examination is performed at specific points on the sole. If there is a risk of injury, the patient will be unable to feel the filament in the specific region when the object is pressed against the foot [20]. Figure 2 shows side by side, the most common areas in which the filament is used, and a thermal image is often used for the study of DF [21].

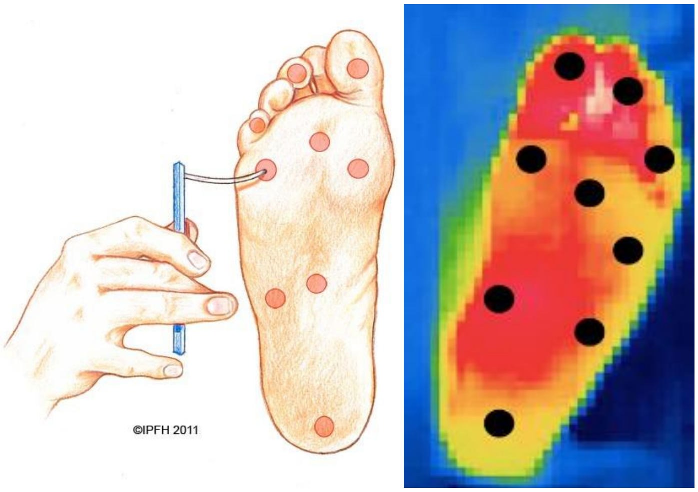

Figure 2: common areas for the development of ulcers [21].

Visual observation of anatomical deformations and presence of limited movement in areas of high pressure. A foot ulcer can develop itself when abnormal pressure is associated with a lack of sensation. Most DF ulcers are prone over areas of bony prominences, commonly when a hammer toe, calluses, or bunions lead to abnormally prominent points. Ulceration usually occurs over the dorsal region, metatarsal heads, and the heel.

- A DM patient with a background of previous ulceration or amputation can increase the sore risk for further ulcers and articulations deformity. In such complications, they may cause the abnormal distribution of plantar pressures and result in the formation of new ulcers which is preferred to perform an amputee. It is recommended to examine a diabetic patient with a very low risk of foot ulceration once a year for signs or symptoms of loss of protective feeling and peripheral artery disease and assess if they are at an elevated risk of foot ulceration. A history of foot ulceration or lower-extremity amputation; diagnosis of end-stage renal disease; presence or progression of foot deformity; limited joint mobility; abundant callus; and any pre-ulcerative sign on the foot are all factors to consider in a person with diabetes who is at risk of foot ulceration. For those categorized as grade risk 1, repeat the screening every 6-12 months, every 3-6 months for grade risk 2, and every 1-3 months for grade risk 3. A patient who is at risk of developing a foot ulcer will be instructed to safeguard their feet by not continuing to use inappropriate barefoot, walking only with socks without shoes, or in thin-soled slippers, whether indoors or outdoors. Finally, to assist prevent a foot ulcer in a diabetic who is at risk of foot ulceration, provide appropriate treatment for any pre-ulcerative symptom or extensive callus on the foot, ingrown toenails, and mycological infections on the foot [22].

Home foot temperature monitoring, pressure-relieving therapeutic footwear, and specific surgical procedures have all been shown to be useful in preventing recurrent foot ulcers. One of the most significant types of research in recent decades has been the acceptance of the importance of a multidisciplinary approach to this complex problem, which has resulted in the establishment of dedicated diabetic foot institutes. The timely examination and identification of wounds, as well as proper techniques of prevention and treatment with internal and exterior surgery, are critical to clinical management for this pathology in multidisciplinary models developed around the diabetic foot. Various foot ulcer prevention strategies are either employed in clinical practice or have been researched in [17,23–25]. Table 3 summarize studies from the past 10 years, highlighting advances in the understanding of diagnosis and treatment of DF.

Table 3: Overview of the key findings in diabetic foot ulcer knowledge and care over the past years.

Field	Since 2012	Last 3 years
Surgical approach	Inpatient treatment with aggressive ablative therapeutic surgery [26].	Corrective surgery; typically, in outpatient clinics and specialized diabetic foot centers; more conservative tissue sparing therapeutic (even for osteomyelitis) and preventative surgery [27].
Skin impedance	Artifacts where the patient is moving or physically active during the recordings than for controlled setups in the laboratory [28].	Development and equipment for body physiological parameters for remote and wireless monitoring [29].
Thermometry	Patient preparation, imaging hardware, image capture, and analysis should all be standardized [30].	Wearable thermometers are detachable components that may be worn by a user during daily activities (e.g., watch, earphone, eyeglass, and helmet). Invisible thermometers are implanted in living items to measure temperature (e.g. beds, chairs, dressing mirrors, and ceiling lamps) [31].
Medical Imaging	Each of the three modalities (PET, CTI, and MRI) does not provide enough information on its own, hence a multimodal approach should be used to provide an appropriate diagnosis [32].	Multimodal imaging and 3D modeling [33,34].

Temperature is one of the factors that stands out in the diagnosis and treatment of the diabetic foot. Body temperature is used as a key indicator and vital parameter to distinguish healthy tissues from potential lesions [35]. Researchers suggested that vascular disorders, endocrinological disorders (particularly diabetes mellitus), regenerative medicine, musculoskeletal disorders, neurological disorders, cancer, and surgery all have potential applications in Infrared Thermography (IRT). A review of IR medical thermography is discussed in the next section.

1.2 IR Medical Thermography

A rise in body temperature is a common symptom of illness. In terms of body temperature monitoring, IRT allows for a quick, passive, non-contact, and non-invasive alternative to standard clinical monitors. Also, IRT is a technique that allows measuring body surface temperatures from a chosen distance. The advantage of infrared cameras to obtain correlations between thermal physiology and skin temperature has steadily increased during the last few decades. Breast cancer, diabetic neuropathy, and peripheral vascular diseases have all been successfully diagnosed with

IRT. This technique has been employed in gynecology, kidney transplantation, dermatology, cardiology, neonatal physiology, fever screening, and brain imaging [36]. Real-time high-resolution thermographic images are now achievable using modern IR cameras, data collecting, and processing techniques, which is critical to supporting more research in this field.

1.2.1 Background and History

In the past, the temperature has been proved to be an excellent predictor of health. The temperature has been exploited for clinical diagnosis since 400 BC. The human body can maintain a steady temperature that is distinct from the ambient temperature. However, the physiological process of thermoregulation regulates the body's temperature. A fluctuation of a few degrees of the core body temperature (33°C - 42°C) is considered a strong indicator of probable disease [37]. Perspiration and vasodilation decrease core body temperature, allowing heat to be transferred through conduction, convection, radiation, or evaporation. The circulation transports the heat created in the body core to the periphery (skin), where it is dissipated by sweating and evaporation. As a result, surface temperatures are a mirror of the body's internal functioning. This approach to body temperature in the context of health led to the development of clinical thermometers and, ultimately, IR imaging tools [38].

Thermometers were invented in the 17th century. Carl Wunderlich was the first to methodically study the temperature of fever-stricken people and compare it to that of healthy subjects in 1868, establishing temperature as a scientific predictor of illness. He determined that a temperature range of 36.3 to 37.5 °C may be considered normal (normothermic) and that a temperature above this range should be considered a sign of disease [39].

Sir William Herschel's discovery of infrared radiation in 1800 was immediately followed by the research of his son, John Herschel: the recording of the first thermal image, which opened up new dimensions in the realm of temperature measurement (Figure 3, was taken from [40]). James D. Hardy claimed that human skin can be considered a blackbody radiator when he detailed the physiological role of infrared emission from the human body in 1934. He discovered the diagnostic value of infrared temperature measurement, paving the path for the use of IRT in medical sciences.

However, owing to a lack of quality equipment and technological know-how, the first application was only documented in 1960 [41].

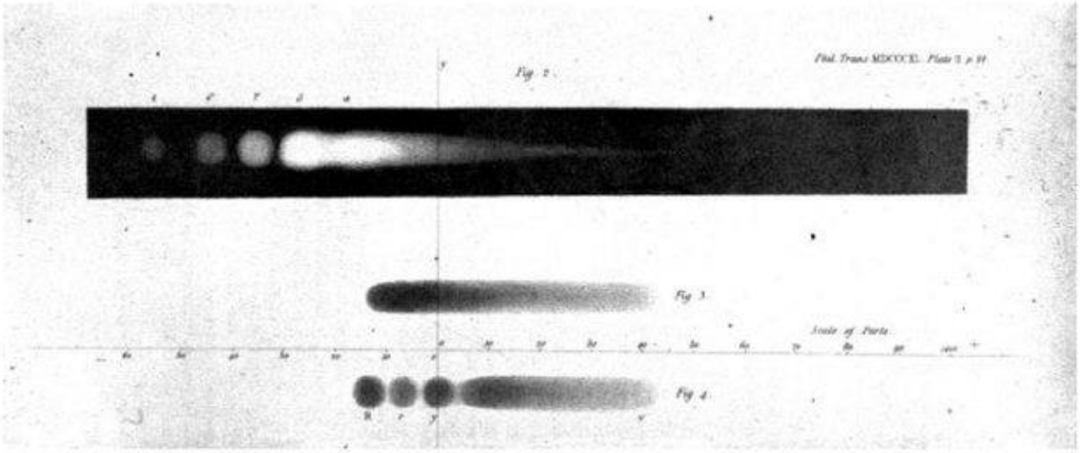

Figure 3: John Herschel used the evaporography process to create a thermogram. The image was taken from [41].

IRT is a highly sensitive, dynamic, non-contact, and non-invasive imaging technology. It is based on the principle that all objects with a temperature greater than absolute zero generate electromagnetic radiation, often known as IR or thermal radiation. This technology is based on optoelectronic devices to study and measure surface IR radiation and convert it into temperature. The wavelength of this radiation is between 0.75 and 1000 µm. However, the wavelength range of near IR (20 µm) is technically relevant for measuring temperatures [42].

The IR spectrum as a form of heat radiation, discovered by Herschel in the19th century, was called the “thermal spectrum”. The latter was discovered during a study of the new optical material by testing samples of crystals and colors that provided similar reductions in brightness. Several samples passed heat that could cause eye damage after only a few seconds of observation [43]. Currently, thermographic equipment uses an array of sensors known as bolometers, invented by Samuel Langley in 1880. The sensor consisted of a thin darkened plastic ribbon connected to a Wheatstone bridge on which infrared radiation was focused and to which a sensitive galvanometer responded. An array of bolometers generates an array of radiometric data, which is represented as a false-color image equivalent to the intensity of IR energy detected within the capture region.

The first modern technique which associates infrared technology with image processing for medical applications was introduced in 1994. A coordinated effort was launched under the Department of Defense of the USE funding jointly financed by the Office of the Secretary of

Defense Science and Technology, the Defense Advanced Research Projects Agency, and the Army Research Office. The primary obstacles to the medical community's acceptance of this method were addressed [45]. The following issues were discovered to be of prime concern:

- Medical information standardization and validation.
- A better understanding of how thermal signatures affect the body's pathophysiology.
- Increased publication and exposure of medical infrared imaging in top publications and conferences.
- The use of an interactive web-based database to characterize thermal signatures.
- Image capture and interpretation training.

Early infrared cameras consisted of a moderate amount of detector elements (1 to 180), which required cryogenic cooling to operate efficiently without noise. The image was generated via a scanning mechanism with mirrors in the camera system. Electrical contact was formed with each detector, which was a time-consuming and laborious task. This camera was large, consumed a lot of power, and was quite expensive to produce. As a result, manufacturers concentrated on the development of a more efficient, lower-cost system, which eventually led to uncooled Focal Plane Array (FPA) type cameras, such as the device used for this project (Fluke Ti32). The detectors of the FPA camera form vast arrays, eliminating the requirement for scanning. Electrical contacts are formed to the detector array at the same time, reducing greatly the number of vacuum leads. IR imaging has been used in a variety of medical applications. Oncology (breast, skin (e.g. diabetic foot), etc.), vascular illnesses (diabetes, Deep Venous Thrombosis), pain, surgery, tissue viability, drug and therapy monitoring, and respiratory disorders are the most common [46]. Figure 4 presents the superficial temperature measured on the sole of a DF patient, in which the temperature was predicted by a mathematical model [47].

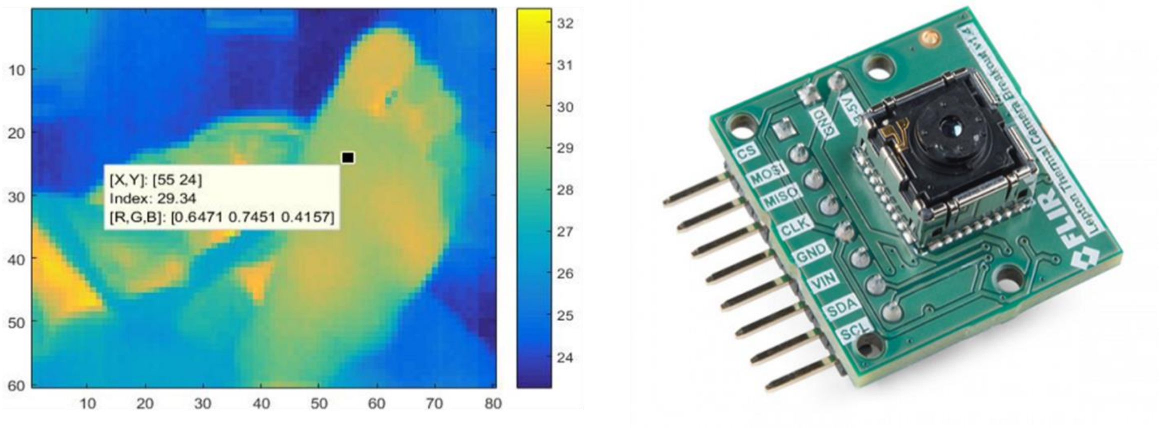

a) b)

Figure 4: a) Thermal image of a DM patient taken with Lepton 2.5. The black dot on the image points to a punctual temperature (29.34°C in this example) predicted by a characteristic equation, b) Lepton 2.5 Long wave IR (LWIR) sensor based on microbolometers array [48].

The first approach for the study of thermal assessment was reported in 1980: It was established in [35,49] that abrupt fluctuations in human skin temperatures reveal crucial physiological and pathological information that cannot be obtained from static temperature mapping (i.e., measurement of temperature distribution over areas of skin). Since the temperature of the skin is dependent on blood flow into cutaneous and subcutaneous tissues under physiological conditions, and blood is the heat exchange fluid, skin temperature shows a variety of hemodynamic processes. Pulsatile cardiogenic variations in blood flow, as well as neural control of blood flow in the vasculature and microvasculature, influence these processes. Since blood perfusion influences skin temperature variably depending on the underlying vascular anatomy, assessing these processes necessitates repeated temperature imaging of the region of interest (RoI) at frequencies greater than the highest frequency of observable blood supply modulation [50]. The structure of the vasculature, as well as systemic variations in blood flow due to both heart function and neuronal systemic and local control of vascular blood flow and perfusion of the capillary bed, may all be learned via dynamic thermal imaging of RoI.

Occlusions (including peripheral vascular occlusive diseases) and aneurysms, as well as the vascular complications of diabetes, are examples of vascular illnesses. A thermography study could assist in the diagnosis of diabetic neuropathies from diabetic vascular occlusive disease, allowing for better diabetes therapy. In addition, this technique may help to early detect inflammatory lesions such as rheumatoid arthritis, local infections, and ulcers [51]. IR thermography can be considered as a technique that could be exploited for the objective of finding temperature changes that induce the physiological disorders that are caused in the diabetic foot due to the physiological effects, outlined in the next section.

1.2.2 Medical Applications

Thermography is a technique that accurately measures the body temperature and that visualizes this information without requiring physical contact. It allows medical professionals to record the cold and hot areas of a patient's body using the energy radiated by their skin, with a precision of up to one-hundredth of a degree centigrade [52]. Table 4 presents an overview of a few medical studies involving medical IRT recently published.

Table 4: State-of-the-art of medical IRT studies.

Author	Year	Study
Farooq et al [53]	2020	Breast tumor classification
Mota-Rojas et al [54]	2021	Mechanisms of Thermoregulation in Mammals
Dang et al [55]	2021	Assessment of Burn Depth and Healing Potential
Mažeika et al [56]	2021	Hidradenitis suppurativa diagnostic in skin
Bayareh Mancilla et al. [57]	2021	Early diabetic foot diagnosis and treatment

Thermography has been used to study the physiological reactions to exercise, emotions, environmental temperatures, pathologies, and other factors. An evaluation of IRT as a research tool in physiology and medicine revealed that this technique allows overcoming the limitations of traditional thermal studies with contact measuring methods [58]. The dynamics of local sweating and profuse sweating from sweat glands due to metabolic changes were found to be closely related to external heat in a thermoregulation study, with the increase and decrease in the standard deviation of temperature being typical of prolonged physical load (and subsequent relaxation) and external whole-body heating, respectively [58]. Figure 5 depicts the effects of temperature on thermoregulation as well as the image created from the observed temperature intensity; the illustration was taken from [52].

Figure 5: Assessment of the effect of thermoregulation with IRT. Paraffin cream was applied on the right hand to enhance the thermal effect, in which the hand should perform temperature regulation that may be observed with a thermal camera [52].

Thermography has also been utilized to detect blood flow changes in muscles implicated in emotional responses. Vasodilation causes hyperemia (an excess of blood in the arteries supplying an organ or other area of the body), which is a symptom of a variety of illnesses. It raises the temperature of the vessels, often at a superficial level and because of a direct or reflex impact. Because it is a simple technology for measuring the superficial temperature in the human body, IRT is currently being employed as a tool for the diagnosis of disorders with trophic symptomatology of thermal origin [59]. Heart rate, body temperature, blood pressure, and breathing rate are four vital signs that are commonly evaluated in clinical settings as markers for evaluating fundamental body functionality and efficiency. The human body is homeothermic since it maintains a constant temperature to coordinate metabolic activity through its established thermoregulatory mechanisms. The average thermal energy created by metabolism within the human body is measured by body temperature [31].

To maintain physiological homeostasis, thermoregulatory processes are crucial. When external and internal conditions vary, a thermoregulatory center in the hypothalamus is responsible for regulating heat gain and loss to maintain body temperature at a reference set point within a certain range for a body to operate properly. The endocrine system begins to enhance or reduce energy production or dissipation when its temperature deviates from the default set point due to various stimulants, and thermoreceptors transduce these inputs into brain impulses, causing the temperature to return to the set point [31]. The core body temperature is maintained at the rational physiological set point of 37.0 °C by thermoregulatory processes, even though surface body temperature can be tolerated over a wide range and even temperatures close to 0 °C, in extreme conditions. Vasodilation increases the blood flow of arterioles through the arteries and redirects blood into the superficial capillaries beneath the skin in a hot environment to speed up heat loss through convection and conduction. Sweating is a quick way to decrease the heat by draining water from beneath the skin surface through eccrine sweat glands [60]. The study of thermoregulation has a wide range of applications, which are currently being supported by the availability of effective technologies such as IRT. Understanding the effects of changes on behavior and productivity; analyzing the effects of exercise on animals participating in sporting activities; identifying the microvascular changes that occur in response to fear, pleasure, pain, and other situations that cause stress in animals; and examining thermoregulating behaviors are just a few examples of these areas.

The early identification of breast cancer is another field that has seen a significant increase and relevance. IRT is used to analyze pathologies associated with breast cancer, such as mastitis, as a complementary non-invasive imaging tool. When tumor abnormalities are discovered, it is no longer used as an initial evaluation approach, but it is still a useful tool for regulating the evolution of other conditions with thermal superficial changes [61]. Mammography is the most frequent diagnostic method for detecting breast cancer. Despite its diagnostic utility, it has significant limitations, including the potential for rupturing the encapsulated tumor, radiation exposure, and low sensitivity in young and dense breasts. In comparison to mammography, IRT is a non-contact procedure that does not expose patients to radiation or cause mutations. In addition, there is no age-related variation in sensitivity. IRT detects functional vascular and metabolic abnormalities in tissues before they become morphologically apparent [61]. It has a high sensitivity of 93.6 % and a 91.2 % negative predictive value [62].

The prognosis and aggressiveness of the tumor appear to be linked to thermovascular activity. The temperature rises locally due to the increased vascularity and metabolic rate of cancer cells. When images are acquired following a cold stress test, a breast region will manifest hot patches (as the vasculature of the cancer cells lack a muscular layer rendering them resistant to vasoconstriction) [63]. Inside the cancerous tissues, there is also a constant state of inflammatory alterations and nitric oxide production, resulting in persistent vasodilation. Abnormal patterns in thermal imaging are the strongest predictors of breast cancer development. Figure 6 depicts the combined vascular patterning and temperatures across the two breasts (taken from [61]). Low specificity, reliance on the research knowledge for interpretations, and non-coverage under healthcare handling have all been major obstacles to the routine clinical use of IRT [30,53,63,64].

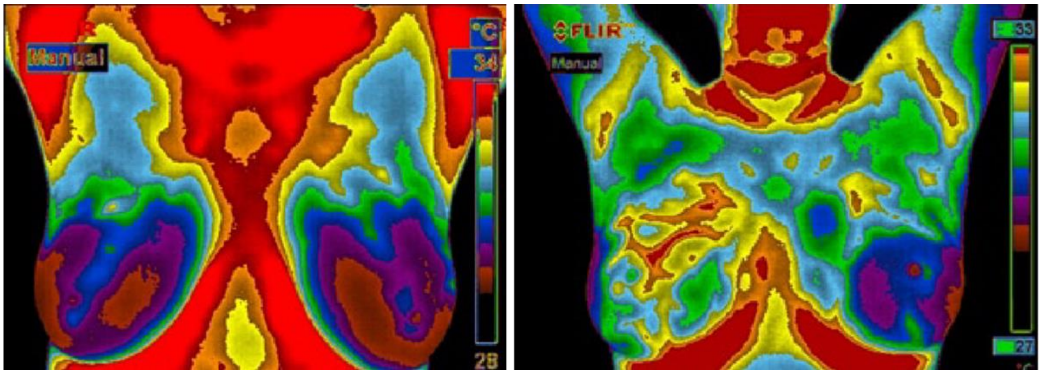

a) b)

Figure 6: Vascular patterning and temperatures across the two breasts images, a) normal nonvascular pattern, b) severely abnormal temperature distribution [61].

The thermography in diabetes and the early diagnosis of diabetic foot are the subjects of the IRT investigation detailed in this thesis. Thermal spot thermometers were employed in the first study on foot skin temperature as a self-assessment tool. However, it is likely that a hotspot not occurring at the preset locations would be missed using a common thermometer, and the method lacks usability because physicians or users would register temperature changes on a punctual spot [65]. Therefore, IRT imaging was exploited in future studies due to the capability of capturing full plantar and feet regions, and also this approach is contactless and has the potential to improve usability [66]. Thermal differences can also be calculated using a computer or a dedicated application. Because the original IR cameras were too expensive, these projects have not yet resulted in in-home monitoring systems. Costs have dropped considerably as a result of the commercialization of low-cost smartphone-based IR cameras, and studies for home use are now feasible [67].

The study of liquid crystal films (LFC) is a method based on temperature differences that allow for quick acquisition of the 2D temperature distribution on body surfaces. This technique provides a temperature distribution over an image, which contains a spatial and temperature resolution. At the moment of this technique, the color pattern was not available until the adoption of computer image processing techniques, in such a way that the displayed image of the LCF allowed only a visual temperature analysis through a comparison to a reference chromatic palette with a resolution of 1°C [68]. Temperature distributions are estimated with relatively weak precision due to the chromatic range with an interval of roughly 5°C. Nevertheless, because of their nature, they can only be used in a laboratory or *in vitro* tissues that can be cleaved by a film [69]. In this sense, thermography may be better for other approaches to diagnosing diabetic foot since it is a noninvasive technology that analyzes infrared emissions and allows visualization of the temperature patterns displaying a false-color image representative of the temperature intensity. Also, thermographic devices can be operated in various scenarios, such as medical applications [70]. Figure 7 depicts two thermal images for the comparison of feet without DM background (on the right) and a foot of a patient with possible DF (on the left); the images were taken from [21].

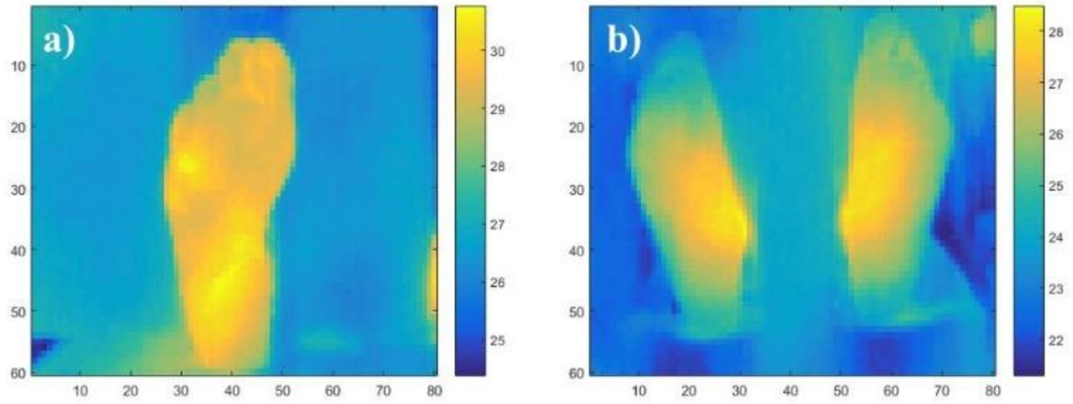

a) b)

Figure 7: a) Thermogram of a person with possible DF, b) thermogram of a person without DM background [21].

Incorrect diagnosis is associated with poor prediction of DM, particularly amputation, in patients with DF ulcers. Outcome prediction in patients with ulcers could be useful for clinicians in optimizing and individualizing treatment strategies. A temperature difference greater than 2.2ºC could be used to predict an ulcer when comparing the same region in booth feet ($\Delta T \geq 2.2$°C) [71]. The ΔT between two feet can be 4.8 times its value a week before the formation of an ulcer. Therefore, early detection through temperature differences, associated with neuropathy and vascular disease, may assist in early DF detection [72]. There are several reasons explaining why thermographic images can be difficult to interpret. Even in non-diabetic subjects, there is a lack of information about thermographic patterns, due to limited technical knowledge of the devices, standardized protocols, and image/data processing. There is a lack of an acceptable classification technique for plantar thermographic patterns, with a particular emphasis on the foot vascular structure and circulatory condition. There is no objective way to categorize thermographic images into different groups [73]. When IR is exploited for clinical purposes, IRT measures have some drawbacks. The detection of bilaterally existent local problems in the same foot region at the same time. This can be seen in cases where an ulcer develops with a local temperature increase on the right hallux and a temperature increase on the left hallux (Figure 8). According to the study described in [65], the temperature difference between these places did not reach 2°C as a result. This constraint can be overcome, as revealed in this study, by further optimizing the algorithms based on a comparison of the ROI temperature with the mean foot temperature [74].

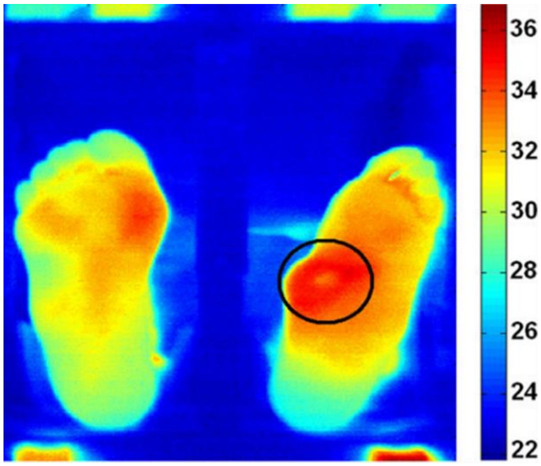

Figure 8: This patient, had an ulcer with a local temperature increase at the right hallux, but also increased temperature at the left hallux. The image was taken from [65].

Another limitation is the difficulty to detect lesions over in both feet at the same time. It is unclear if a patient has bilateral Charcot foot, bilateral osteomyelitis, or merely a pair of heated feet based on the thermal picture itself (e.g., due to the presence of neuropathy). This limitation may be addressed by merging multimodal images (also known as multiplex imaging, which refers to the simultaneous generation of signals for more than one imaging technique); however, it should be noticed that the chances of having such serious issues on both feet at the same time are extremely unlikely [65].

Furthermore, the utility of using absolute foot temperature values to detect symptoms of foot diseases remains unclear [75]. Because of age and sex differences, the existence of autonomic neuropathy or peripheral vascular disease, and environmental factors such as ambient temperature, and foot temperatures might vary from person to person [25]. Properly controlled investigations with sophisticated infrared imaging in large groups of volunteers are required to determine the utility of absolute foot temperature readings for diagnostic purposes. Such investigations should ideally take temperature readings from patients over time to detect intraindividual temperature trends and variations.

An intelligent telemedicine monitoring system, as utilized in daily clinical practice, would be the focus of IRT medical applications. Patient positioning, camera positioning, the need for additional imaging modalities, and automated picture registration and analysis are all technical difficulties that must be addressed. Feasibility studies are required to determine the most optimal requirements for such a system as well as its most successful implementation in regular activities [76,77]. Following that, the cost-effectiveness of implementing such a device to prevent diabetic foot disease must be determined. Advanced thermal imaging systems are becoming more affordable, but it is unclear whether they will be affordable enough for health facilities to use as a monitoring tool. In terms of recent developments and clinical trends, it is possible to conclude that thermography has become more popular in recent years. It is a great approach for tracking the progression of lesions, especially in disorders involving inflammation or ischemia areas, where thermographic instruments can easily capture thermal changes.

The studies presented in this section have all a major feature in common: they deal with temperature measurements on the skin surface. In IRT, the physical property of emissivity, which is unique to each material, is important to consider. The importance of skin emissivity in IRT research is discussed in the next section.

1.2.3 Human Skin Emissivity

The body's natural defense is skin, a biological barrier that protects us from the environment. In an ideal world, human skin would maintain a relatively constant temperature pattern over time, to maintain thermal balance. Long-term exposure to a variety of external factors (e.g., ultra-violet radiation or scars) leaves an impact on human skin, breaking and changing the thermal pattern with permanent hot/cold areas, which might compromise the appropriate interpretation of a thermographic image. Four mechanisms transfer human thermal energy to the environment [39].

1. Conduction is the transfer of heat energy from the warmest part to the coldest part through the tissue layers when two bodies of different temperatures come into contact.
2. Convection is the transfer of heat from the skin to the environment.
3. Radiation is a form of heat transfer that does not involve the use of a medium. Electromagnetic waves transport energy between two independent things at differing temperatures.
4. Sweat Evaporation is the process through which the body regulates its temperature by converting liquid to vapor. The temperature of the surface drops as a result of evaporation.

Thermal cameras display images based on the quantity of heat dissipated by IR radiation at the skin surface. The physical principle of these cameras lies in the conversion of the received electromagnetic radiation into electrical energy. Afterward, these signals are represented by gray levels or colors that represent temperature values. However, the energy absorbed by thermal cameras is dependent on several external factors, such as emissivity.

Since 1934, skin emissivity is an active research topic. The first research contribution related to skin emissivity was proposed by Hardy J. in [41], which described the transmission of infrared radiation through human skin. Even though different studies have reported varying values for the emissivity factor, human skin emissivity is relatively high and constant, almost identical to that of a black body. Emissivity is a measurement of a surface's ability to emit thermal energy efficiently: it is the percentage of energy emitted compared to that emitted by a thermally black surface (a black body). A black body is a material with an emissivity of one and is a perfect emitter of thermal energy. A perfect black body would be a material having an emissivity of 1. Human skin emissivity is reported to be nearly constant, with a value of 0.98 ± 0.01 for the near IR wavelength range of 2–14 μm [78]. Despite the color of the skin, the skin emissivity is the same, regardless of whether the emissivity determination trials were conducted *in vivo* or *in vitro*, as stated in [79]. Surface curvature does, however, influence the value of surface emissivity. Surface temperature measurement errors are minimal for viewing angles up to 45 degrees, according to [80].

While it is well known that the amount of thermal energy radiated by a surface is proportional to its emissivity, more recent theoretical and experimental results have demonstrated that emissivity is proportional to the viewing angle of the surface, i.e., the angle between the imaging axis and the normal to the surface. When the viewing angle is larger than 60°, the emissivity drops significantly, resulting in erroneous temperature measurements. Figure 9 presents the angular effect on temperature, reported in [81].

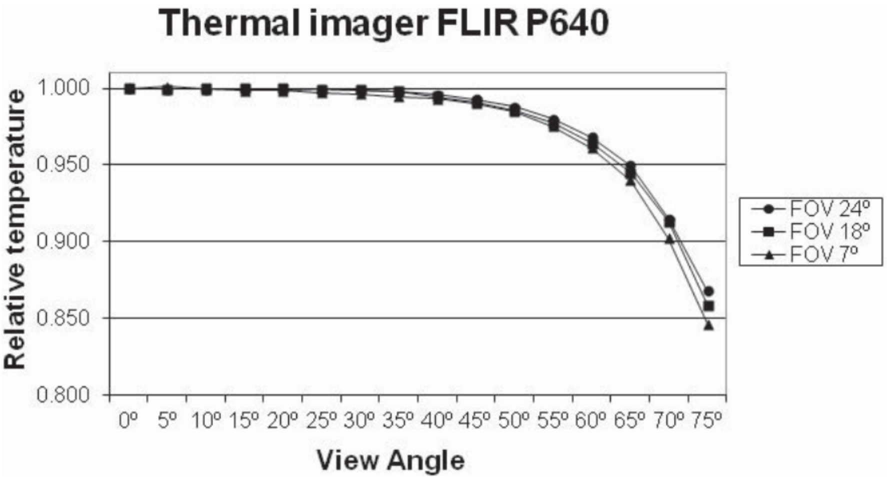

Figure 9: Relative temperature (i.e., normalized temperature) measurement with the same thermal imager and for three different FOVs as a function of viewing angle to the spheric black body [81].

The effect of emissivity according to the angle has been studied in several works employing 3D thermal reconstruction approaches. Some methods that are based on phantom investigations propose artificial neural network prediction approaches [82] as a solution to correct the emissivity effect according to the view angle

A local increase in skin temperature is usually associated with underlying pathology. To perceive correctly temperature differences, some adjustments must be made for any influence quantity that may impact the temperature to be measured in the image [83]. Variations in emissivity are unlikely to cause apparent temperature differences of more than 0.5°C for skin viewed at normal incidence. However, when skin is seen obliquely, the reduced emissivity can result in a 0.4°C drop in apparent temperature lower than 0.5°C, producing a ‘hot spot’ in this area undetectable on the thermograph. If possible, the skin should be examined normally during clinical tests, or the thermograph image should be compared for areas viewed at equal obliquity under comparable angles.

1.3 3D Imaging: A Medical Computer Tool

IR images, despite their two-dimensional nature, are appropriate and effective for providing physiological information. A 3D scanning technology, on the other hand, can create precise 3D spatial models of the area under investigation. Thermal evaluation of the plantar region of the foot using spot thermometers and/or thermal imaging has been proven to be beneficial withinside the prevention of diabetic foot ulcers [33]. Traditional cameras, on the other hand, are limited in terms of FOV and capture only a 2D view of the plantar facet of the foot, in which 50% of ulcers develop [4]. The thermal skin distribution must be expanded beyond 2D to improve ulcer detection. Our goal is to combine 3D models and thermal imaging to detect inflammation in diabetic foot disease. Table 5 gives an overview of the latest 3D medical modeling applications. Remarkably, 3D applications are starting to become increasingly popular. From segmentation and pattern recognition to modeling for 3D printing.

Table 5: Overview of the 3D reconstruction techniques based on visible-light images and/or IR images

Author	Year	Study
O'Dell et al [84]	2017	Sizing of pulmonary vessels from 3D medical images.
Chernov et al. [85]	2017	Breast reconstruction
Moriya et al [86]	2018	Unsupervised segmentation of 3D medical images
Sanches et al [87]	2019	Image fusion between MRI with IR images
Goudie et al [88]	2019	3D printed vasculature for simulation-based medical education.
De Queiroz Júnior and de Lima [64]	2020	Breast pathologies study
van Doremalen et al. [33]	2020	Diabetic Foot study
Bayareh et al. [34]	2021	Early diabetic foot diagnosis and treatment

1.3.1 Medical Imaging

Since its beginnings, photography has played a significant role in medicine, particularly in specialties like dermatology, where a visual interpretation is of prime importance. It is used as a way of detailed documentation of diseases or operations, as well as a communication and instructional tool. If medical images are used for teaching, gaining second views, monitoring treatments, and constructing image libraries to feed algorithms, they must be of the highest quality. This leads to the key goal: to help patients. Understanding and implementing basic photography concepts to normalize images is required for quality images. It is essential to be able to compare and contrast critical data out of visual information. Each specialty has its system of regulations, some of which are more formal than others [89]. The potential for using photography to improve medical care becomes limitless once the standards are met. An avalanche of concepts come to mind, each opening a new door and then another: comparison, extrapolation, projections, monitoring, post-processing, diagnosing, pattern recognition, big data, artificial intelligence, and facial recognition [45,90,91].

Dermatological images were among the first medical images to be repeatedly replicated for datasets intended to disseminate medical knowledge. In this way, photography had an important role in the development of dermatology as a field. Even though diabetic skin symptoms are present in up to 70% of patients with diabetes mellitus type 2 and are the first indication of vascular impairment, they are not well accounted for as part of the diagnostic. Figure 10 illustrates the evolution of a patient diagnosed with osteomyelitis with DM and DF background, the follow-up was performed with medical imaging documentation, in which there was no evidence of a systemic illness or metabolic instability.

Figure 10: Series images and radiographs of a 68-year-old man with type 2 diabetes osteomyelitis foot. The images were taken from [92].

Gradually, imaging for clinical follow perspective began to standardize, to distinguish medical from non-medical images, marking a subtle shift from creative depiction to this new scientific way of visualizing disease progression or treatment evolution. Among the 3D medical imaging techniques are radiology (i.e., X-ray, computed tomography) and magnetic resonance tomography. As already mentioned, medical imaging began with the discovery of X-radiation, which is a type of electromagnetic radiation capable of recognizing bone structures. As a result, X-rays are frequently used in medical imaging, particularly in the fields of dental care and chest imaging. To address the limitation that X-rays can only provide 2D perspectives, X-ray computerized tomography (CT) was developed to generate three-dimensional images on the inside of an object using computer processors. To obtain detailed cross-sectional views of the places inside the body, a succession of 2D X-ray images from various angles are taken. As a result, the produced images can contain more information than traditional X-rays, allowing physicians to examine individual slices within the 3D images. Since then, CT has become an important tool in medical imaging to supplement X-rays, and it is commonly referred to as a CAT scan [89,93]. Figure 11 gives an example of a CT scan of the foot in which the bioheating distribution was segmented and modeled for the study of the diabetic foot.

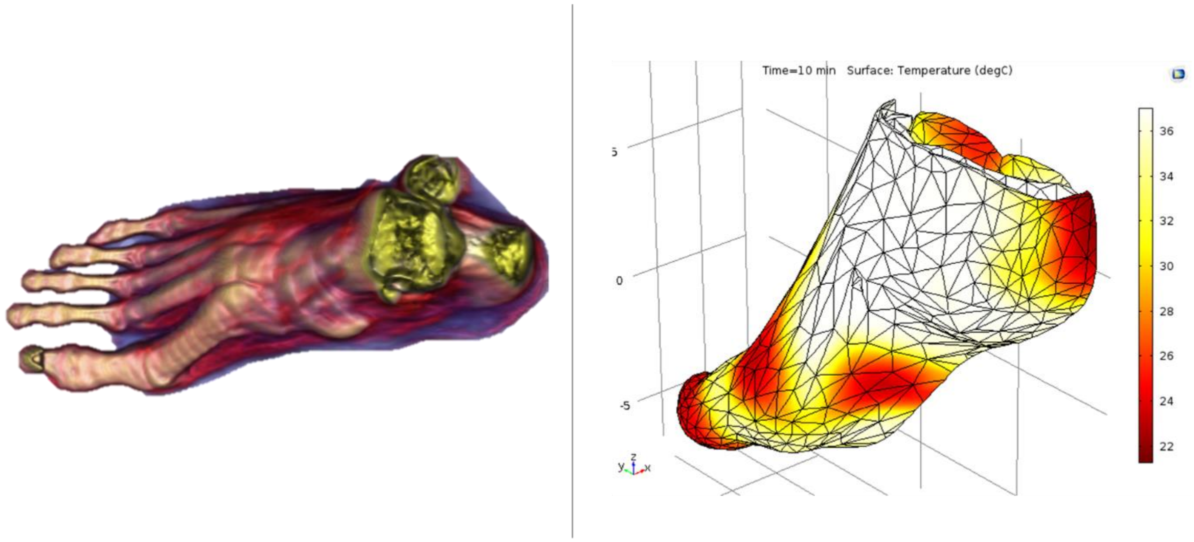

Figure 11: 3D model of the right foot obtained from a CT scan. A cut below the ankle was made to the original model. Bioheat distribution pattern at 10 minutes. The initial temperature of the skin layer was set at 15 ºC and the rest of the layers at 37 ºC. The images were taken from [94].

Although computed tomography (CT) has long been used to examine the human brain, it cannot examine functions, leading to the development of positron emission tomography (PET) and single-photon emission computed tomography (SPET). PET is a form of diagnostic imaging technique that creates a 3D image or picture representing the body's functional activity. PET is frequently used to evaluate and study neurological illnesses such as Alzheimer's and multiple sclerosis, cancer, and heart disease because of this advantage. These nuclear data are frequently completed by additional 3D images, for instance, provided by CT scanners. The different acquisitions are usually performed in parallel during the same session to display the bone structure of an object [93,95,96].

The arrival of magnetic resonance tomography (MRI), on the other hand, enhanced the earlier developments in medical imaging. MRI plays an important role in imaging organs such as the brain, muscles, heart, and malignant objects. MRI does not use ionizing radiation like CT scans or standard X-rays [97]. Figure 12 shows an example of 3D datasets of head images obtained by MR and IRT for a patient.

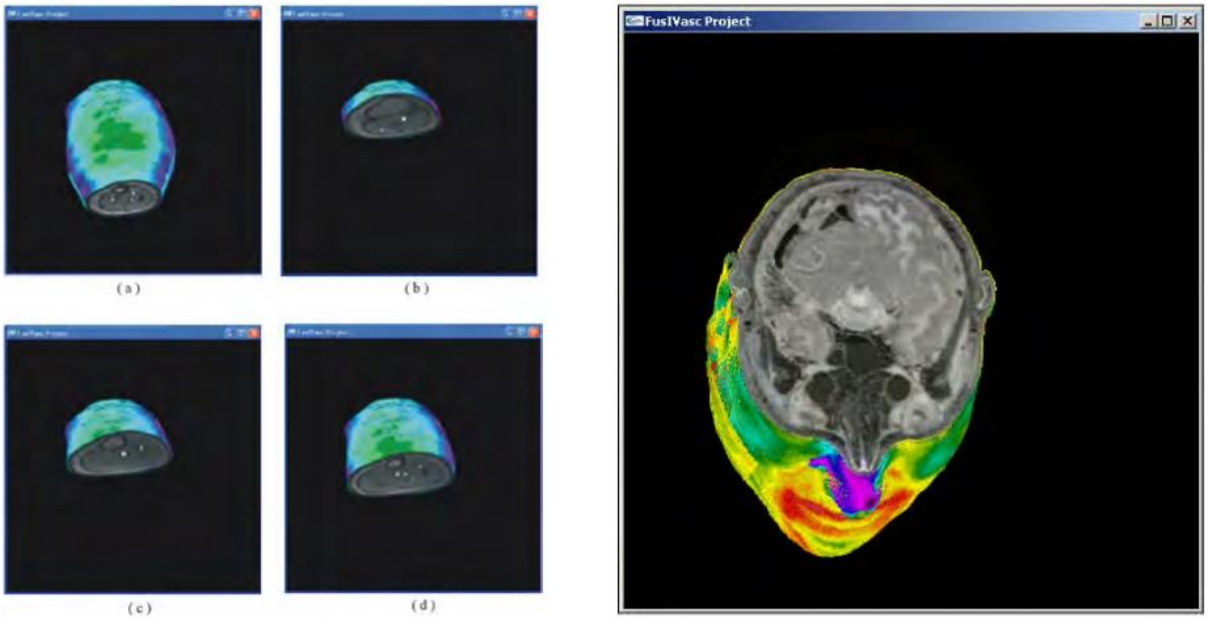

Figure 12: head visualization at dorsal root axial cut and visualization at four distinct cutting levels. In both cases, the MRI data is visible together with the surface temperature. The images were taken from [87].

Hybrid tomography is emerging by combining two imaging techniques, for example, IR/CT and IR/MR can present both functional and structural information inside one set of produced pictures to keep relevant features of each imaging approach. The next section will describe some advantages and applications.

1.3.2 Advantages and Applications

Early techniques displayed 2D image structures located inside the body; more complicated acquisition systems now allow the visualization of 3D images. Specialists can create a unique 3D thermal model by combining the precise geometry of the body surface area under study (surface data acquired with a 3D scanner) with 2D thermal photos. There are a few references in the literature concerning such a technique aiming at identifying DF complications, as well as a comparable system for breast cancer detection [64,94,98]. 3D imaging is a technological advancement that provides a significant benefit to clinical practice by providing morphology information with detail. From the geometrical point of view, a 3D model is more accurate than a 2D image and reduces the common distortion errors found in 2D photography. It is a valuable tool for measuring the size and the shape of lesions like tumors, scars, and ulcers, and it is appropriate for facial and breast exams since these comparisons make it easier to assess a tissue evolution, before and after a treatment, for instance [85]. The advantages of a 3D representation are the following [33,45,89,99–102]:

- It allows organ inspection using more realistic anatomical images, the identification of objects and structures, the appreciation of movements, and the estimation of boundaries.
- The evaluation of different views and positions of a surgical procedure.
- It allows more detailed analysis of the entire body, especially in areas with curved surfaces, allowing early detection and surveillance of malignant lesions.
- It provides a more realistic and in-depth vision than standard 2D images.
- Pathological issues are visualized, located, and assessed.
- It improves depth perception and simplifies surgical planning and training in laparoscopic surgery.

1.3.3 Technological Limitations

3D medical modeling has become a widely used technique in complex surgery (notably to simulate an intervention) and planning surgical operations. However, the 3D model accuracy, i.e., the similarity between the model and the original anatomical situation, remains unanswered in the existing research [103]. According to [89,104,105], the disadvantages of current 3D imaging techniques are the following:

- In IRT, 3D imaging is still in its early stages and must be validated before it can be used as a standard tool for facial and body mapping.
- It necessitates more advanced calibration methods.
- Certain systems still require the use of specific 3D cameras, which are not approved in operating rooms, as well as the use of special projection displays.
- The expensive costs of these 3D image systems, as well as the size of the equipment and the need for unique software, necessitate training, which can be a barrier.

1.4 Thesis Context

This thesis describes a method to achieve a 3D anatomical model by exploiting the fusion of IR and visible-light images associated with temperature information. In a comparison of the state-of-the-art, the novelty of this contribution lies in the automatic segmentation of radiometric arrays based on temperature threshold criteria under certain conditions. For this thesis, the RoI will be referred to as the plantar region of the foot; however, a set of images of the hand was employed to prove the limits of the algorithm. The advantage of processing radiometric data instead of a false-color image lies in the fact that the RoI (e.g., the foot or hand) can be delimited in terms of a set of temperature values, while the background can be set to zero. In this sense, it is possible to automatically segment a region with search criteria for a specific temperature range in a one-dimensional array, instead of processing a false-color image for a specific segmentation process. This method can automatically eliminate thermal interferences, detect the region of interest, and enhance the RoI contrast. In essence, the method was designed to automatically obtain merged images in which only the RoI would contain false colors, proportionally to the measured temperature.

In the context of the DF issue and the difficulty of early diagnosis, IR thermography has provided a supporting assessment tool. However, infrared cameras still have a significant drawback. When an image is taken, this image is 2D information. Ulcers developing on the dorsal side, for example, will be missed if the plantar side is scanned. The other half of the ulcers would go unnoticed because only half of them appear on the plantar side. Alternatively, multiple images could be taken, although automated temperature differences have only been proved to be achievable for the plantar side because only the plantar side can capture similar characteristics of both feet in one image. A multiple image strategy would also involve extra effort in evaluating thermal images, which might not be practicable in a busy clinical office or home monitoring setting. When completely developed, a 3D model may be able to address most of the shortcomings highlighted. With a 3D model, the feet beyond the plantar site can be shown in a single image. Furthermore, a model gives additional information that may aid clinical assessment and can be utilized to evaluate contralateral temperature differential on the plantar, medial, dorsal, and lateral foot sides automatically.

Due to medical IRT is still a technique that displays partial anatomical views and time consuming to inspect thermal images individually. A representation such as a 3D anatomical model can offer a solution of displaying multiple regions of the foot which could visualize regions of interest such as inflammations due to abscesses or temperature asymmetry segmented by regions; which are not usually visible when not yet diagnosed with diabetic foot [70]. Providing a 3D model of the foot with temperature information could be useful for fast assisting in the early detection of the diabetic foot along a comprehensive examination is required in the treatment and monitoring of the condition. The individual inspection of medical images could translate into time consumption for the physician to find relevant or significant information that could contribute to the evaluation and diagnostic criteria, so, in this thesis, we propose the possibility of implementing 3D models and we describe the methodology to associate temperature information, with the perspective of evaluation of the diabetic foot from multiple views.

However, while the proof of concept has been established in [33,34], the spatial and thermal precision remains unknown. Some medical diagnostic-oriented studies [102,106,107] indicated an accuracy error of less than 1 mm, which this study used as a baseline for its findings. On the other hand, other works have contributed to the study of the accuracy of multimodal fusion presented in

[108]; however, the segmentation in thermal images was performed manually. In conclusion, this work could contribute, as a perspective, to a new study to determine the 3D model's thermal accuracy using radiometric data processing and image registration to develop a digital assistance tool for the diabetic foot early diagnosis. Although several 3D thermography foot techniques have been created, they have never been employed in a medical setting. The current thesis purpose is to demonstrate for the first time how 3D thermographs could be effective in detecting inflammation in the diabetic foot, with the eventual goal of developing a fully established 3D thermography system in mind. This is investigated using an experimental setup that combines 3D imaging with established 2D thermal imaging modalities.

1.5 Thesis Objective

The perspective of providing 3D thermal models is to perform an early diagnosis of the physiological state of the foot as a single entity instead of a set of individual images before a visible alteration. Therefore, the objective of this thesis is to provide a 3D model of the foot with temperature information, based on the multimodal image registration with thermal images obtained by IR radiometric processing.

At the time of this work, the generation of 3D thermal models with a view to early diagnosis of the diabetic foot had limitations in terms of multimodal image registration. This limitation entails that the superimposition of images and data was carried out by a specialist, which represents a disadvantage in terms of the inspection time. The challenge in this thesis is defined as eliminating the manual procedure so that a collection of superimposed images is obtained from the processing of radiometric information prepared to reconstruct 3D surfaces.

A particular problem that drives to employ of radiometric processing is to enhance the contrast of the plantar area to enhance the detection and paring of key points. Traditional digital image processing cannot improve the contrast due to the false-color nature of the images. In other words, it is required to process the radiometric data before obtaining a high color contrast image.

A secondary problem, but not less important, is the elimination of thermal interferences that can compromise the paring of key points. In such a way, radiometric data processing can solve this problem in an automatic procedure without recurring to crop images by a user or specialist. Also, it is important to recall that thermal interferences can affect the contrast of the RoI, therefore can seriously compromise the surface reconstruction by pairing incorrectly key points.

Medical imaging has proven to be a suitable tool in disease diagnosis. IR thermography, one of the various modalities of medical imaging, has been able to identify temperature asymmetry in paired organs such as the foot [69,109]. Medical thermography, on the other hand, is still a 2D approach that needs analyzing a series of images that can vary in amount and convert into time costs for an appropriate diagnosis [33], moreover, each image only presents a partial anatomical region of the limb of interest.

A shape-based entity, such as a 3D anatomical model, can provide a solution for displaying several regions of the foot, allowing for the visualization of regions of interest such as abscess inflammations or temperature asymmetry segmented by regions, which are typically not visible when not yet diagnosed with diabetic foot by traditional inspection [70]. Therefore, providing 3D modeling with temperature data could be useful in assisting in the early detection of the diabetic foot when a thorough examination is required for treatment and monitoring.

1.6 Conclusions

IRT has proven the potential to measure surface temperature differences of a patient in a contactless way. It is a non-invasive technique that is not risky to the patient since it measures the temperature emitted by the patient’s body instead of providing energy (passive technique). The fact that thermography cannot provide under-skin imaging can be limiting since several authors have proposed the concept of IRT tomography, yet it can aid in symptom assessment and monitoring. Numerous medical disciplines, as well as other branches of health science, have published studies establishing their utility in the evolution of alterations due to pathological evolution. As the cost of equipment decreases, these studies are becoming increasingly common. The use of thermography is not new; it has been around since the 19th century. The study of thermography in multiple domains of medicine should continue to better comprehend its potential clinical applications and decide which disorders it might be useful for. Recent information suggests that it is gaining popularity as a non-invasive technology with no contraindications that are becoming more widely available.

This chapter included a comprehensive overview of the medical context and thesis goals, with a focus on diabetic foot complications, medical thermography, and 3D medical modeling with thermal data. The multimodal image registration is an essential approach for obtaining matching points between two different but sequential images to estimate the point cloud that will be used to create the 3D surface as a result of this project.

It is certain that 3D medical modeling has great potential and is currently expanding. However, depending on the discipline, application, and technology, the outcomes are produced in a variety of ways. The technological aspects of this thesis will be presented in the following chapter to accomplish the aim of providing a thermal 3D model.

Chapter 2

State of the Art of 3D Thermal Modeling Background

Contents

2.1 IR Thermography

This chapter provides an introduction to IR thermography and the integration with 3D modeling, which has proven to be a suitable option for the development of models in a variety of application domains in recent years, with a particular focus on the medical field.

The principles of IR thermography, as well as the standards for equipment used in medical applications, data gathering conditions, and protocols in patients, are covered in this chapter. Also, external factors that can affect skin surface temperature measurement including relative humidity, ambient temperature, air currents, and thermal interference, are described to take into account in medical thermography. The information provided by the cameras varies depending on the technology used; nevertheless, this study focused on radiometric data-gathering devices. This section also compares and contrasts several current image processing techniques with the thesis proposal, which is the treatment of IR radiometric data. This data is collected in the form of matrices. They can be acquired only as digital information from electrical signals, or they can be expressed as temperature. The main advantage, as explained in Section 2.2.4, is the segmentation and color correction when the data is treated prior as a signal instead of a false-color image. The procedure to construct a false-color image from radiometric data is detailed in the section mentioned above. A highly contrasted region of the area of interest will be recreated from the data processing, with a homogeneous image background. Over this, the RoI can be retrieved against a transparent background. Segmentation is the result of this step, and it provides relevant data for multimodal fusion of visible spectrum and false-color images (i.e. thermal images). State-of-the-art studies will be outlined in terms of methods, applications, and accuracy. The merged images are required for the 3D reconstruction stage, for which this chapter explains the principles employed in this project (i.e. Structure from Motion and Multiview Stereo).

2.1.1 Principles

In recent years, IRT has attracted attention as a viable and reliable method for addressing complicated non-destructive testing issues in objects and buildings. However, from the perspective of preventative and corrective medicine, applications have expanded to medical use.

Electromagnetic radiation is emitted by all objects with a surface temperature greater than absolute zero. The wavelength and intensity of such radiation can be used for characterization. Both of these parameters are correlated to the object's surface temperature by relatively basic physical rules. The intensity (Q_λ) and wavelength (λ) of radiation emitted by an item can thus be used to determine its surface temperature without the requirement for physical contact [110]. Radiation with a peak intensity of 10 μm is emitted by an object at room temperature (290 K). The radiation generated by such cool objects in the visible band (400 nm to 700 nm) is below the threshold that human eyes can detect. Most objects in the environment are only visible because they reflect light in the same waveband as that emitted by the sun. IRT technique detects energy emitted by the subject and translates it to temperature variations. The result is a transient thermal image from the sample. In electromagnetic bands, IR refers to the radiations that fall between visible and microwave wavelengths.

The Long Wave IR (LWIR) spectral band, often known as the thermal imaging region, is useful for medical IRT. Sensors can provide a completely passive image of objects that are only slightly warmer than room temperature (e.g. human body) using only thermal emissions and no external lighting or infrared illuminator [42].

The relevance of the IR spectrum as a form of heat radiation was discovered by Herschel in century 19th century, in which this electromagnetic spectrum was called the thermal spectrum. The latter spectrum was discovered during a study of the new optical material by testing samples of crystals and colors that provided similar reductions in brightness. Several samples passed heat that could cause eye damage after only a few seconds of observation [43]. Currently, thermographic equipment uses an array of sensors known as bolometers, invented by Samuel Langley in 1880. The sensor consisted of a thin darkened plastic ribbon connected to a Wheatstone bridge on which infrared radiation was focused and to which a sensitive galvanometer responded. An array of bolometers generates an array of radiometric data, which is represented as a false-color image equivalent to the intensity of IR energy detected within the capture region [45].

Several laws of radiation were postulated by Kirchhoff, Stefan-Boltzman, and Plank, after the discovery of heat radiation in electromagnetic waves [110]. All objects with temperatures above absolute zero will emit electromagnetic radiation from the surface. The emitted radiation is described by the intensity and the wavelength, which are used to measure surface temperature in a contactless way. The intensity of radiation emitted by a body is described by Planck's distribution in Equation (1) [110]:

$$Q_\lambda = A \,/\, \lambda^5\left(e^{(B/\lambda T)} - 1\right) \qquad (1)$$

where Q_λ is the emitted radiation [W], λ is the wavelength (m), T is the surface temperature [K], and the Plank constants A = $3.742\text{x}10^8$ W μm^4 $\text{m}^{-2}$and B = $1.439\text{x}10^4$ µm K.

For bodies with different surface temperatures, Equation (1) gives a set of curves that characterize the amount of radiation emitted at each wavelength (λ). Integrating Equation (1) over the entire wavelength range provides the total radiation emitted by a body, given by Equation (2).

$$\varepsilon = e'\sigma T^4 \qquad (2)$$

where ε is the radiant emittance [$\frac{w}{m^2}$], e' is the effective emissivity (a value between 0 and 1), σ is the Stefan-Boltzmann constant ($\sigma = 5.67x10^{-8}\frac{w}{m^2k^4}$), and T is the absolute temperature [K].

All detectors are subject to the same principles presented in this section, The following section presents the distinction between IR cameras and the several detectors.

2.1.2 Infrared Camera and Detectors

Thermal cameras use principles of IR radiation to create images. Heat is produced by all objects and organisms, known as thermal IR radiation, which is a kind of light that is undetectable. A thermal camera acts as a heat sensor, detecting temperature variations between objects and within the scene. Thermal images are a visual representation of heat rather than a visible spectrum image. The brighter an object appears in a thermal image; the more IR energy emits [45]. In most situations, images are generated in grayscale, with darker portions indicating colder temperatures and lighter areas indicating warmer temperatures. Color palettes can be used to enhance the image contrast among a set of different colors, as depicted in Figure 13.

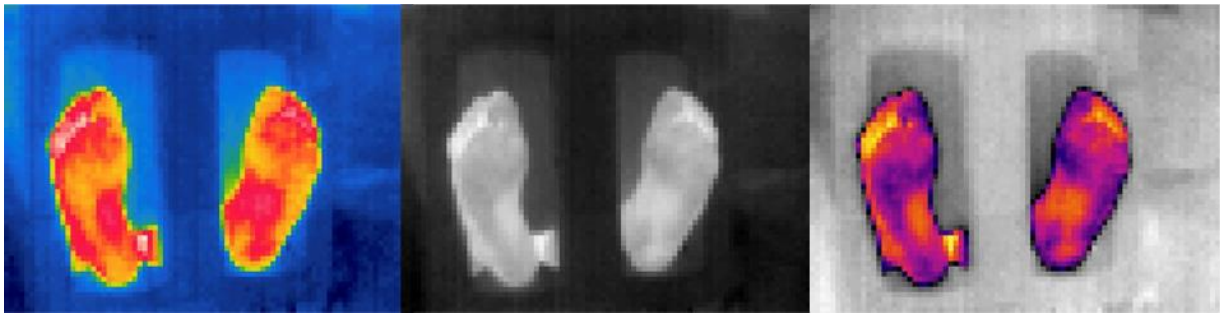

Figure 13: thermal images from the feet. From left to right, the color palettes are rainbow (also known as spectral or JET), gray scale, and iron. The image was taken from [111].

Thermal imaging is not a new concept. Until recently, though, the costs were exorbitant. As a result, outside of the military, law enforcement, and high-security locations, practical applications were limited. New sensors have led to improvements. Streamlining sensor manufacture and improving lens materials are increasing volumes and lowering prices. Thermal imaging is now used in a variety of industries, including the infrastructure industries, as well as medical applications [112].

The IR radiation spectrum, which includes elements of the electromagnetic spectrum beyond visible light, is frequently classified into the following subregions (see Table 6):

Table 6: IR subregions on the spectrum band [113].

IR Classification	Wave length [µm]
Short-wave infrared	1.4 to 3
Mid-wave infrared (MWIR)	3 to 8
Long-wave infrared (LWIR)	8 to 15
Far-wave infrared (FWIR)	15 to1000

The MWIR band is frequently referred to as thermal in the thermography field. However, due to the strong spectrum absorption of the atmosphere in this range, the wave band is useless for thermal imaging. The electromagnetic spectrum is frequently divided in the thermal imaging sector based on the response of various IR detectors (Figure 14).

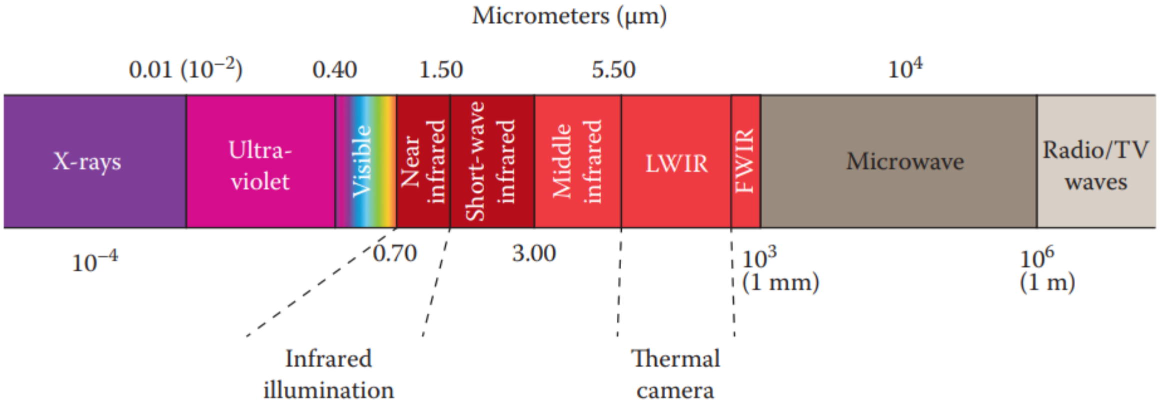

Figure 14 Bandwidth spectrum, the image was taken from [113].

The energy of IR radiation is captured by an IR detector, which absorbs and transforms it into a measurable quantity. IR detectors are divided into two types with a specific classification [70]:

- Thermal or bolometer detectors.
- Quantum type or the photon detector.

Bolometer detectors are low-cost and do not rely on wavelength; however. they perform poorly when mass-produced in large quantities. To a major measure, their price is influenced by the cooling system (they are often temperature stabilized using Peltier elements). The photon detector of the quantum type, which is wavelength dependent, requires complex cryogenic cooling methods and has a low production volume at a high cost. They have a higher sensitivity and reaction time than bolometer detectors [113]. Bolometer detector technology was applied in this thesis project, involving thermal imagers model: Fluke Ti32 and Lepton 3.5.

Thermal imaging sensors with suitable performance specifications are now available. The MWIR band and the LWIR band are two different spectral bands that provide adequate thermal sensitivity for medical purposes [91]. Both bands have a significant advantage over the other in medical applications, although the LWIR is quickly becoming the most cost-effective sensor technology. Some researchers believe that employing both bands has advantages [31].

MWIR cameras are widely accessible and generally have more pixels, resulting in superior resolution. This spectral band has been highly successful in detecting small tumors and temperature abnormalities. Cryogenic temperatures as low as -195°C are required for MWIR sensors. Some MWIR sensors use thermoelectric coolers, which operate depending on the image processor architectures. MWIR sensors detect radiation from a wide range of sources, including the sun, as well as emitted radiation from thermal sources. Reflected light, rather than emitted radiation, can generate structure in images in this spectrum. Spectrum light sources, such as incandescent light bulbs and sunlight, must be avoided as much as possible. Undesirable light in the image might result in shadows, reflections, and bright spots. Wideband artificial sources and sunlight (IR image interference) should not be used to illuminate the subject directly. Before gathering data for the record, it is advisable to experiment with lighting geometries and sources. It is also important to avoid moisturizing lotions, sweat, and other skin surface coatings [52,112,114]. Since the introduction of uncooled thermal imaging arrays, the LWIR camera's popularity has increased. The current state-of-the-art differs significantly from what was accessible in the 1970s. LWIR cameras are becoming more common, and they can compete with thermoelectrically cooled MWIR cameras in terms of price and performance. Thermal cameras that are not cooled are small and offer adequate resolution and sensitivity for medical applications. Cameras having 320 240 pixels, for example, may be acquired for less than USD $10,000. Shadows, illumination, and reflections have a much lower impact on sensors in this band. However, before gathering data for the record and dissemination, it is advisable to experiment with viewing geometry, ambient illumination, and skin condition [45,70,112,115]. Figure 15 compares two images taken in the MWIR and LWIR spectral ranges. The image was obtained from [116].

Figure 15: In certain scenarios, such as when there are hot targets, LWIR can outperform MWIR. Burning barrels, as illustrated in this figure, is a clear demonstration of the LWIR advantage. With large energy in the MWIR, hot targets shift left on Planck's curve, yet the LWIR image remains functional with burning barrels in the field of view [116].

A thermal camera sensor is characterized by a large number of detectors that are sensitive to thermal infrared radiation. The thermal IR information is detected, recorded, and then converted into electrical impulses by the sensor. The measurements are converted into images. Thermal imaging detectors, independently of the wave length, are classified into two categories: cooled and uncooled infrared sensors [45].

Uncooled IR image sensors are compact and have more mechanical moving components than their cooled counterparts, making them less expensive. Cameras with cooled sensors, unlike cameras with uncooled sensors, need to be maintained regularly, while newer systems based on sterling electronics require less maintenance. In addition, every 8,000–10,000 hours, the cooling medium must be replaced [110]. Individual elements in an uncooled sensor respond to incoming IR radiation in different ways, resulting in "drift" in individual pixel values. The sensor corrects this by performing nonuniformity correction. The sensor is blocked by a mechanical shutter, which sets a standard temperature target against which every pixel is corrected. This occurs at regular intervals or in response to a specific temperature change. Figure 16 shows an example of a thermal camera shutter of the Lepton 2.5 and the correct calibration of the uniformity correction.

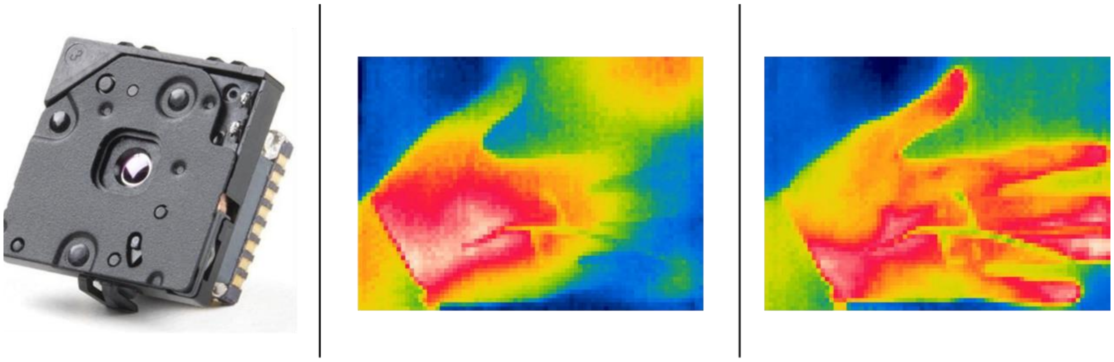
a) b) c)

Figure 16: a) Lepton 2.5 LWIR microbolometer sensor: This model contains a micro shutter between the lens and the chassis, b) thermal image with drifting pixels, and c) thermal image after shutting and opening the shutter for pixel correction. The samples were taken from the thesis [117].

An LWIR uncooled thermal camera sensor does not require cryogenic cooling. Using less sophisticated temperature control devices or no temperature control at all, the uncooled IR sensor is stabilized at or close to room temperature. Microbolometer technology is used in a common design. This is usually a small resistor (or thermistor) on a thermally insulated silicon device with extremely temperature-dependent characteristics. Vanadium oxide (VOx) or amorphous silicon (α-Si) are used to make the resistor [118].

A Focal Plane Array (FPA) refers to an imaging system, which is made up of individual detector picture elements, i.e. pixels. Although the definition can be used for both linear dimensional and two 2D arrays, it is most applied to the latter. In most optoelectronic imaging devices, the optics section is confined to focusing the image onto the detector array. Electronically, these so-called staring arrays are scanned, usually with circuits built into the arrays [119]. Figure 17 illustrates and schematic of the function of a thermal sensor. The image was taken from [113].

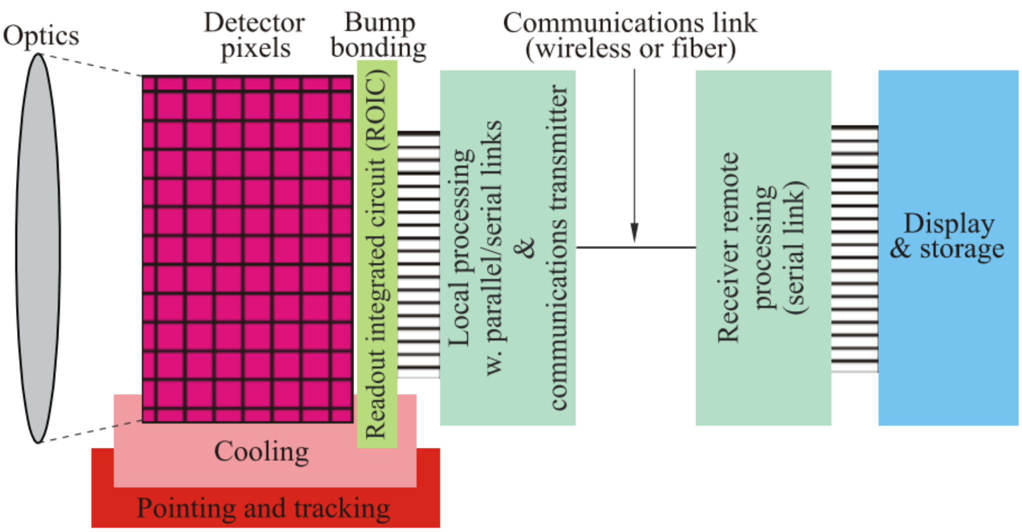

Figure 17: An imaging system is depicted schematically, with subsystems highlighted from the optics to the display and storage block [113].

2.1.3 Image Formats

Thermal images are most often displayed in greyscale, so the variable-temperature data is converted into a digital image with grayscale values (12 or 16 bits). The most typical presentation (or palette) is white/hot, in which heat sources are white against gray and black backgrounds of lower temperatures. In some circumstances, black/hot, which makes heat sources seem black, may be more convenient to utilize [45]. Thermal images are commonly linked with vivid, strong hues, which may appear unusual given that the camera operates beyond the visible light spectrum. Because the human eye can distinguish between distinct shades of color better than different shades of gray, adding color to thermal images can sometimes help the user to identify temperature differences. The intensity temperature acquired by the IR radiation sensor is used to create these false-color images. Each color or hue reflects a distinct temperature, with white and red representing higher temperatures and green, blue, and violet representing lower temperatures [61]. Nevertheless, different color palettes (e.g. JET, Viridis, Parula, etc.) are available to visualize temperature.

Thermal imaging is currently being used for research and development into the identification of diabetic foot, as well as for screening and tracking of ulcer progression. The latter is the least stressful and most cost-effective option due to the integration of the multimodal sensor (IR and visible light sensors) into one single device. Uncalibrated static images and simple uncalibrated video (images taken before calibration, controlled environment, or without emissivity settings) are two forms that can be useful in this situation. These formats can be saved and archived for later use. It is not suggested to use such visuals for rigorous studies [21,55,65] where temperature values are important. Figure 18 shows uncalibrated images of the foot, demonstrating how an uncontrolled environment can influence rigorous studies.

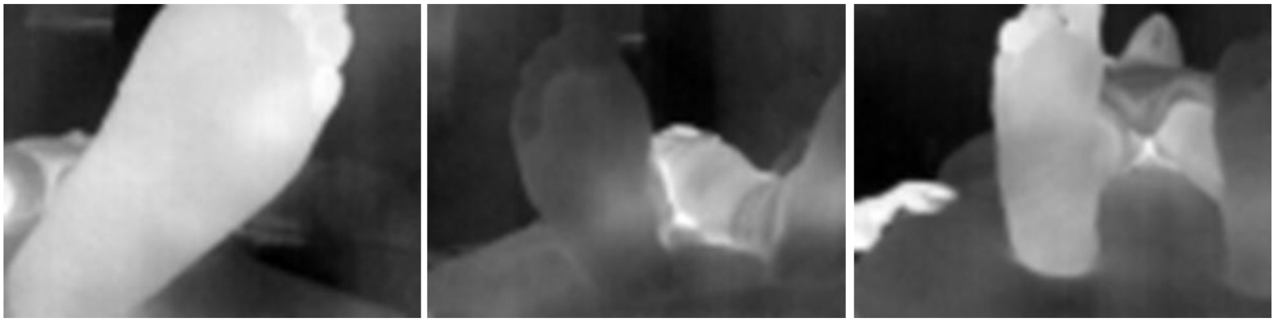

Figure 18: Images taken with the Lepton 2.5 sensor which have not been calibrated. These images were generated by reconstructing raw information recorded through digital processing. The RoIs (i.e. de plantar foot) are eclipsed by other regions, such as the volunteer body or surrounding people, with higher intensity in all three cases. The temperature interferences due to wrong data or image acquisition may challenge data processing from the perspective of a quantitative point of view. The images were taken from [67].

It is relevant to collect calibrated radiometry data in lossless archival formats (e.g., the so-called “raw” format that a thermal camera offers as a data array) for medical studies in which images and information are to be saved, shared, and used for the testing of software and medical theories, or to explore future studies [67,120]. Commonly, the radiometric data arrays are stored in a TXT matrix to be processed by several programming languages. Thus, a radiometric thermal camera with uncompressed standard formats or “raw” output that keeps the thermal calibration is preferable to buy or rent. This type of information enables the medical facility to convert its thermal images into a standard format for distribution to other medical facilities. Figure 19 depicts an illustration of a raw thermal array and its digital image reconstruction. The reconstruction is done by characterizing the sensor with a black body under very controlled environment standards. In such a way, the characterizing would prove a mathematical mode that predicts each pixel temperature based on the radiometric array.

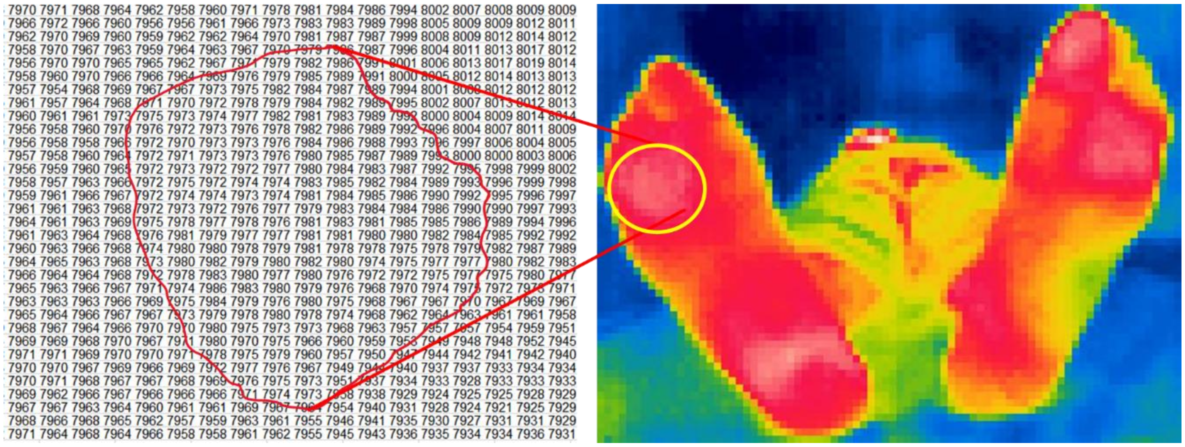

7970	7971	7968	7964	7962	7958	7960	7971	7978	7981	7984	7986	7994	8002	8007	8008	8009	8009
7966	7972	7966	7960	7956	7956	7961	7966	7973	7983	7983	7989	7998	8005	8009	8009	8012	8011
7962	7970	7969	7960	7959	7962	7962	7964	7970	7981	7987	7987	7999	8008	8009	8012	8014	8012
7958	7970	7967	7963	7959	7964	7963	7967	7970	7979	7986	7987	7996	8004	8011	8013	8017	8012
7956	7970	7970	7965	7965	7962	7967	7971	7979	7982	7986	7991	8001	8006	8013	8017	8019	8014
7958	7960	7970	7966	7966	7964	7969	7976	7979	7985	7989	7991	8000	8005	8012	8014	8013	8013
7957	7954	7968	7969	7967	7967	7973	7975	7982	7984	7987	7989	7994	8001	8008	8012	8012	8012
7961	7957	7964	7968	7971	7970	7972	7978	7979	7984	7982	7989	7995	8002	8007	8013	8012	8013
7960	7961	7961	7973	7975	7973	7974	7977	7982	7981	7983	7989	7992	8000	8004	8009	8014	8014
7956	7958	7960	7970	7976	7972	7973	7976	7978	7982	7986	7989	7992	7996	8004	8007	8011	8009
7956	7958	7958	7966	7972	7970	7973	7973	7976	7984	7986	7988	7993	7996	7997	8006	8004	8005
7957	7958	7960	7964	7972	7971	7973	7973	7976	7980	7985	7987	7989	7993	8000	8000	8003	8006
7956	7959	7960	7965	7972	7973	7972	7972	7977	7980	7984	7983	7987	7992	7995	7998	7999	8002
7958	7957	7963	7966	7972	7975	7972	7974	7974	7983	7985	7982	7984	7989	7993	7996	7999	7998
7959	7961	7966	7967	7972	7974	7974	7973	7974	7981	7984	7985	7986	7990	7992	7995	7996	7997
7961	7961	7963	7968	7972	7973	7972	7976	7977	7979	7983	7984	7984	7986	7990	7990	7997	7993
7964	7961	7963	7969	7975	7978	7977	7978	7976	7981	7983	7981	7985	7985	7986	7989	7994	7996
7961	7963	7964	7968	7976	7981	7979	7977	7977	7981	7981	7980	7980	7982	7984	7985	7992	7992
7960	7963	7966	7968	7974	7980	7980	7978	7979	7981	7978	7978	7975	7978	7979	7982	7987	7989
7964	7965	7963	7968	7973	7980	7982	7979	7980	7982	7980	7974	7975	7977	7977	7980	7982	7983
7966	7964	7964	7968	7972	7978	7983	7980	7977	7980	7976	7972	7972	7975	7977	7975	7980	7977
7965	7963	7966	7967	7971	7974	7986	7983	7980	7979	7976	7968	7970	7974	7975	7972	7978	7971
7963	7963	7963	7966	7969	7975	7984	7979	7976	7980	7975	7968	7967	7967	7970	7967	7969	7967
7965	7964	7966	7967	7967	7973	7979	7978	7980	7978	7974	7968	7962	7964	7963	7961	7961	7958
7968	7967	7964	7966	7970	7970	7980	7975	7973	7973	7968	7963	7957	7957	7957	7954	7959	7951
7969	7969	7968	7970	7967	7971	7980	7970	7975	7966	7960	7959	7958	7949	7948	7948	7952	7945
7971	7971	7969	7970	7970	7971	7978	7975	7979	7960	7957	7950	7947	7944	7942	7941	7942	7940
7970	7970	7967	7969	7966	7969	7972	7977	7976	7967	7949	7944	7940	7937	7937	7933	7934	7934
7970	7971	7968	7967	7967	7968	7969	7976	7975	7973	7951	7937	7934	7933	7928	7933	7933	7933
7969	7962	7966	7967	7966	7966	7966	7971	7974	7973	7938	7938	7929	7924	7925	7925	7928	7929
7967	7967	7963	7964	7960	7961	7961	7969	7967	7964	7954	7940	7931	7928	7924	7921	7925	7929
7968	7966	7968	7965	7962	7957	7959	7963	7961	7955	7946	7941	7935	7930	7927	7931	7931	7929
7971	7964	7968	7964	7966	7958	7958	7961	7962	7955	7945	7943	7936	7935	7934	7934	7936	7931

Figure 19: The raw Lepton 2.5 sensor data is stored as a 14-bit data array, and a false-color thermal image with a Jet (rainbow) palette is reconstructed from it. Any radiometric camera, such as the Fluke Ti32 model used in this study, can produce these formats reduced in terms of bytes towards a digital image.

If required, image editing software tools can be used to adjust image properties such as manual cropping or scaling. The data, on the other hand, can be sent in a variety of uncompressed formats to be processed [47]. If medical research facilities are to share common databases, they must adopt standard formats. Although thermal images are being researched for several medical applications where dynamic phenomena are of interest, there is no clear requirement for diabetic foot studies at this time [31].

2.1.4 Dynamic Range

The dynamic range of a camera determines the capacity to preserve precise temperature resolution in the presence of a wide temperature fluctuation in the image. The image digitalization and formation electronics in the camera determine the dynamic range. It is advised to use a camera with a suitable resolution of bits for image digitization. Commonly, most commercially available cameras have a pixel resolution of 12 bits or greater. This is enough for preserving fine detail in human body images. When acquiring images, it is recommended that nothing in the sensor field of vision is much cooler or hotter than the subject; that is, avoid scene temperature differences of more than 30°C (e.g., lamps, refrigerators, or radiators in the background could cause trouble). This is like trying to take a picture of a person standing next to headlights with a visible digital camera. Large temperature fluctuations often stress the image generation process, and undesirable artifacts may develop. Nonetheless, designing a collection environment with a limited temperature variation is rather simple. Covering the sensor field of vision with the human subject is a straightforward technique to do this [45,121]. For example, Figure 20 illustrates the differences between Lepton 2.5 and 3.0 dynamic range for the same subject to illustrate the concept. For the Lepton 3.0, used for this thesis, different features are presented in Table 10. The main difference is the number of pixels, which Lepton 3.0 has double the resolution of than Lepton 2.5 counterpart.

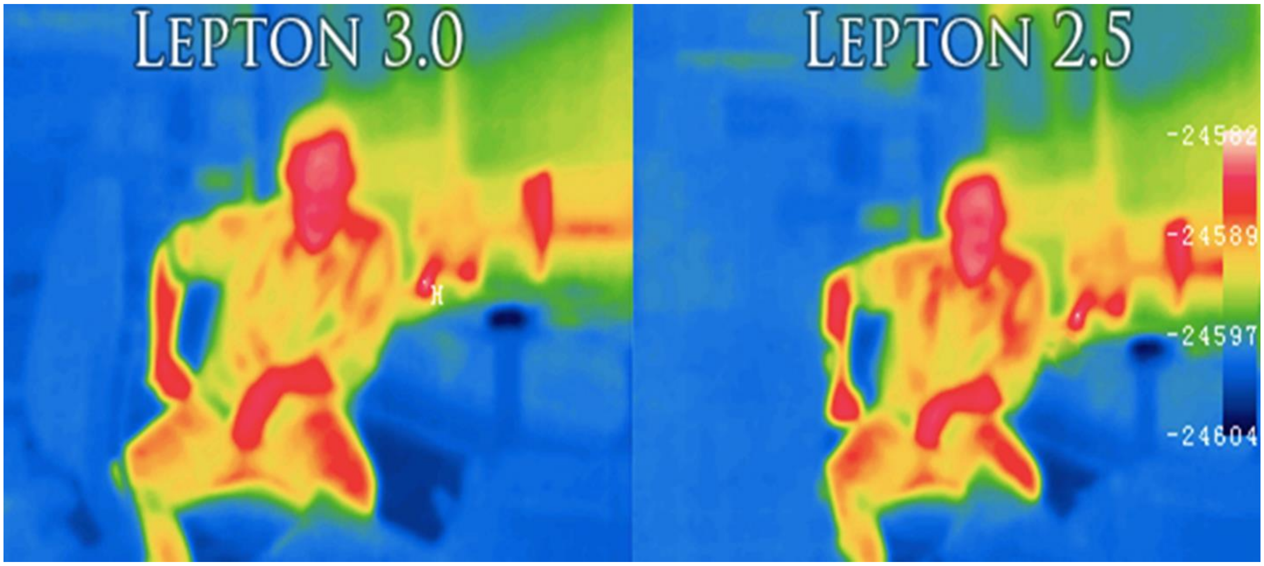

Figure 20: Dynamic range comparison between Lepton model 3.0 and 2.5. Both images are represented in Jet palette color [122].

2.1.5 Resolution and Accuracy

To assess the appropriate use of thermography, two factors must be considered: first, the accuracy of thermal images in patients, and second, the incidence of normal and abnormal thermograms in asymptomatic patients, as well as the presence or absence of temperature asymmetry.

The temperature is given on a scale, for example in degrees Celsius. The accuracy is measured in tenths of a degree. Sensitive sensors can detect temperature variations lower than 0.025 degrees. Because local temperature fluctuations produced by tumors and angiogenesis are frequently higher than this, this sensitivity is considered important for medical diagnosis [71]. The displayed colors are proportional to the measured temperature, in such a way that the highest color (e.g. red for Jet palette) of the scale will be assigned to the maximum temperature and the minimum color (e.g.

blue for Jet palette) will be assigned to the minimum temperature. The color distribution smoothness depends on the sensor temperature resolution and size. The sensor spatial resolution is mostly influenced by the pixel size. Thermal cameras with 320x240 pixels are fairly affordable, and the images from such sensors can be quite acceptable for informal inspection; nevertheless, images magnified may appear grainy unless the viewing area or field of vision is lowered [123,124]. The medical images will have useful thermal and spatial information since to the high accuracy and pixel resolution. In conclusion, while 320x240 imaging is appropriate, higher pixel counts allow for more flexibility in casual use and are needed for medical research. Larger pixel counts have advantages in consumer digital photography and military applications, but megapixel arrays in medical screening have yet to be established as a clear necessity. Temperature resolution of at least a tenth of a degree is suitable for most medical studies [43,45].

2.1.6 Emissivity Properties

As previously stated in Section 2.1.1, a blackbody represents the limit of a source's overall spectral exitance at any given temperature. Anybody with a temperature greater than absolute zero emits infrared radiation as a result of changes in atomic and molecule vibration and rotation states. Conduction, convection, and radiation are all characteristics of transferring heat. Thermographic imaging systems use the last characteristic (radiation). It should also be emphasized that, particularly in medicine, circumstances requiring the measurement of moist surface temperatures may arise, such as in the case of fresh wounds. It must address the scanned surface's physical qualities, such as emissivity or transparence, as well as external environmental conditions, such as the ambient temperature. It must additionally consider current external sources of infrared radiation as well as background radiation [80,110,125]. An emissivity is a number between 0 and 1. A black body or perfect radiator is an object that emits the most amount of infrared energy possible at a given temperature. It has an emissivity of one (100%). An item with an emissivity of 0.8 emits only 80% of the maximum theoretical amount of infrared light.

The emissivity and reflectivity of the measured surfaces is fundamental features. In thermography, when it comes to medical applications, these characteristics are essential. The detection and analysis of IR radiation emitted from the studied object that corresponds to its temperature is the essence of surface temperature measurement using a thermal camera. To understand the principles of emissivity, Wien's law and the Stefan-Boltzmann law in Equation (2) must be considered.

In 1968, Watmough and Oliver established that human skin with a depth of 2μm to 5.4μm thickness has an emissivity of Q_λ = 0.98 in normal incidence [126]. Emissivity was measured using a method involving an Aga IR scanner, averaged over tiny regions ~2 cm^2. The approach entails measuring the apparent temperature differential ΔT' between a black body cavity and a patch of skin that has been set to the same surface temperature as the black-body cavity. The use of a surface thermometer enhances the blackbody temperature. The skin and black body were placed in the same plane, one on top of the other, in front of the thermal scanner. The isotherm circuit built into this instrument is used to measure $\Delta T'$. Equation (3) describes the emissivity of both objects assuming the skin and black body are both at temperature T, there is an apparent temperature differential $\Delta T' = T_1 - T_2$, where T_1 is the black body apparent temperature and T_2 is the skin's apparent temperature. If Q_1 is the energy received from the black body, and $\varepsilon = \varepsilon_1$, Q_2 is the energy received from the skin, and $\varepsilon = \varepsilon_2$, then:

$$\varepsilon_2 = \left(1 - \frac{12.5\Delta T'}{T_1}\right)\varepsilon_1 \tag{3}$$

Equation (3) shows that $\varepsilon_2 \approx 0{\cdot}98$ at normal incidence according to Watmough and Oliver's study [126]. Although this study has been a reference in most medical IRT studies, the study of skin emissivity continues to be the subject of studies that depend on factors such as the angle of capture or humidity in open wounds. Because of the high air transmittance and short measurement distance, atmospheric radiation can be ignored in measurements of the human body. In other words, mirrored radiation provided by ambient temperature, i.e. electromagnetic waves reflected from the studied area, whose wavelength corresponds to the temperature of surrounding objects and the background, may impact the resulting value of the temperature of the measured body [46].

A clean human skin has an emissivity of 0.98. This number is based on several studies [80,110,127]. The temperature measurement is accurate only when the emissivity value is well defined. This is because emissivity affects the measured surface temperature. According to [128], surface temperature T detected by IR sensors can be described by Equation (4).

$$T = \sqrt[4]{\frac{\frac{q_{ck}}{\sigma}+T_{amb}^{4}-(1-\varepsilon)\cdot T_{mir}^{4}}{\varepsilon}}, \qquad (4)$$

where T_{amb} is the room temperature, T_{mir} is the mirrored temperature, q_{ck} is the density of the heat flow between the object and thermography equipment, ε is the emissivity, and σ is the Stefane-Boltzmann constant.

Several factors can influence thermography results, including the professional technical skill, the thermal imager characteristics, environmental conditions such as temperature, relative humidity, and wind speed, the electric current load of the equipment being studied, and angular emissivity [82]. Some mathematical models evaluate the effects of these factors and allow to obtain of reasonably accurate temperature measurements using infrared thermography. However, the angular position factor of the thermal imager over the examined subject influences the results. In addition to the object's susceptibility to angular emissivity, there is evidence that the thermal imager viewing angle features create measurement inaccuracies. The amount of heat energy radiated by a surface is likewise determined by its emissivity [82,129,130]. The emissivity of a surface is dependent on the viewing angle, or the angle between the optical axis and the normal surface. According to theoretical and experimental results, when the viewing angle is extended above 60°, the emissivity drops significantly, resulting in erroneous temperature mapping [82,131].

According to the studies reported in [130], the results show that the positional emissivity linear formula is a reasonable approximation for measurement error, and the normalized error curves shift consistently with viewing angle at different temperatures, as shown in Equation (5).

$$\Delta T = \frac{T_n - T(\theta)}{T_n - T_a}, \qquad (5)$$

where ΔT is a normalized temperature level with a range between [0,1], T_n is the temperature viewed at a normal angle, i.e., the measured temperature at the central point of the curved surface, at which the viewing angle concerning the camera axis is 0°. T_a is the room temperature, and $T(\theta)$ is the temperature recorded and a specific angle.

2.1.7 Blackbody

All structures are composed of atoms that are constantly vibrating. Electromagnetic waves are produced by the oscillation of charged particles, including atoms. The increment of the temperature of an object depends on the spectrum of radiant energy, which also depends on the vibration of the particles. As a result, all materials emit radiation at a constant rate with a wavelength distribution that is determined by the object temperature and spectral emissivity $E(T)$. Each material reflects IR energy differently, so these properties must be considered in a theoretical model body with ideal radiation properties known as a blackbody. A black body is capable of emitting IR energy, this property is known as emissivity. However, no material can be described as the perfect IR emitter source. Emissivity is a physical property of material, defined as the ratio of IR energy radiated from the material surface and its nature (effectiveness). One of the greatest advances in physics was the blackbody or Planck equation. Planck's law states the spectral reflectivity (spectral radiant exitance) of a perfect blackbody as a function of temperature and wavelength of the emitted radiation, expressed in Equation (6) [132].

$$E(T) = \int_0^\infty E(\lambda, T)\, d\lambda = \sigma T^4, \tag{6}$$

where E is the radiant emittance $[\frac{w}{m^2}]$, σ is the Stefan-Boltzmann constant ($\sigma = 5.67x10^{-8}\,\frac{w}{m^2k^4}$), and T is the absolute temperature [K].

For any specific temperature, the blackbody gives the upper limit of a source's overall spectral exitance. Most thermal sources are not perfect blackbodies. These are typically referred to as graybodies. At the same temperature, a graybody emits radiation with the same spectral distribution as a blackbody, but at a lower intensity. Emissivity is defined in Equation (7) as the ratio of the real source exitance to the exitance of a blackbody at the same temperature. In principle, emissivity is affected by λ and T [132].

$$\varepsilon(\lambda, T) = \frac{E(\lambda_1 T)_s}{E(\lambda_1 T)_b}, \tag{7}$$

where $\varepsilon(\lambda, T)$ is the ratio of the exitance between de source $E(\lambda_1 T)_s$ and the blackbody $E(\lambda_1 T)_b$, which is dimensionless between [0-1]. In a perfect blackbody at any wavelengths, the emissivity is $\varepsilon = 1$. The emissivity of a graybody is influenced by the wavelength, as depicted in Figure 21. The image was taken from [119].

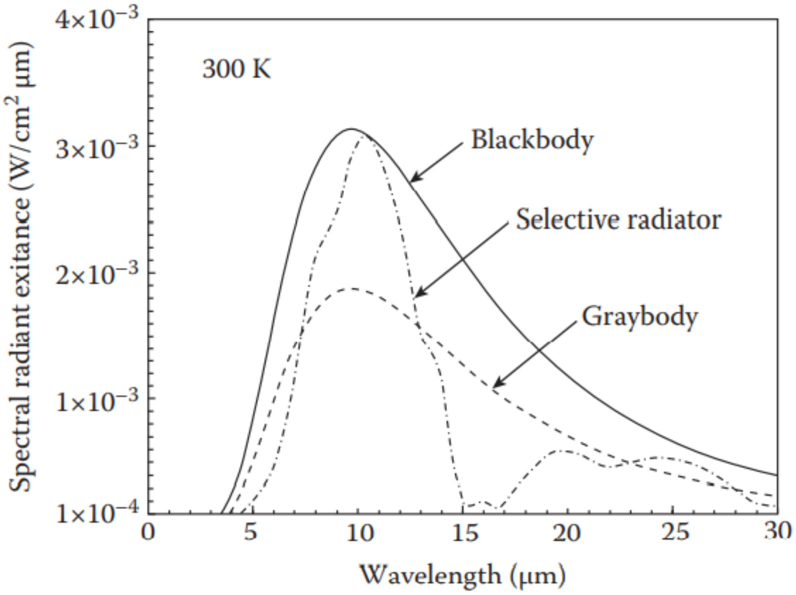

Figure 21: Spectral radiance exitance $\varepsilon(\lambda, T)$ for three different phantoms [119].

Blackbodies have a variety of mathematical principles that can be used to create physical models. The physical and theoretical models of blackbodies are not the same. As a result, a phantom or black body simulator is a technically accurate name for such a system [47,130]. Commercial blackbody simulators based on surface radiator principles are available on the market, commonly at high prices. Therefore, a practical approach is often practiced in studies such as using conical or plane radiators as an approximation to a black body (i.e. ε > 96%) [125].

2.1.8 Thermal Calibration

Temperature calibration is another important function. Several thermal imaging devices are made to detect temperature variations rather than to map the temperature that has been calibrated. A radiographic sensor is a camera that maps the actual surface temperature. Only mapping local temperature variations may be used to perform medical screening. This application would act as a third eye for the physician, assisting them in detecting asymmetries and temperature anomalies, such as hot or cold regions. Assessing circulation via thermal imaging, for example, entails searching for cold areas in a normally warm foot. If the physician decided to discuss the images with other physicians or use them for research, it should employ a calibrated camera so that the thermal differences can be quantified and separated from display settings and digital compression errors. When viewing the same image on two separate computer displays, for example, the results may change. If, on the other hand, the imaging is calibrated so that each color or brightness corresponds to a specific temperature, doctors can be confident that they are viewing relevant imagery and accurate temperatures rather than visual artifacts [45,91].

The calibration must be consistent and accurate enough to match the camera temperature accuracy. Caution is advised in this situation. Most radiometric sensors on the market are built for industrial applications where substantial temperature differences are expected and the temperature of the object is well over 100 °C; for example, at 600 °C, the temperature difference could be 5 °C. The temperature differences of interest in a diabetic foot are roughly a tenth of a degree at around 37ºc. As a result, the calibration procedure must be appropriate for those variables [45,65,133].

The calibration procedure is simplified since the dynamic range of the diabetic foot detection application is comparatively limited. The temporal stability, temperature resolution, and calibration accuracy are more critical. 0.1°C resolution at 37°C, 0.1°C stability per hour (drift), and 0.3°C precision are useful calibration parameters. This means that at body temperature, the camera can detect a temperature difference of 0.1°C with an accuracy of 0.3°C. For example, if the foot temperature is 36.5°C, the camera may register 36.7°C [134].

Internal and external calibration methods are available. External calibrating devices can be purchased from a variety of places. They may be traced back to the National Institute of Standards and Technology. External calibration has the disadvantage of requiring a black body and a more complicated technique for use. The thermal camera must be calibrated immediately before usage, and calibration imagery must be recorded, or the calibration source must be inserted in the image while data is being gathered [45]. Implementing a temperature-controlled system and instruments with measurement standards is one technique to perform an external calibration. The digital information collected by the sensor is compared with the standard instrument in this approach [47,125,135]. Internal calibration refers to the setting of parameters in the thermal chamber, such as ambient temperature, relative humidity, and emissivity [91]. For this thesis, Fluke Ti32 was employed which is possible to adjust the emissivity value. However, an external calibration was carried out based on a golden standard instrument (i.e. calibrated thermometer) to ensure precision. The calibration is detailed in Section 3.1.3.

2.1.9 Acquisition Protocols for Active and Passive Thermography

Several tests and patient preparation protocols must be properly followed to establish diagnostic-quality infrared images. The use of IRT requires a regulated environment. The nature of human physiology is the major explanation behind this. Thermal artifacts are caused by changes in the external (noncontrolled room) environment, clothes, and other factors. Sun exposure, cosmetics, lotions, antiperspirants, deodorants, exercise, and bathing should all be avoided before the test to adequately prepare the patient for imaging.

The temperature and humidity in the imaging room must be controlled and kept between 18 and 23℃, with no more than 1°C variation during the test. This temperature range guarantees that the patient is not placed in a setting that stresses their physiology and causes them to shiver or sweat. Drafts and infrared heat sources should also be avoided in the room (i.e., sunlight and incandescent lighting). To avoid increased physiologic stress, the floor should be carpeted, or the patient must wear shoes to maintain a physiologically neutral temperature environment [136].

Active or passive thermography refers to whether the patient is induced to a form of temperature stimulation, or the subject is homogenized with the ambient temperature. In medicine, active thermography, also known as Active Dynamic Thermal IR-imaging (ADT), is a suggested diagnostic modality. Descriptive images are mainly created by exploiting quantitative descriptors for evaluating subjects. The measurement technique requires the application of excitation, such as heating or cooling, to the object under test. An IR camera is used to record the thermal reaction of the object's surface to external excitation. Since the evaluated surface is usually obstructed by an IR camera during excitation, the phase of spontaneous recovery to initial conditions following excitation provides more accurate data for further analysis [95,137]. Figure 22 depicts the temperature variation of the torso when the subject is excited with external heating and cooling. The images were taken from [137,138].

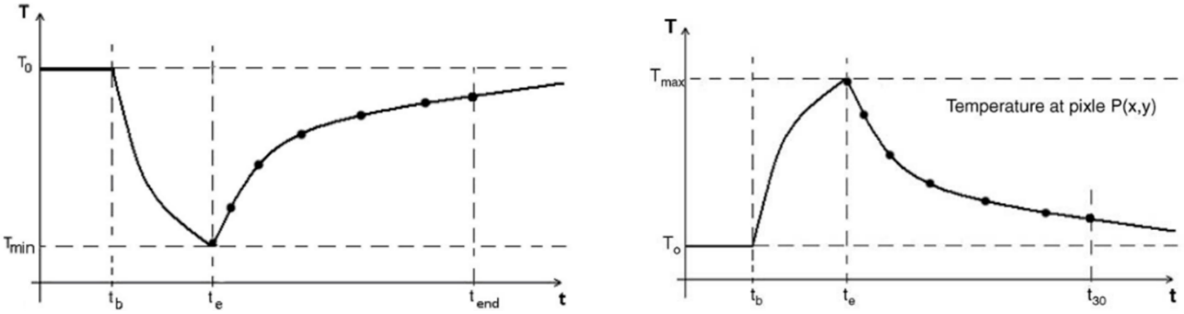

Figure 22: In 30 minutes, the heating and cooling sources are turned on (starting) and off (end) correspondingly [137,138].

The fundamental advantage in medicine is the ability to have a brief thermal interaction with a tested region since biofeedback mechanisms can be initiated and have a significant impact on measurement results. However, several practical difficulties limit the use of ADT in medical applications. The fundamental problem is that radiation energy distribution is difficult to manage, and optical excitation is frequently non-uniform. Furthermore, the temperature must not exceed 42°C; any higher temperature will damage vital cells and organs. The temperature along superficial tissue is decreasing due to heat exchange at the skin surface; hence boundary conditions are normally uncontrolled. In such circumstances, the temperature gradient after heating may be minimal, allowing heat exchange interpretation difficult. This leads to the conclusion that cooling is a better solution, even though it is technically more complex [30,91,139].

To achieve a condition in which the body is at thermal equilibrium with the environment, the patient must endure 15 minutes of waist-up undress acclimation for the passive thermography protocol, which is more appropriate in the study of vascular disease. Further variations in the body surface temperatures occur very slowly and uniformly, causing no alterations in homologous anatomic regions. At this moment, any thermal artifacts from clothing or the outside environment are also removed. In conclusion, following an adequate patient and laboratory protocols is critical for obtaining a physiologically neutral image that is free of artifacts and suitable for interpretation [45,136].

2.2 Image Segmentation

Clinical training and surgical planning, as well as medical imaging research, can benefit from anatomical models. Physical interaction with models in the clinic helps students learn anatomy and how different parts interact spatially in the body or offers a faster inspection of the physiological state of the patient instead of performing an inspection of a set of images that offer limited views. Medical image data, such as visible light and infrared images, can be used to create anatomically 3D models. Different features can be detected depending on the imaging modalities, therefore different picture segmentation techniques will be required.

Recent advancements in segmentation software have made it easier to extract, automatically or semi-automatically, the surface of structures of interest from medical imaging data. This has enabled the creation of anatomical models on a normal personal computer. At the same time, thanks to low-cost desktop alternatives, 3D printers, which were previously only available for industrial uses, are now available for household usage. This technology allows the rapid development of three-dimensional models without the requirement for traditional manufacturing experience [140].

The process of splitting an image into numerous labeled sections to locate objects and boundaries in images is known as image segmentation. It can be used to make very accurate computer models of organs and tissue that are patient specific. There are a variety of image segmentation approaches, each with its own set of benefits and drawbacks, but no single technique is ideal for all images and applications. Basic segmentation methods are based on the idea that the RoI would be cooler or warmer than the background (remarkable intensities). As a result, it is relatively simple to identify differences between boundaries. Image segmentation software is available in a variety of formats, ranging from multi-purpose commercial platforms to standalone physics simulations. However, in this section, digital image techniques principles for segmentation as well as radiometric processing advantages will be discussed.

2.2.1 Digital Image Processing Techniques

An image can be defined as a two-dimensional function $f(x,y)$, where x and y are spatial (plane) coordinates. The amplitude of f at any pair of coordinates (x, y) is called the intensity or gray level of the image at that place [141]. When (x, y), and the intensity values of f are all finite, discrete quantities, we call the image a digital image. The field of digital image processing refers to processing digital images employing a digital computer.

Image segmentation refers to the separation of an image into its constituent regions or objects. The level of subdivision that is carried out depends on the problem that is being handled. In other words, segmentation would be considered completed when the objects or regions of interest have been identified (i.e. separated from the background) [142]. In medical imaging, for example, studies are interested in evaluating the presence or absence of temperature anomalies in specific regions of the body.

One of the most challenging problems in image processing is the segmentation of nontrivial images. The success or failure of automated analytic methods is determined by segmentation accuracy. As a result, great effort should be made to improve the chances of proper segmentation. In some cases, such as medical applications, at least some level of environmental control is usually possible to enhance or assist the segmentation process [74,134]. Most of the segmentation algorithms described in this chapter are based on the fundamental features of intensity values: discontinuity or similarity. The first method divides an image into sections based on abrupt changes in intensity, such as edges. The main methods in the second category are based on segmenting an image into similar parts based on a set of specified criteria. Methods in this category include thresholding, which also was applied for segment regions with radiometric data.

In general, a region is considered when the following conditions are satisfied (Equations 8-12). Considering R as a space region of an entire image, image segmentation is defined as a process that partitions R into n sub-images $R_1, R_2, R_3 \dots R_n$ [141]:

$$\bigcup_{i=1}^{n} R_i = R \tag{8}$$

Ri is a connected set, $i = 1,2,3 \ldots n$ (9)

$R_i \cap R_j = \emptyset$ for all i and j, i≠j (10)

$Q(R_i) =$ TRUE for i = 1,2,3, … n (11)

$Q\left(R_i \cup R_j\right) =$ FALSE for any adjacent region Ri and Rj (12)

where $Q(R_i)$ is a logical operation over each pixel in the region R_i and $\emptyset$ is null space. Figure 23 illustrates a segmented false-color image where two independent regions of the scene can be seen.

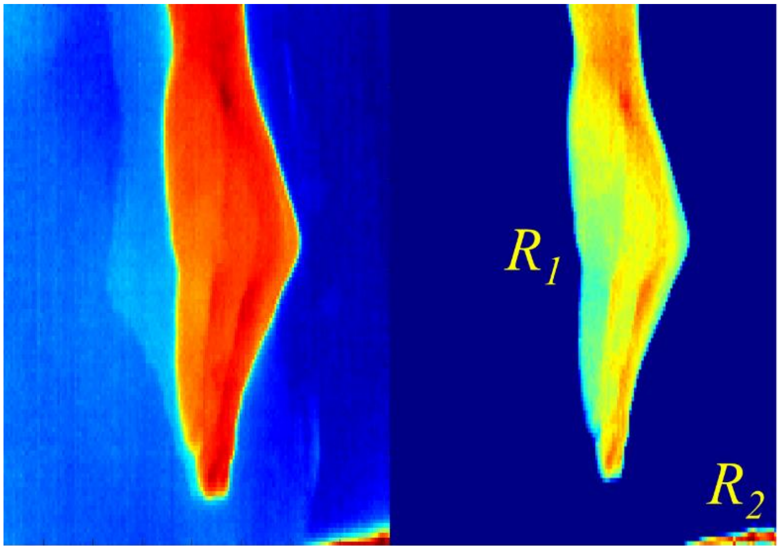

a) b)

Figure 23: a) original thermal image reconstructed from radiometric information, b) image segmented into two independent regions. It is important to note that the region R2 is considered an interference since it does not belong to the RoI, i.e., only R1 should exist in the space R.

According to Equation (7), the segmentation must be complete, meaning that every pixel must be in a region. Equation (8) specifies that points in a region must be connected in some way (e.g., the points must be 4- or 8-connected). The regions must be disjoint, according to Equation (9). Equation (10) deals with the properties that pixels in a segmented region must satisfy, e.g. if all pixels in the region have the same intensity level. Finally, Equation (11) indicates that two adjacent regions must be distinct.

In general, segmentation methods for binarized images are based on one of two main types of intensity value properties: discontinuity or similarity. The assumption in the first category is that area boundaries are sufficiently distinct from one another and from the background to allow boundary detection based on local intensity discontinuities. The most common method in this category is edge-based segmentation. In the second category, region-based segmentation methods divide a picture into regions that are comparable based on a set of specified criteria.

The edge description of an image minimizes the amount of data that must be processed while preserving valuable information about the shape of objects in the picture. This visual explanation is simple to implement in a variety of object identification algorithms used in computer vision and other image processing applications. The capacity to extract the exact edge line with good orientation is a key feature of the edge detection technique. On the other hand, no common performance directory for evaluating the performance of edge detection algorithms if the Canny criteria exist. The effectiveness of edge detection algorithms is always appraised on a specific instance basis, depending on the application. Local variations in visual intensity are referred to as edges. Edges are often seen at the intersection of two regions. The main features of an image can be retrieved from the edges. For image analysis, edge detection is a crucial feature. Advanced computer vision algorithms make use of these characteristics. Computer vision using edge detection is utilized in a variety of applications such as medical image processing, biometrics, etc. Roberts edge detection, Sobel edge detection, LoG edge detection, and Canny edge detection are the most often utilized discontinuity-based edge detection approaches [142–144].

Roberts edge detection computes a spatial gradient value on an image. This approach highlights spatial frequency regions, which commonly correspond to edges. The most popular application of this method is to give the operator a grayscale image that matches the output. Every pixel value in the output represents the estimated entire magnitude of the input image spatial gradient at that place. The Roberts operator is given by:

$$\begin{bmatrix} -1 & 0 \\ - & +1 \end{bmatrix}_X \qquad\qquad \begin{bmatrix} 0 & -1 \\ +1 & 0 \end{bmatrix}_Y$$

The Sobel method of image segmentation edge detection uses a linear regression approximation to the derivative to detect edges. A possible edge is related to a pixel that contains the highest gradient concerning its neighbors. The Sobel approach emphasizes regions of high spatial frequency that correlate to edges by performing a spatial gradient quantity on an image and it is typically used to calculate the estimated absolute gradient magnitude at each location in a grayscale image. At the very least, the operator is given by:

$$\begin{bmatrix} -1 & -2 & -1 \\ 0 & 0 & 0 \\ +1 & +2 & +1 \end{bmatrix}_X \qquad \begin{bmatrix} -1 & 0 & -1 \\ -2 & 0 & +2 \\ -1 & 0 & +1 \end{bmatrix}_Y$$

The Laplacian of Gaussian (LoG) of an image defined by *f(x,y)* is a second-order derivative defined by Equation (13).

$$\nabla^2 f = \frac{\partial^2 f}{\partial x^2} + \frac{\partial^2 f}{\partial y^2} \tag{13}$$

The LoG will smooth the image and compute the Laplacian, resulting in a double-edged image. Finding the zero crossings between the double edges is the next step in locating edges. The Laplacian is commonly used to determine whether a pixel is on the bright or dark side of an edge. The LoG operator is given by:

$$\begin{bmatrix} 0 & -1 & 0 \\ -1 & 4 & -1 \\ 0 & -1 & 0 \end{bmatrix}_X \qquad \begin{bmatrix} -1 & -1 & -1 \\ -1 & 8 & -1 \\ -1 & -1 & -1 \end{bmatrix}_Y$$

One of the standard edge detection approaches is the Canny edge detection technique. Canny is a highly essential method for finding edges by isolating noise from the image before finding image edges. The Canny approach is a better method since it preserves the features of the image edges after applying the tendency to detect the edges and a substantial threshold setting. The Canny algorithm is depicted in Figure 24. The Canny operation, unlike Roberts and Sobel, is not very sensitive to noise. It would be superior if the Canny detector worked properly.

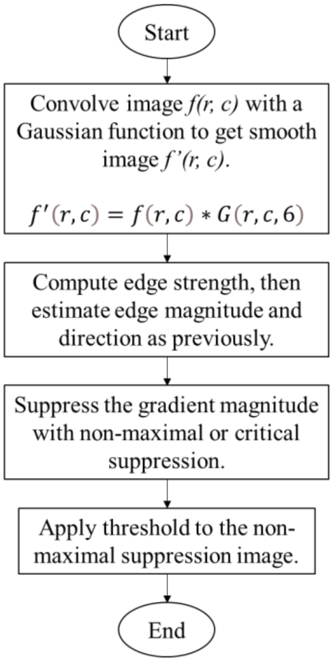

Figure 24: Canny edge detector algorithm [143].

Figure 25 illustrates the comparison between the methods described above.

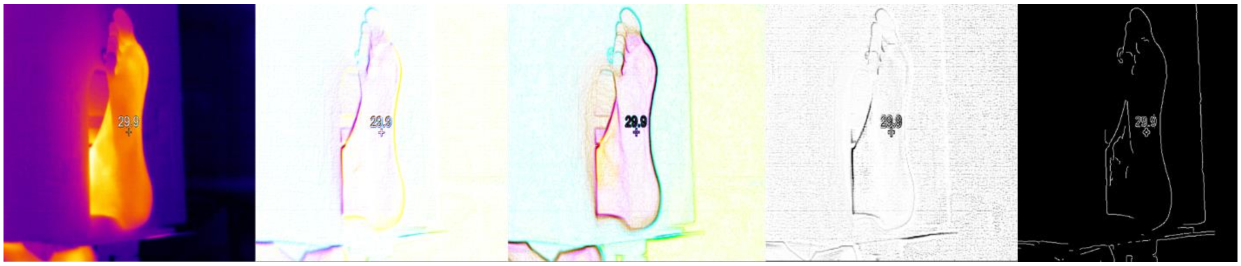

a) b) c) d) e)

Figure 25: a) thermal image taken from volunteer 1 presented in this thesis, b) Robert edge detector, c) Sobel edge detector, d) LoG edge detector, e) Canny edge detector.

As seen in Figure 25, the edge detection approach is ineffective in thermal imaging because it is unable to isolate the foot from the scene. The image used for the test presented in Figure 25 a), is an image sample of the foot taken with the thermal camera Ti32. The thermal image was extracted directly from the camera without any digital processing in JPEG format, so this sample was input into the several edge detectors presented above. Canny method presented the best results with the following parameters: σ = 2, Low threshold = 0.8, High threshold = 0.11 and signal no noise ratio = 0.0039. However, the borders of the foot are not a closed contour and the borders of some objects in the scene remain. The latter method would be suitable if only the borders of the foot would be obtained, in such a way that they may exploit as a mask to segment the original image.

The region-based segmentation approach compares nearby pixels for similarity. Pixels with comparable properties are clustered together into distinct regions. Gray-level intensity is the most common method of attributing similarity in all segmentation approaches, however additional options exist, such as variance, color, and multispectral characteristics. The pixels that indicate homogeneous areas in an image are clustered using region-growing algorithms. Regions are formed by grouping neighboring pixels with qualities that differ by less than a certain amount, such as intensity. In the output image, each grown region is given its numeric label. Because it is adaptive and less vulnerable to the effects of partial occlusion, adjacency, noise, and ambiguous borders, this family of algorithms works well with difficult imagery. These can be divided into two categories [141,145]:

- Merging algorithms analyze neighboring regions and combine them if they are similar enough in some way.
- Splitting Algorithms, which divide huge non-uniform regions into smaller, possibly uniform portions.

Merging must begin with a seed region that is uniform. An appropriate seed region has been identified after some research. Divide the image into 2x2 or 4x4 blocks and verify each one separately. Another option is to cut the image into strips and then further subdivide the strips. The seed will be a single pixel in the worst-case scenario. Once a seed is discovered, its neighbors are merged until no more neighboring regions meet the uniformity condition. The region is removed from the image at this stage, and a new seed is used to merge another region. By combining adjacent areas that belong to the same object, region merging techniques eliminate erroneous boundaries and spurious regions. A partition satisfying condition is the starting point for merging schemes (e.g., regions produced using thresholding): $Q(R_i) = TRUE$. Then, by gradually merging adjacent image portions, they proceed to fulfill the criterion $Q\left(R_i \cup R_j\right) = FALSE$ [141,145].

Splitting algorithms start with the entire image and partition it into subregions until each one is uniform. When the attributes of a newly split pair do not differ from those of the original region by more than a threshold, the splitting procedure is usually stopped. The difficulty in selecting where to make the partition is the main issue with this type of technique. Early algorithms employed some regular decomposition methods, which are adequate for specific classes; nonetheless, splitting is usually used as the initial stage of a split/merge process.

Algorithms that combine splitting and merging are available. In every scenario, a uniformity criterion must be used to determine whether a region should be split or two regions should be combined. This criterion is based on an area property defined by the application, which might be any of several measurable image qualities such as mean intensity, color, and so on. Setting boundaries on the measured attribute or utilizing statistical metrics like standard deviation or variance can be used to determine uniformity criteria [145]. Figure 26 presents a scheme of how splitting and merging ideas, the illustration was taken from [146].

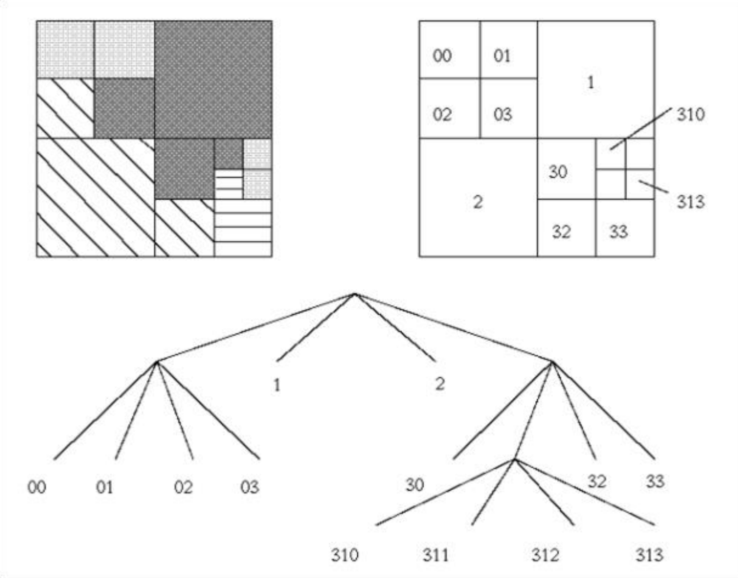

Figure 26: Splitting and Merging Algorithm [146].

This method consists of defining a pyramid statistics shape, a homogeneity criterion, and a preliminary segmentation into areas. Split each non-homogeneous vicinity *R* inside the pyramid statistics shape into 4 child areas (Region QuadTree); if any 4 areas with the equal determine may be mixed right into an unmarried homogeneous vicinity, they are a candidate for merging. If the regions cannot separate or merge any, the last step must be “iterated”. Then, the detected neighboring regions must be merged; *Ri, and Rj*, may be merged into a homogenous vicinity (even though they may be on extraordinary pyramid stages or do not have the equal determine). If it is required to delete minor areas, merge them with the maximum comparable close by vicinity [145].

Figure 27 compares the result between an original thermal image and the result of the splitting-merging method provided by [147].

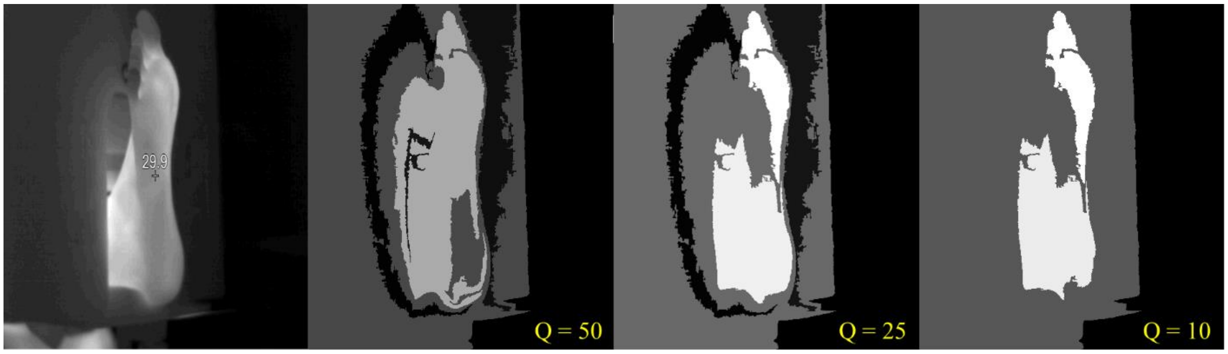

a) b) c) d)

Figure 27: a) Original thermal images are taken from volunteer 1, b), c) and d) are segmented digital images (8-bit grayscale) based on the splitting merging method with several regions Q = 50, 25, and 10 respectively. All regions were detected by 8 connectivity.

As Figure 27 d) illustrates, even choosing a $Q = 10$, the foot that corresponds to the RoI is not segmented correctly. Any Q below 10 will eliminate the RoI. For this reason, the splitting and merging method may not be suitable for our purpose due to the number of elements of the scene.

A third method is the image binarization based on thresholding which occupies a crucial place in image segmentation applications due to its intuitive features, ease of implementation, and computational speed. Selecting a threshold T that divides these modes is one way to remove the objects from the backdrop. The intensity of $f(x,y)$ is specified by T which is a number between [0-1]. Any point in the image that is an object point is referred to as such; otherwise, the point is referred to as a backdrop point. Equation (14), in other words, gives the segmented image [142].

$$g(x,y) = \begin{cases} 1, & if\ f(x,y) > T \\ 0, & if\ f(x,y) \leq T \end{cases} \tag{14}$$

The procedure described Equation (14) is known as global thresholding when T is a constant that applies to the entire image. Variable thresholding is the term used when the value of T changes over time in a picture. Variable thresholding is frequently referred to as local or regional thresholding, in which the value of every place in a picture is determined by the attributes of a neighborhood of pixels (for example, the average intensity of the pixels in the neighborhood).

Although the principle of this method was used in segmentation from radiometric information, it has a limitation when dealing with thermal images. The comparison will be technically detailed in Section 2.2.4. Figure 28 shows the results of segmenting by thresholding at 70% with Otsu's automatic method [148].

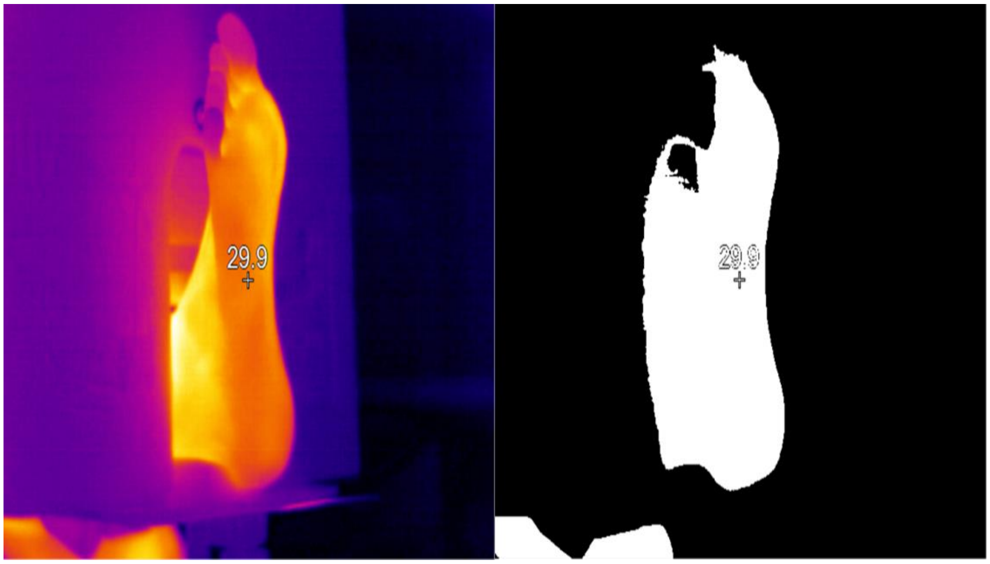

a) b)

Figure 28: a) thermal RGB image of volunteer 1, b) binarized images with a $T = 0.7$. It is noticed also that two different regions were segmented due to similarity between temperature intensities.

2.2.2 Machine Learning Approach

Artificial Neural Networks (ANNs) are a method exploited for pattern recognition, including medical segmentation, which is a major part of Computer Vision and Machine Learning. This is due to ANNs' ability to learn, adapt to changing settings, and display a computing paradigm similar to that of the human brain's parallelism [149]. As a result, ANNs are capable of solving a wide range of pattern identification and prediction issues. ANNs work in two phases: training and testing. Training is when the ANN learns the patterns, and testing is when it determines how much it has learned. There is no standard approach that can be used for all types of images with success. Furthermore, selecting the most appropriate segmentation method is a complex task. Characteristic histogram thresholding, edge/boundary detection, region extraction or region expansion, and semantic and syntactic techniques are examples of traditional algorithms. Artificial intelligence methods, particularly neural network approaches, are used to apply segmentation algorithms. Sometimes one type of image may not apply to all images or may be applied with poor results [75,150,151].

For segmentation, supervised techniques require human input. Typically, this means that human experts select the training data, which is subsequently utilized to segment the images. Unsupervised methods or clustering processes might be semi-automated or completely automated. To increase the effectiveness of the approaches, user participation may be required at some point during the process, but the computing should be independent. Without the need for manual involvement, an unsupervised segmentation algorithm automatically separates the images based on a database previously selected. These designs, on the other hand, might be built at design time utilizing application-specific a priori knowledge, such as anatomical, physical, or biological knowledge [45,134,152,153]. Along with the development of this work, we collaborated in the field of segmentation based on Machine Learning. The results based on the work of Maldonado et al. [75] are presented in Figure 29. The limitation of this work was the need to have a database that would train the neural network for segmentation; however, this was only successful in images in the visible spectrum. Currently, segmentation of thermal images with ANN requires prior training, which involves manual segmentation by an expert. The limitations will be discussed in the next section.

Figure 29: Segmentation con R-CNN and the generated masks in visible spectrum images. The database for training is a set of 300 images [75].

2.2.3 Manual Segmentation on Thermal Images

Manual segmentation by an expert in the subject is a popular solution in thermal image segmentation. Table 7 compiles the most recent work on medical IRT that included a manual segmentation.

Table 7: List of studies involving medical IRT. Although selected papers involve classification and pattern detection with a diagnostic perspective, RoI segmentation has been a manual task implemented by a specialist.

Author	Year	Application
González-Pérez et al [108]	2021	Diabetic foot análisis
Queiroz Júnior et al [64]	2020	Breast cancer detection
Vardasca et al [154]	2019	Diabetic foot análisis
Magalhães et al [155]	2018	Skin Neoplasms classification

When samples are obtained in controlled conditions, segmentation in thermal imaging is usually not a problem. However, some initiatives, such as the work of Maldonado et al. [75], are attempting to address this difficulty by implementing Machine Learning. Multimodal image registration or pathology detection is the focus of process automation. The segmentation of the RoI in a thermal image is critical in studies where samples are affected by thermal interferences or in semi-controlled conditions.

The main downside of this manual segmentation is how time-consuming it can be when dealing with a series of images (videos) when the interference is naturally different between two frames. As a result, to automate this procedure, it is proposed in this thesis to process radiometric data rather than an image when the LWIR sensor can produce this type of data. The concepts of radiometric information are discussed in the next section; however, the processing is covered in detail in Chapter 3.

2.2.4 Radiometric Data Processing Advantages

It is critical to acquire calibrated data, also known as "raw" data or radiometric data, for medical studies in which data must be saved, distributed, and used for the testing of software and medical observations, or to investigate temperature patterns. Thus, a radiometric still camera with uncompressed standard formats or "raw" output that keeps the thermal calibration is preferable use [45]. Nevertheless, the IR images were segmented automatically (which is where this project's contribution resides) using IR radiometry data processing.

Due to the lack of features that may distinguish the target from the image background, automatic segmentation of false-color images, such as thermographic images, remains a challenge. Instead of using the image as input data, this problem can be solved by using radiometric data directly from the sensor [156]. Only the region of interest will contain the color map corresponding to the IR energy intensity recorded by the sensors if the segmented information is fitted to an image in the visible spectrum. Although the accuracy of segmentation based on radiometric information has yet to be documented, there have also been advances in multimodal picture registration using manual segmentation [108]. Multimodal segmentation addresses the challenge of point cloud estimation by adding more visible-spectrum features to a scene, making multimodal fusion useful for these purposes [157]. In this way, instead of processing a false-color image for a specific segmentation procedure, it is feasible to automatically segment a region with search criteria for a given temperature range in a one-dimensional array. This approach can detect the region of interest, reduce thermal interferences, and improve the contrast in the RoI. In essence, the method was created to generate merged images with just the RoI containing false colors corresponding to the measured temperature.

A radiometric thermal camera translates the intensity of an IR signal that is captured by the sensor to estimate the temperature of a surface. When a camera has radiometric capabilities, it allows the user to save images for post-study image analysis and properly estimate the temperatures of individual image pixels. Temperature data can be recorded in every pixel of an image when radiometric imaging is used. As a result, a physician or specialist can analyze and provide accurate reports and images that examine temperature data across the image, achieving quantitative results [158,159].

Some of the advantages of advanced radiometric cameras, according to [111,159,160], include the following, which were also used in this thesis:

- Increased accuracy by 5% in the high-gain condition, with small variations over the whole working temperature range.
- Users can choose any point on the array for their coordinates. In this way, the data arrays may be treated in a similar way to an image.
- Additional spot-meter data is available in real-time, including average, standard deviation, minimum, and maximum values.
- Digital data in scene temperature is linear, the pixel values in the digital data correlate to the scene temperature.

- Temperature data in detail (users derive temperature information per pixel from objects in the scene)
- Temperature precision enables emissivity compensation of external scene characteristics.

Some cameras with advanced radiometric technology can even compensate for temperature fluctuations. This enables users to receive a result that has been stabilized and normalized, actual results in "temperature-stable video," which means that a scene with a given temperature will always correlate up to a specific digital value in the video, regardless of the camera temperature, as in the case of the Fluke Ti32 model. Because of the low cost (and portability) of modern radiometric thermal cameras, practically any laboratory may make use of the benefits and advantages that this extremely valuable technology offers. The use of radiometric thermal cameras has already helped several medical applications [57,77,134,161]. Radiometric thermal technology may increase even more applications in the next years as its cost-effectiveness and feature set improve. Figure 30 illustrates the comparison between a segmented image with radiometric data processing and a thermal image directly extracted from the thermal camera. Although Figure 32 a) is not perfectly segmented, it is possible to observe that certain thermal interferences were eliminated and that the RoI of the foot contrast correction. Radiometric data processing allows to segment automatically based on threshold criteria applying a range normalization between [0-1]. For this case, the threshold was set to 0.8 which presented the best results. Any value below 0.8 may carry thermal artifacts, while any value above 0.8 will erode the RoI (foot).

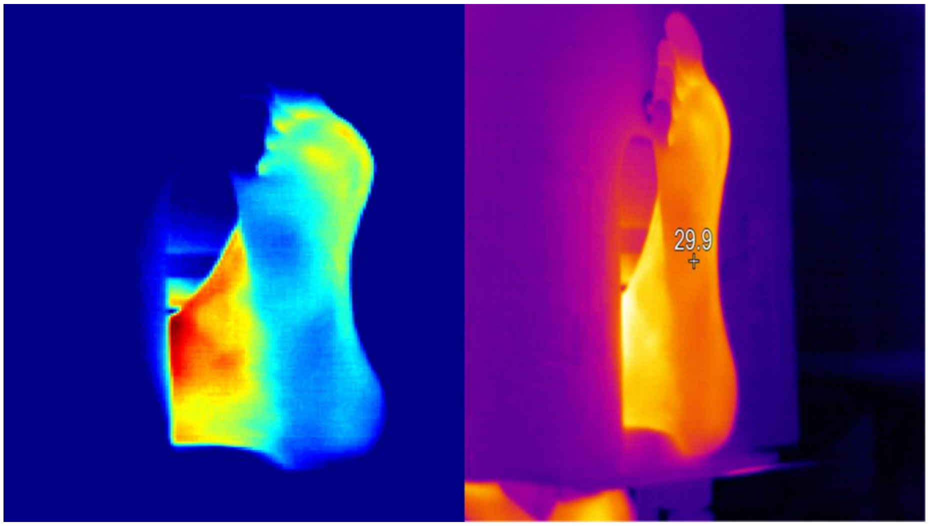

a) b)

Figure 30: a) Image segmented and reconstructed from radiometric information, b) original thermal image extracted from the thermal camera.

2.3 Multimodal Image Registration

The process of translating multiple images of the same scene into the same coordinate system is known as image registration. These images may be captured at various time intervals, using multi-modal registration (multiple types of sensors), and from different perspectives. These images' spatial connections might be rigid (translations and rotations), affine (shears, for example), homographies, or complex deformation models. Image registration is useful in several situations, but it is most useful when comparing many images of the same scene. It is indeed widely used in medical imaging, as well as satellite image processing and optical flow analysis [142]. The fundamental reason for employing registration between false-color and visible light images was to enhance the keypoint detection and matching process. During testing, it was found that using only a collection of false-color images led to no detection of key points or, at best, mismatching due to the colors mapped (Jet palette) onto the image. The rigid registration is the only connection that competes with this thesis since the thermal images and visible spectrum images were simply transferred and rescaled. The transformation was required since both sensors have different resolutions and FOV; however, since both sensors were placed at the same distance, the rigid registration was enough to complete the task. The superimposed images were compared to the picture-in-picture tool assistant provided by Fluke, leading to the same result.

2.3.1 Methods

This section presents several methods for multimodal image registration (thermal and visible light images). Although a simple scaling and translation operation was required for our purpose, this section may be fundamental to explore as a perspective in such a way as to improve the scalability of the proposed method in this thesis.

The Geometric Optical Translation technique employs a mathematical method to acquire image registration from visible and infrared cameras. A scaling process (resizing images) was employed to match the angular resolution of each sensor image. Using a translation transformation provided by Equation (15), the visible pictures were translated to fit the coordinate system of the IR camera [145].

$$T(p) = p + \vec{u} \tag{15}$$

The translation transformation *T(p)* of a point p is given by a vector $\vec{u}$ in which will move the point p into a new point $p \rightarrow \vec{p}$. Finally, a cropping procedure was included to match the coordinate system and the resolution of the thermal and visible spectrum images.

The second registration technique, which is described by the Homography transformation, provides the most flexibility by depending on a transformation with the freest parameters described in Equation (16).

$$T_\mu(x) = H(x) \tag{16}$$

$$H = \begin{bmatrix} h_{00} & h_{01} & h_{02} \\ h_{10} & h_{11} & h_{12} \\ h_{20} & h_{21} & h_{22} \end{bmatrix}$$

The image may be translated, rotated, scaled, sheared, and perspective adjusted using the homography matrix H. The key points are detected by overlaying the images with a standard blob feature detector and then matching the set of key points in one image with the corresponding counterpart in the other image [145]. The homography matrix was employed in the point cloud estimation that will be detailed in section 2.4. For determining the optimal collection of key points that map one image to the other and removing outliers that do not support the transformation, a Random Sample Consensus (RANSAC) [162] statistical outlier removal technique is used to determine the set of parameter values that fulfill a homography transformation.

The Iterative Closest Point technique aligns two sets of arbitrary points iteratively. Equation (17) defines a rigid transform T_μ.

$$T_\mu(x) = R(x - c) + t + c, \tag{17}$$

where R is the rotation matrix (i.e. orthonormal and proper), c is the center of rotation, t is the translation applied, and the parameter vector is specified by $\mu = t$. The image that is being transformed is treated as a rigid body, and the algorithm will translate and rotate it without allowing for scale changes throughout the registration process. A set scaling ratio handles any change in scale between the two pictures. Euler angles are used to parameterize the rotation matrix. The image rotational center has been set to the image center [108,145].

The last registration method is the Affine Transformation with Gradient Descent, which relies on a transformation with more free parameters than the Iterative approach and provides more flexibility than the Iterative method. It is defined as an affine transformation stated as Equation (18):

$$T_{\mu}(x) = A(x - c) + t + c \qquad (18)$$

The transformation matrix A has no restriction, therefore the image can be translated, rotated, scaled, and sheared to generate these extra degrees of freedom.

2.3.2 Applications

The advancement of technology in recent decades has increased the quantity, diversity, and complexity of data collected by image sensors [45]. There are a variety of 2D and 3D datasets including multimodal samples collected using several sensors. 3D data can come in different properties, as well as distinct sources of inaccuracy. The use of such data frequently requires appropriate alignment in a shared coordinate system. Before viewing, comparing, or processing data, alignment, or registration, has become a fundamental task in computer vision and computer graphics, and a variety of applications require alignment algorithms. Multiple procedures, such as 3D object retrieval, 3D mapping, 3D object scanning, and 3D model reconstruction, use registration techniques, which are essential components of applications like cultural heritage and medical imaging [45,163].

The availability of methods for objective and quantitative evaluation of images across different settings or patients is an important consideration when processing medical thermal imaging data. Multimodal applications are becoming increasingly popular as sensor designs improve, and image sensor costs drop. Imaging sensors include infrared (IR) and visible (visible) cameras. Multimodal imaging provides anatomical (visible spectrum picture) and physiological inspections (thermal imaging). For future fusion and processing, registration between IR and visible pictures is necessary. Detecting and matching similar features in image sequences taken by two separate sensors is challenging. Current IR and visible registration approaches may be categorized based on the characteristics used [164]. Although in this thesis a series of consecutive images were taken, the multimodal registration was addressed as a set of static images.

The range of modalities that must be aligned is extensive. For anatomical modeling, the 3D point cloud and 3D mesh are the most popular applications. A frequent modality is the 2.5 D RGB-D picture (i.e. a 2D color image with depth); such images are sometimes referred to as 2.5 D since they are an image with depth information per point. Medical imaging applications give rise to a wide range of modalities. Ultrasound, X-ray, magnetic resonance imaging, and computed tomography are examples of anatomical imaging that reveal the anatomy of entire regions. Thermal imaging and positron emission tomography are examples of functional pictures that depict the physiological activity of specific body locations [36,121,163]. Table 8 provides a few studies involving 3D modeling with multimodal registration.

Table 8: Overview of the 3D reconstruction techniques based on visible-light images and/or IR images. Although the acquisition techniques are different, the objective is common for all the reported papers for a 3D structure estimation.

Author	**Year**	**Method**	**Optical Technique**	**Data/Image Processing**	**Application**
Souza et al. [98]	2015	Structured light	Active	Particle Swarm Optimization	General purposes
Chernov et al. [85]	2017	Stereoscopy	Active	Correlation between depth and IR images	Breast reconstruction
van Doremalen et al. [33]	2019	Stereoscopy	Passive	Projective Transformation	Diabetic Foot study
de Queiroz Júnior and de Lima [64]	2020	Stereoscopy	Passive	Manual tracing of the profile curve	Breast pathologies study
Bayareh et al. [34]	2021	Stereoscopy	Passive	IR radiometric processing for multimodal fusion	Diabetic foot study

When both visible and infrared spectrums are employed simultaneously, a consistent and effective registration approach between visible and thermal infrared pictures is required to generate a multispectral image for abnormal plantar temperature detection. Other steps of the analysis might begin when the registration procedure has been completed successfully. These processes may involve segmenting the feet to identify temperature differences by thermal image comparisons, multimodal mapping between temperature changes and visible anatomical changes, and dataset generation of multispectral images. The next section reviews the performance of four different registration methods for fusing visible and thermal infrared images captured using low-cost cameras for medical applications

2.3.3 Performance

In 2021, González-Pérez et al. [108]. published a report on the accuracy of the image registration algorithms discussed in Section 2.2.1. This work is significant to this thesis because it may be used to test the report concept, which is intended to use radiometric information processing to automate segmentation. It is worth noting that, while image fusion was carried out automatically, the segmentation of thermal images was carried out by a professional, according to the authors. As a result, the cited study may be relevant to this thesis in terms of evaluating the accuracy of segmentation using radiometric data and multimodal fusion. Figure 31 shows the fusion of thermal images and registered visual masks acquired using different registration methods when the patient's feet are at the focus plane distance.

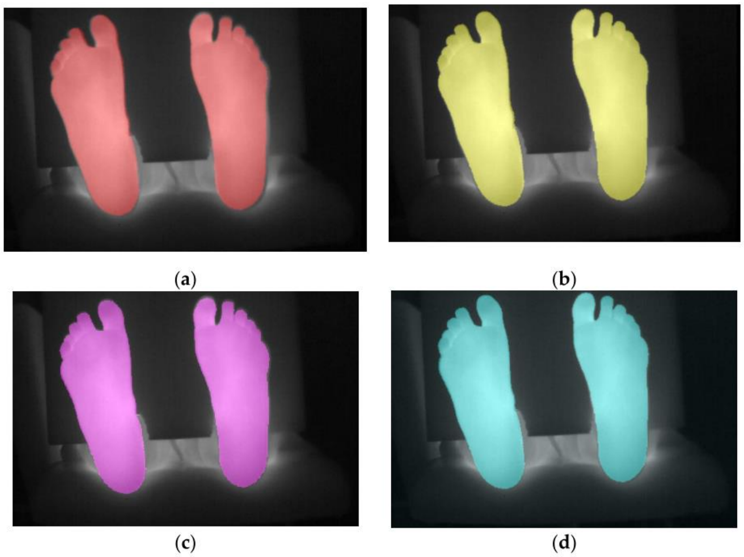

Figure 31: After using each registration approach (masks marked in color), a fusion of thermal IR pictures with foot segmentation of the visible image was assessed at 800 mm. The techniques of registration are: (a) Geometric Optical Translation (GOT), (b) Homography, (c) Iterative Closest Point, and (d) Affine Transformation with Gradient Descent. The images were taken from [108].

Figure 32 presents the similarity between the registration methods presented previously, based on Dace and Jaccard coefficients. The Dice coefficient is a statistical method used to compare the similarity of two samples, which coefficient varies from 0 to 1 (see Equation (19)) [165]. In computer vision, the Dice and Jaccard similarity coefficients are often employed to support the similarity (e.g. image registration).

$$Q_{SD}(A,B) = \frac{2|A \cap B|}{|A| + |B|} \tag{19}$$

where $Q_{SD}(A,B)$ is the Dice coefficient [0 – 1], A and B are the cardinalities of two sets (number of elements of each image).

On the other hand, The Jaccard coefficient, which is defined as the size of the intersection divided by the size of the union of the sample sets, is a measure of similarity between finite sample sets (see Equation (19)) [166].

$$J(X,Y) = \frac{|X \cap Y|}{|X| + |Y| - |X \cap Y|} \tag{20}$$

where $J(X,Y)$ is the Jaccard index [0 – 1], X and Y are the cardinalities of both sets.

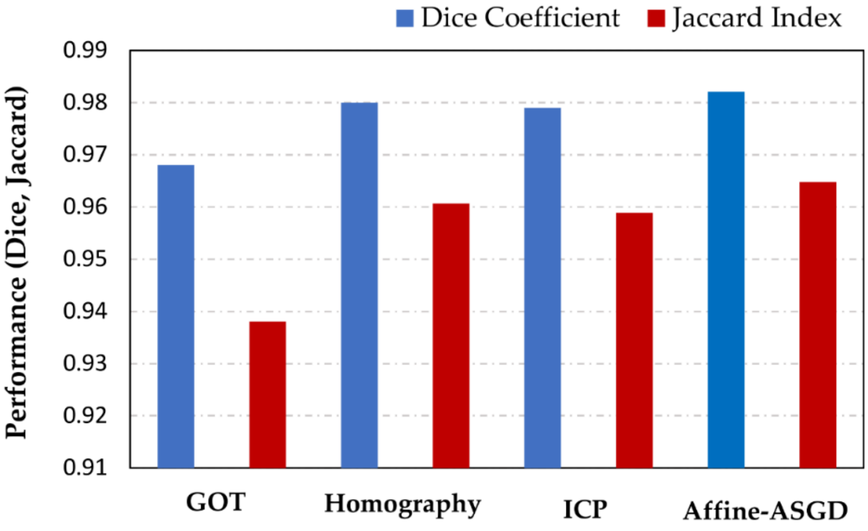

Figure 32: The four registration techniques Dice coefficient and Jaccard index metrics. These results were taken from [108] as a perspective that follows this thesis.

2.4 3D Reconstruction

The process of recreating a shape or structure from a set of images is defined as 3D reconstruction. A 3D model could provide physicians and researchers a more accurate picture of the surface temperature distribution and assist in its interpretation using 3D thermography systems that blend 3D geometric data with 2D thermography data. This provides a deeper understanding of the heat flow distribution and thermal processes in the area under the surface. In medicine, IRT has been presented as a possible alternative to computed tomography angiography for preoperative vascular mapping in breast reconstruction, as well as for breast cancer diagnosis, skin burn diagnostics, skin cancer detection, and the main focus of this thesis: diabetic foot studies [87,97,167,168].

This section briefly describes the basics of 3D surface reconstruction based on the principles of Structure from Motion. The following list presents a short description to introduce the concepts used in the following sections of this thesis. In resume, the surface reconstruction was carried out as follows:

1 Image pre-processing: false-color images are retrieved after segmenting the foot based on thresholding criteria. The RoI is mounted into the visible-light images by scaling and translation. The output of this step is a set of merged images of both modalities (i.e., IR and visible light).

2 SfM: The merged images were converted into the gray level domain by modeling a weighted addition of the R, G, and B components. Then, the sparse 3D point cloud and the camera parameters (i.e., position and orientation) were retrieved in this step. The point cloud is obtained by a cluster of homologous 2D points from the projection of the same point on different viewpoints, which are used for the estimation of the point cloud and camera poses [169].

3 Dense reconstruction: at this stage, a dense point cloud is generated based on the camera poses and the cluster of matched key points obtained from the last step. The surface estimation is based on Poisson surface reconstruction [170].

4 Mesh generation: an estimated surface is obtained by triangular facets from the dense cloud, based on the mesh-generation algorithm [171].

5 Surface texturing: a sharp and accurate color texture of the images is superimposed on the mesh surface [171].

2.4.1 Structure from Motion (SfM)

Structure from Motion is a technique used in the domains of computer vision and visual perception to describe the process of determining the 3D structure of an object by studying local motion signals across time. From the motion cue, SfM creates a 3D model. Assuming that all the objects in the scene are stationary, their relative displacement is only determined by their depth. This method creates a model from a collection of images or a video. SfM systems, more precisely, take a set of images as input and build a 3D point cloud of the scene, as well as the position from where each image was taken and the cameras' optical characteristics [169,172].

A typical SfM pipeline consists of several processing phases, each of which addresses a distinct reconstruction difficulty. Each stage might use multiple methods to handle the problem at hand, resulting in a large number of distinct SfM pipelines. The SfM pipeline allows 3D structures to be reconstructed from a sequence of images gathered from multiple observation views. Figure 33 depicts the incremental SfM pipeline steps. Incremental SfM, in particular, is a pipeline that consists of a first phase of image correspondences search and the second phase of iterative incremental reconstruction. Feature Extraction, Feature Matching, and Geometric Verification are the three processes in the correspondence search phase. The generated scene graph is used to initialize the model with a chosen two-view reconstruction before progressively registering additional images, triangulating scene points, filtering outliers, and improving the reconstruction by employing bundle adjustment [169,173]. Figure 33 was taken from [173].

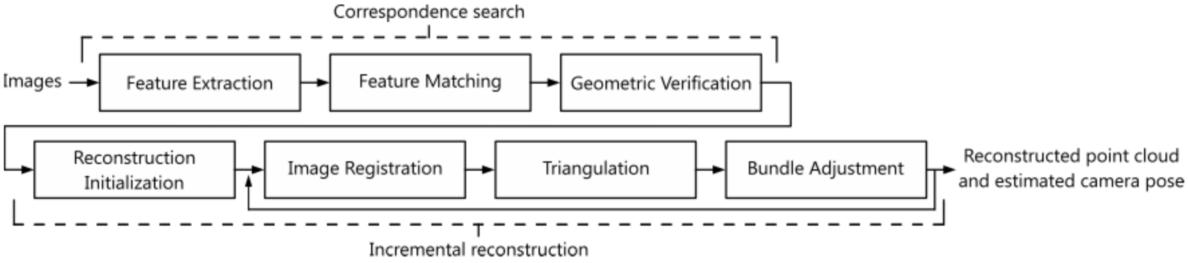

Figure 33: Incremental Structure from Motion pipeline [173].

Several alternative implementations of the incremental SfM pipeline have been developed throughout the years. COLMAP is an open-source implementation of the incremental SfM and MVS pipeline among the existing pipelines. The most common pipeline is presented by Schonberger, J. L. and Frahm, J., in which the major goal is to provide a general-purpose system that can be used to rebuild any scene while simultaneously improving resilience, accuracy, and scalability [169]. The C++ version also includes a user-friendly graphical interface for configuring pipeline settings. The sparse reconstruction can also be exported for use in other MVS pipelines [169,174]. The Graphical interface of COLMAP was exploited for 3D reconstruction for this thesis.

2.4.2 Principles

The building components of a typical incremental SfM pipeline are described in this section.

Feature Extraction states that for each image as input of the pipeline, a set of local features is generated to characterize the image places of interest (key points). Different solutions may be employed for feature extraction, and the algorithm used has an impact on the durability of the features and the efficiency of the matching phase. After obtaining key points and descriptions based on SIFT described in Section 4.2.1, the following stage is to look for correspondences of these points in various images [175]. Figure 34 b) illustrates the future detection (yellow dots) on a thermal image of the volunteer 1.

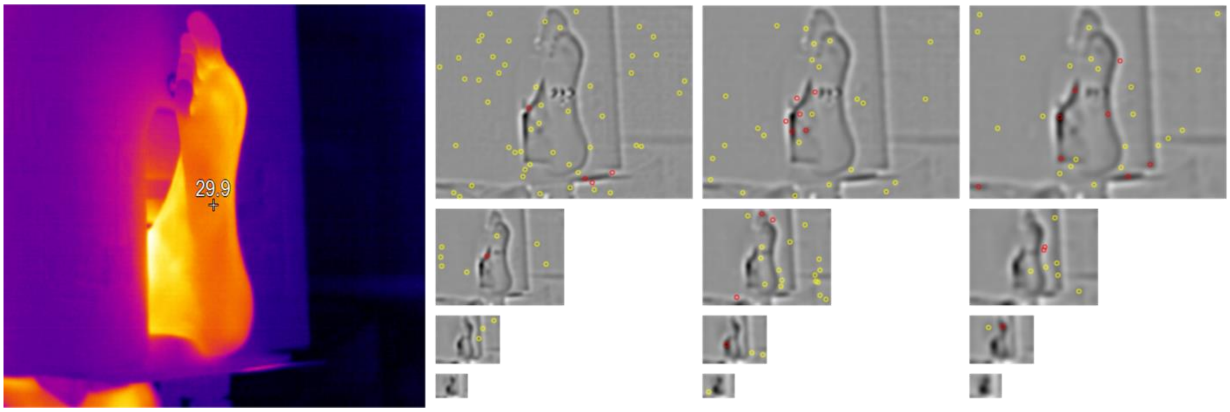

a)

b)

Figure 34: a) thermal image of the volunteer 1 foot, b) feature detection of the thermal image, each row represents the DoG filtering which causes blurring.

The key points and features extracted through Feature Extraction are utilized to determine which images depict common elements of the scene and are thus partially overlapping. Feature Matching is the term for this process. If two points in distinct photographs have the same description, they can be deemed to be the same in the scene in terms of appearance; if two images have a set of points in common, they can be said to depict the same part of the scene. Different ways can be employed to efficiently compute image matching; SfM implementations use these tactics. This phase produces a set of images that overlap at least in pairs, as well as a list of feature correspondences [175].

Because the preceding matching step primarily checks that pairs of images appear to have points in common, Geometric Verification is required. It is not guaranteed that identified matches represent true correspondences of 3D points in the scene, and outliers may be present. A geometric transformation must be found that successfully transfers enough common points between two images. If this occurs, the two images are regarded geometrically confirmed, implying that the points correspond to the scene geometry. Different ways of describing the geometric relationship between the images can be employed depending on the spatial configuration in which they were acquired. The transformation between two images of a camera that acquires a planar scene is described by a homography. Instead, if the camera intrinsic calibration parameters are known, the epipolar geometry allows the movement of the camera to be described using the essential matrix; if the values are unknown, the uncalibrated fundamental matrix can be used [169,175].

Because outliers frequently influence correspondences obtained during the matching phase, robust estimate techniques such as RANSAC must be used during the geometry verification step. The Scene Graph, a graph whose nodes represent images and edges connected to the pairs of images that are regarded geometrically confirmed, is the output of this phase of the process [176].

The initialization of the incremental reconstruction is critical since a faulty initialization leads to a bad three-dimensional model reconstruction. It is advisable to proceed with a dense region of the scene graph to ensure that the redundancy of the correspondences offers a stable base for the reconstruction. If the reconstruction begins with a limited number of images, the Bundle Adjustment procedure will not have enough data to adjust the location of the reconstructed camera poses and points, resulting in an accumulation of mistakes and a poor result. A pair of geometrically confirmed photos in a dense area of the scene graph are picked for the reconstruction initialization. If multiple image pairs can be utilized as a starting point, the one with the most geometrically evaluated matching points is chosen. The first points of the reconstructed cloud are the points in common between the two images; they are also utilized to establish the position of the first two cameras. Following that, the Image Registration, Triangulation, and Bundle Adjustment process incrementally add additional points to the reconstruction [169,173].

The initial stage in incremental reconstruction is image registration. A single image is contributed to the reconstruction at this step, and it is thus identified as a registered image. The position and rotation of the camera that has acquired the previously registered image must be computed; this can be done using the correlation with the known 3D points of the reconstruction. This stage utilizes the 2D and 3D relationship between the key points of the previous input image and the 3D reconstruction points associated with the key points of the previously registered images. To calculate the camera position, the position is defined in terms of the reference coordinates system, as well as the rotation. Outliers are frequently present in 2D-3D correspondences, and the approach uses RANSAC to generate an accurate estimation of the camera location and rotation. The addition of new points has not yet been enhanced by the new recorded image; this will be done during the triangulation phase [173,175,176].

The previous stage identifies a new image with similar points to the 3D cloud that has been reconstructed. New points may be detected by the new registered image; these points can be incorporated into the 3D reconstruction if they are recognized by at least one previously registered image. To determine the 3D coordinates of the additional points that can be added to the reconstruction and so build a denser point cloud, a triangulation method is performed. The triangulation issue begins with a pair of registered images with common points and an estimate of the respective camera positions; it then attempts to estimate the 3D coordinates of each common point between the two images. An epipolar condition is used to address the problem of triangulation. The positions from where the images were obtained must allow for the identification of the acquisition position of the counterpart in the image; these points are known as epipoles. The epipolar lines can be used to define the epipolar plane on which the point whose position needs to be evaluated in the ideal scenario. However, it is possible that the point does not fall in the exact intersection of the epipolar lines due to mistakes in prior steps of the pipeline; this error is known as a reprojection error. Special algorithms that account for the inaccuracies are required to solve this challenge [169,172,173].

Because the estimation of the camera location, orientation, and triangulation can result in defects in the reconstruction, a strategy to reduce the accumulation of such mistakes is required.

The goal of the Bundle Adjustment step is to prevent mistakes in the camera pose estimation from propagating to the cloud triangulation and vice versa [177]. Bundle Adjustment may thus be defined as the refining of the reconstruction that results in optimal values for the 3D reconstructed points as well as the camera calibration parameters. This phase is computationally demanding and must be completed for each image contributed to the reconstruction. To reduce processing time, it can be executed only for a small number of images/cameras, the most sequential ones; therefore, it is executed globally on all images only when the rebuilt point cloud has grown by at least a certain percentage [173].

2.4.3 3D Point Cloud Estimation and Camera Poses

The sparse point cloud can be compared to the ground truth of the reconstructed object. The distance between the reconstructed locations and the geometry of the ground truth is considered in the evaluation. After the reconstruction has been aligned to the ground truth, the rebuilt point cloud can be evaluated by computing the distance between the reconstructed points and the ground truth. Figure 37 b) shows the generation of the point cloud estimation from thermal images of a hand. It is possible to observe that the point cloud has errors (voids) because the cloud estimation is not possible only with false-color images due to the lack of borders and edges.

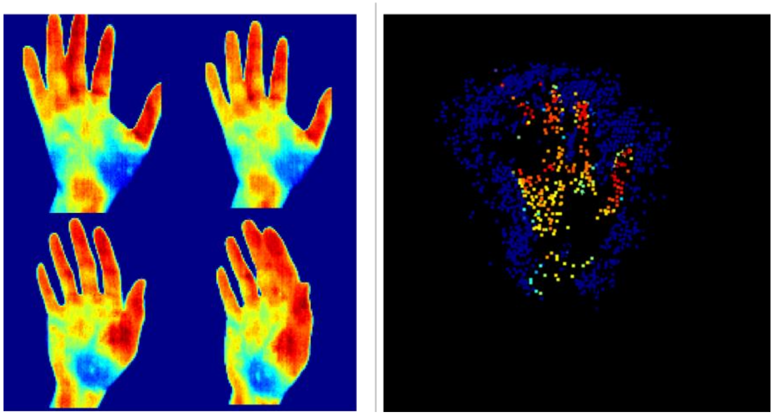

a) b)

Figure 35: a) Set of representative sequential images used for the estimation of the point cloud, b) estimation of the point cloud of a hand.

The distance can be calculated using the Euclidean distance if the ground truth is accessible as a dense point cloud. The closest point in the reference cloud is found for each 3D point of the cloud to be compared. The mean value and standard deviation are calculated when all distance data for all points in the cloud have been acquired. If the ground truth is in the form of a mesh, the distance between a reconstructed point and the nearest point on the mesh vertices is determined. For each vertex in the mesh, the algorithm searches for the point with the shortest square distance given a point from the reconstructed point cloud. The least-square distance is chosen among all the selected points (one for each triangle) and the square root of this value is returned. This calculation is carried out for each reconstructed cloud point. Even in this scenario, data structures can be utilized to partition the estimated space and accelerate computing. The mean value and standard deviation are calculated when all distance data for all points in the cloud have been acquired [175].

Only points corresponding to objects that are included in the ground truth model used for comparison must be included in the rebuilt cloud in both instances. Typically, the ground truth only comprises the reconstruction of the main object, ignoring the other elements present in the set of images. The distance estimate will be altered if the reconstruction involves areas of the scene that do not belong in the ground truth. To solve this problem, commonly the cloud of points from the reconstruction is removed, before calculating the distance. If this is not achievable, because each boundary between relevant and irrelevant elements is not easily distinguishable, the same effect can be obtained by providing a maximum distance for the reconstruction evaluation. If a reconstruction point is evaluated with a higher distance from the ground truth than acceptable, it is eliminated so that the total assessment is not affected [172,173,175].

The SfM pipeline provides the data on the camera poses (position and orientation) in addition to the sparse points cloud. Each camera pose can be compared to the related ground truth image. This method offers data on the distance between positions as well as the change in orientation between each pair of ground truth and predicted camera poses. In theory, if a camera is reconstructed in the same position as its ground truth, it can be assumed that it observes the same points and, as a result, its orientation is the same as the ground truth; however, minor differences between the orientations can be observed [172].

The Euclidean distance between the reconstructed position and the related ground truth camera position is used to evaluate the position of a reconstructed camera. The average distance and standard deviation can also be calculated using these variables. The angle of rotation required for the relative transformation that returns the reconstructed camera to the same orientation as the associated ground truth camera is used to assess the variations in camera orientation. This rotation angle can be used to assess the reconstructed camera rotation accuracy. When the reconstructed camera orientation is the same as the ground truth camera, the rotation angle of the defined transformation is 0; when the reconstructed camera orientation differs from the ground truth, the value of the rotation angle required to align the camera orientation also increases.

2.4.4 Multiview Stereo Basis

Multiview Stereo (MVS) refers to a series of steps that use stereo correspondence as their primary input and employ more than two images. MVS can collect multiple viewpoints in-between two images from two different viewpoints to improve robustness, for example, to image noise or surface texture. The quality of the input images and camera parameters determine how efficient an MVS algorithm is. Furthermore, the underlying SFM algorithms that generate the camera parameters pose, are a substantial part of MVS recent success [178]. A basic MVS pipeline is depicted in Figure 36, the illustration was taken from [178].

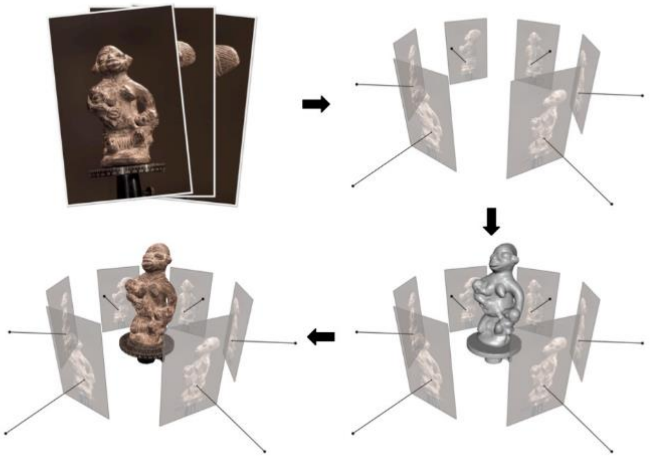

Figure 36: MVS pipeline process. In order, input images, posed imagery, reconstructed 3D geometry, and textured 3D geometry are shown clockwise [178].

Each of the main blocks may be implemented differently in various applications, but the overall approach is always the same: Collect images, calculate camera parameters for each image, then recreate the scene 3D geometry using the images and camera parameters (3D dense point cloud and surface reconstruction), and finally recreate the scene materials (mesh texturing). The collected images and the camera parameters were retrieved from the SfM method.

2.4.5 Surface Reconstruction

A meshed surface is built using the dense point cloud computed in the MVS stage. The meshed surface is formed by three vertices that define triangle facets. The meshed surface begins with a statistical outlier elimination that refines the point cloud [179]. Then, using the surface normal angles and the coordinates of the 3D points, the Poisson surface transformation generates a mesh. A refinement stage refers to the main surface, which improves the representation of the meshed surface [170]. The reconstruction of a surface from a set of false-color images of the hand is shown in Figure 37 b). Due to point matching issues, it is possible to see that the mesh is inaccurate concerning the anatomy of the hand.

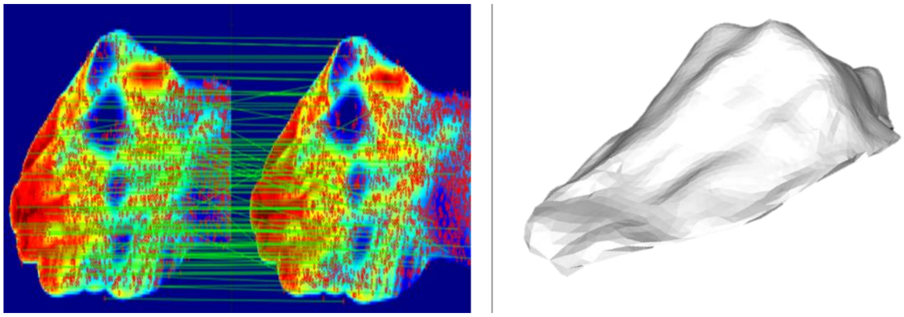

a) b)

Figure 37: a) pair of consecutive false-color images of the hand, b) reconstructed surface. The model is visibly imprecise due to the errors of the matching vectors. It is consequently recommended that images with visible spectrum scenes be included.

2.4.6 Texturing

Texture mapping is the last step in the 3D reconstruction process, and so it generates 3D surfaces with consistent colors and structures. To provide visually consistent scene rendering, the superimposition of 2D image texture information onto the meshed surface is critical. However, due to noise in the depth data, geometrical reconstruction errors of surface parts, substantial variation in the scale of the multiple accessible images, image blur, exposure differences from one image to another, occluded surface portions, texture mapping on meshed surfaces is a difficult task. The texturing method, when combined with efficient SfM and MVS phases, resulted in the reconstruction of precise extended 3D surfaces with remarkable texturing coherence [171,180]. Figure 38 b) depicts a reconstructed model with thermal image texturing based on the envelope texturing approach [98].

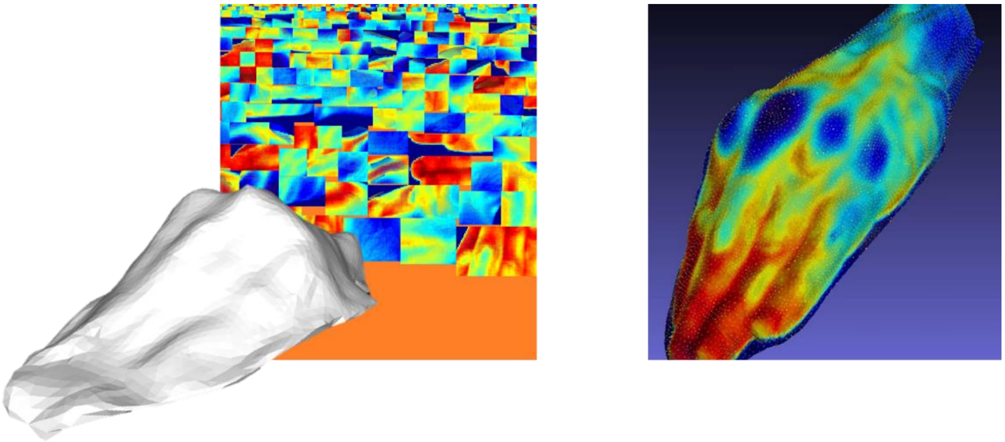

a) b)

Figure 38: a) MVS method generated mesh and texturing, b) 3D reconstruction of a hand with false-color texturing proportional to the temperature intensity collected by the thermal camera.

2.5 Conclusions

Medical IR is now supported by more clinical research around the world, employing state-of-the-art technology. Clinical data quantification, standardization, effective training with high-quality assurance, collaborations, and more publishing in prominent peer-reviewed medical journals must all be prioritized. The following areas are an efficient integration of actual state-of-the-art technology for IR imaging: IR imager and systems, advanced image processing, image and data analysis methods, protocol-based image acquisition, image interpretation, system operation and calibration, and a better understanding of the pathophysiological nature of thermal signatures. According to [45], Table 9 summarizes the minimum requirements for a thermal camera to be employed for a medical study.

Table 9: Key Camera Parameters in Summary [45].

Feature	Specification	Units
Format	Set of multiple images or video	
Compression	None	
Digitization (dynamic range)	12 minimum	bits
Array size	320 × 240 up to 640 × 480	Pixels
Sensitivity	0.04 - 0.1	◦C
Calibration accuracy	±0.3	◦C
Spectral band	LWIR, 8 - 14	μm

Medical imaging related to diabetic foot early diagnosis is still hard to achieve due to the multifactorial etiology such as. poor glycemic control, foot deformities, improper foot care, underlying peripheral neuropathy, poor circulation, etc. [73]. Currently, each accessible technique has limitations and advantages, implying that multimodal imaging is the best strategy for accurate diagnosis in diabetic patients. The use of IRT in the diagnosis of diabetes-related foot complications has been explored in the last decade as a perspective to find a correlation between surface temperature and vascular diseases Nevertheless, assuming that traditional IRT imaging is already widely studied, which is only partially true because some physicians recall that this technology in diabetic foot diagnosis failed at an early stage of development [181], multimodal registration expands IRT's function in medicine. Both modalities complement each other, as IRT provides metabolic functional information and visible-light pictures allow for the reconstruction of structural thermal characteristics, which can be used to supplement both functional and structural diagnostic data.

The fundamental reason for segmenting the foot is to avoid thermal interferences that could distort the results and lead to misinterpretation, even in a controlled environment. As demonstrated in this chapter, traditional methods cannot automatically segment the foot given an image in the worst-case scenario: uncontrolled environment, thermal interference, and temperature gradient similar to that of the scene. Due to these limitations, manual segmentation by a specialist is commonly requested, which is a disadvantage in terms of time and effort when handling a collection of several images. Therefore, it is proposed in this thesis the segmentation of the RoI based on the radiometric information (sensor data matrix or temperature matrix) so that the scene can be homogenized, which will lead also to improving the color mapping only in the RoI (foot).

A further major reason for segmenting the foot is to superimpose the false-color image on a scene from a visible light image, to detect more features that may enhance the surface reconstruction stage. The quantity of features detected in false-color images is commonly limited, which usually leads to wrong matching inliers, and in the best scenario, a low-quality surface (see Figure 38). Traditional image processing algorithms for thermal image segmentation for multimodal fusion, on the other hand, have limitations. Although it is now possible to segment manually, the thermal properties of the collected information are static, imposing restrictions. When working with a big collection of images, segmenting according to the threshold criterion of a specific temperature has several advantages, including the ability to improve the contrast of the RoI and automate the procedure. The superimposed images are essential as input for the SfM stage.

Standard SfM algorithms provide for precise and reliable point cloud calculation in a variety of scene types with textures and/or structures. Under the assumption that homologous points can be tracked using feature detection and matching methods for visible light images. However, in some medical scenarios, such as medical IRT, the use of feature detection and matching in SfM techniques is not ideal due to the lack of key points on false-color images. Despite the limitations of exploiting a set of false-color images, several medical applications have exploited the SfM approach to create 3D anatomical models [102,107].

The next chapter will introduce in detail the contribution of this thesis: radiometric data processing to automate the segmentation procedure relatively accurately respecting the traditional methods presented in this chapter.

Chapter 3

IR Radiometric Processing for Automatic Segmentation on Thermal Images

Contents

As discussed in the previous chapter, a collection of fused multimodal images is necessary for ensuring an accurate surface reconstruction. The required multimodal image is a false-color RoI superimposed into a visible light scene. This multimodal registration task is difficult, especially when there are interferences attributable to acquisition protocol mistakes (e.g. objects with heat sources or the personnel themselves). As a result, this chapter outlines the thesis strategy, which is to process radiometric data in a controlled environment.

3.1 Data Acquisition Protocols and Consideration

3.1.1 Instrumentation

The initial idea of this project was to use a low-cost LWIR sensor to conceive a portable prototype for sample collection in healthcare facilities. Table 10 shows the characteristics of the Lepton 3.5 radiometric LWIR sensor (Flir company, Orlando, USA).

Table 10: Technical features of the LWIR sensor Lepton 3.5 [48].

Characteristics	**Range/value**	**Units**
Infrared sensor resolution	160 x 120	Pixel
Pixel size	12	µm
Thermal Sensitivity	≤ 50	mK
Infrared Spectral Band	8 – 14	µm
Voltage	2.8	V
Refresh rate	8.6	FPS

The sensor is considered radiometric and of low scale (small size and portable). The participants of the project in which this thesis took place used this sensor in several other projects involving thermal pattern studies in diabetic patients [21,57,182]. However, the spatial resolution and pixel size challenged the finding of features within the region of interest. The information obtained by this sensor was further used only to test the robustness of the algorithms proposed in this thesis.

The instrument that best matched the needs of this project was the Fluke Ti32 thermal camera (Fluke, Everett, WA, U.S.A.), which has a multimodal recording of radiometric IR data and images in the visible spectrum. This sensor is usually used for industrial applications. The characteristics of this sensor were considered an advantage since the multimodal fusion of the two acquired images (IR and visible light images) would not require robust processing beyond scaling and translation. Each capture is stored as an IS2 file which contains the metadata, radiometric information, and visible-light images. The camera dimensions are 27.7 cm × 12.2 cm × 17.0 cm, with the advantage of being transportable to healthcare centers for future studies. The features are described in Table 11.

Table 11. Fluke Ti32 Commercial Thermal Imager characteristics [183].

Characteristics	Range/value	Units
Visible-light sensor resolution	480 × 640	Pixel
Infrared sensor resolution	240 × 320	Pixel
Temperature Range	−20 to +600	°C
Thermal Sensitivity	≤50	mK
Infrared Spectral Band	8–14	µm
Minimal focus distance	46	cm
Refresh rate	60	Hz

Figure 39 compares the pixel size quality of the two sensor modalities (IR and visible light) using images of the same subject.

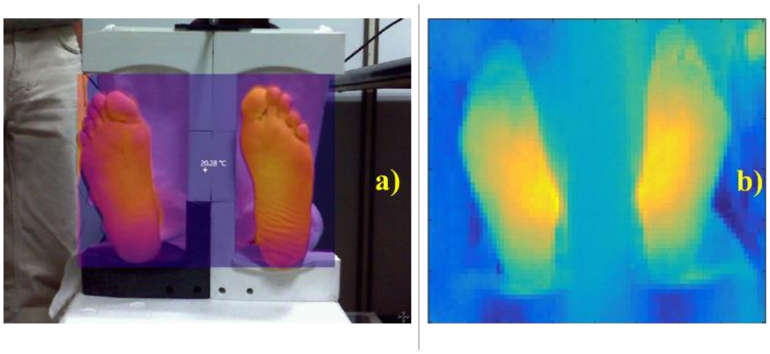

Figure 39: Volunteer samples IR images. a) False color image sample taken with the Ti32 thermal camera, b) IR image reconstructed with radiometric data of the Lepton Sensor. The image was taken from [21].

As discussed in Section 2.1.8, calibration is an important task for non-contact temperature measurement accuracy. Because IR energy is measured and interpreted as temperature, this method of measurement is known as "indirect measurement". For the thermal camera Ti32, a calibration was performed in a thermal bath under controlled conditions, obtaining thermographic measurements on a black body. The thermal camera emissivity was adjusted to 0.98 according to the value of a black body (phantom), which corresponds to the value of the emissivity of human skin.

3.1.2 Blackbody Design

A blackbody or an imaging phantom is required for accurate measurement in thermography. A theoretical blackbody has an emissivity of 1, which implies that the blackbody will absorb and radiates all the IR energy [135]. However, manufacturers produce black bodies with a coating material whose emissivity is as close as possible to a perfect black body. However, a perfect emissivity is very difficult to achieve. Thus, the materials commonly used material has approximately an emissivity of 0.98 [47].

The thermal calibration was performed with a 10 cm x 10 cm aluminum plate covered by black mate paint with a smooth texture. The blackbody was placed inside a sealed bin, to avoid direct contact with water (see Figure 40). The plastic bin was 3D printed with a polylactic acid film, which can isolate heat and not interfere with the thermal measurements. The dimensions of the bin were 10 cm^3. The reason for maintaining a matte surface was to avoid the reflection of light and IR energy from external sources such as laboratory lamps or personnel.

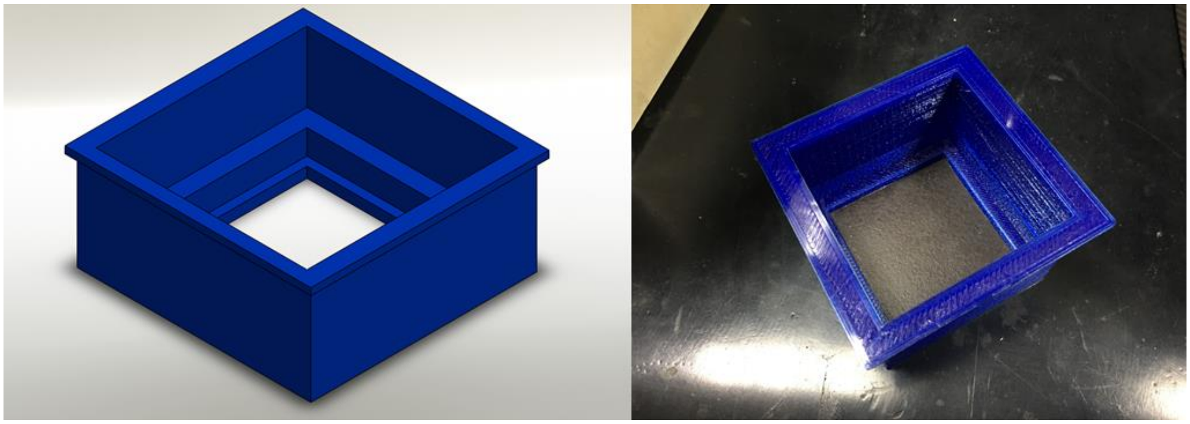

Figure 40: blackbody phantom and the designed bin printed with a 3D printer.

3.1.3 Thermal Calibration

Once the blackbody was built and the appropriate emissivity was chosen, a thermal calibration was performed with a blackbody metal plate to ensure the most accurate measurements. The thermal bath model is Haake P5 Circulating Bath w/ Thermo C10 Controller (Marshal Scientific, HN, USA), with the characteristics described below in Table 12.

Table 12. Haake P5 Circulating Bath operation characteristics [184].

Characteristics	Range/Type	Units
Operating temperature	-30 – 100	°C
Temperature accuracy	0.02	±K
Circulation capacity (open tap)	17	l/min
Immersion depth	From 85 up to 140	mm
Temperature setting	digital	-
Temperature display	Green LED	-
Control type	PID	-
Control sensor	Digital IC	-

Thermal baths are a recognized solution to provide controlled and fixed temperatures using circulating water. With thermal baths, the temperature over the black body is statically maintained constant. However, a gold standard thermometer was additionally placed to ensure that the temperature is accurately known and constant. The bin including the black body was placed inside the thermal-static bath and the thermal camera was fixed 20 cm over the black body surface, as depicted in Figure 41. The water temperature was set from 22°C to 44°C in 2°C increments, with a settling time of 2 min at each step to stabilize the black body temperature.

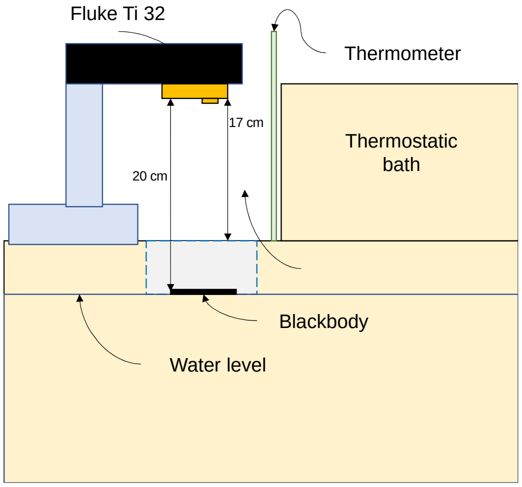

Figure 41: Controlled system diagram from thermal calibration.

The radiometric measurements were performed with two different cameras (i.e., the Lepton 3.5 and Fluke Ti32 cameras), to characterize and compare the Lepton 3.5 sensor against the Ti32 equipment. The objective of the characterization was to obtain a mathematical model capable to predict temperatures in Celsius degrees using the radiometric information of the Lepton 3.5 camera; this calibration was done, with the factory settings [67], since the Lepton camera is not able to determine temperature values. The proposed characterization will allow the further development of thermographic studies with low-cost sensors and the implementation of neural networks for the detection of thermal patterns [74]. However, the thermal equipment used for the 3D modeling of feet was the Ti32. The temperature was recorded in the center of the black body, in which it was observed that the temperature was homogeneous on the black body surface, as illustrated in Figure 42. The calibration results are presented in Section 5.2.

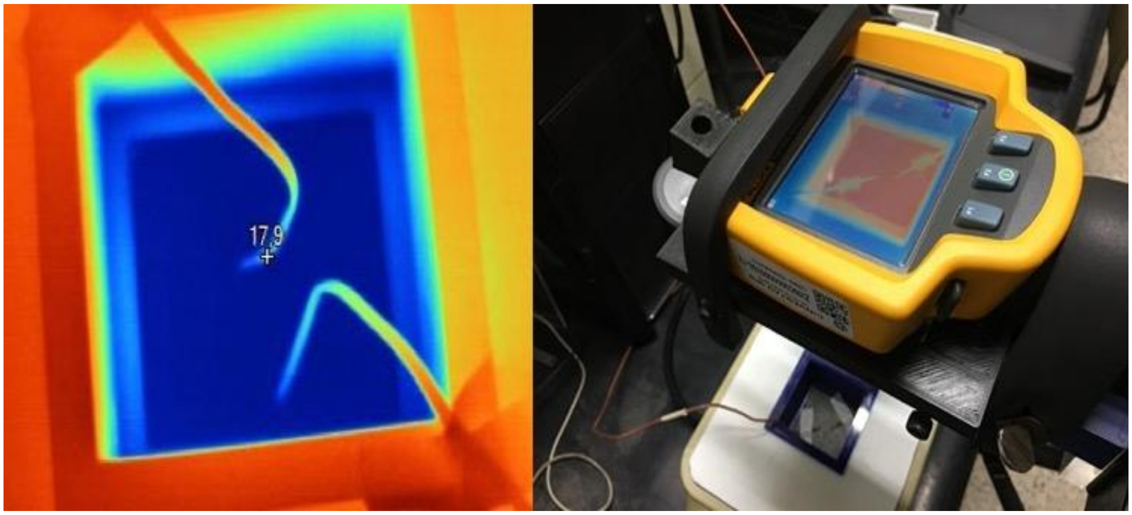

a) b)

Figure 42: a) thermal image of the phantom at 17.9°C, b) Fluke Ti32 in the thermal calibration process.

3.1.4 Volunteer Selection

A public invitation was issued for the recruitment of volunteers. Given that the project does not involve invasive or medical procedures, recruitment did not require volunteers with specific characteristics (sex or age) or a history of DM. Informed consent was given under the guidelines of the World Health Organization [185]. Two volunteers accepted the invitation and were informed that their integrity, identity, and health will not be exposed during and after the development and publication of this project.

3.1.5 Sampling Protocol

Medical IRT requires controlled conditions to avoid thermal interferences with the environment that could decrease the contrast in the RoI. Several authors proposed to use enclosures to cover the lower limb and foot, allowing the thermal camera to record just the IR radiation emitted by the body. Maldonado et al. [75] tackled the challenge relating to an uncontrolled environment by implementing Machine Learning segmentation of the foot sole and by using a segmentation mask. The limitation is that obtaining such a mask requires visible light images, which means that research should use multimodal capturing equipment. It is currently not recommended to collect thermal imaging outside of controlled environments. An acquisition protocol must be defined in a controlled environment to obtain images and information without thermal interference. However, diagnosis and monitoring in an uncontrolled environment by front-end equipment is a fundamental objective [75].

Therefore, a semi-controlled environment was designed based on support for the volunteer or patient foot and a thermal insulating background made of extruded polystyrene with a size of 40 cm x 30 cm (Figure 43 depicts the setup for this thesis).

Each volunteer was placed with the right lower limb in a straight position and was instructed to keep the foot as much as possible in a fixed position. The proposed protocol was based on passive thermography, in which the foot was exposed for 15 minutes to room temperature to generate a thermal equilibrium and avoid drastic temperature changes. The images were taken in a radial sequence every 12°. Sudden temperature fluctuations could cause surface distortions or loss of correlation at the feature-matching stage between two consecutive images.

a) b)

Figure 43: Foot posture during the image acquisition. a) Lateral view of the foot on the resting base. b) Frontal view. It is noteworthy that the pink background foam is large enough to isolate the foot from the remaining body of the volunteer so that the IR radiation does not interfere with the captured frame.

Although the acquisition system presented in this thesis is not a sealed container, the pink board was enough to avoid IR interferences or temperature changes in the scene that may be induced by the volunteer himself or heat sources. Temperature fluctuations were prevented because the laboratory where the samples were acquired had closed areas. Thermal interference was also prevented by placing the volunteer body behind the foam backing on the XPS Insulation Foam Board made from polystyrene resin (pink board). The board size was 40 cm × 50 cm.

The camera was placed at 95 cm from the foot, perpendicular to the sole, and rotated every 12° around the resting chair to obtain 15 captures per volunteer, i.e., 15 visible-light frames and 15 radiometric data arrays from left to right viewpoints of the foot. The equipment was fixed on a tripod to avoid motion artifacts during the acquisition time. The acquisition time between two consecutive images was 13 s. Additionally, with the controlled environmental conditions, airflows were avoided so that the acquired surfaces do not have drastic temperature variations. The acquisition trajectory is illustrated in Figure 44.

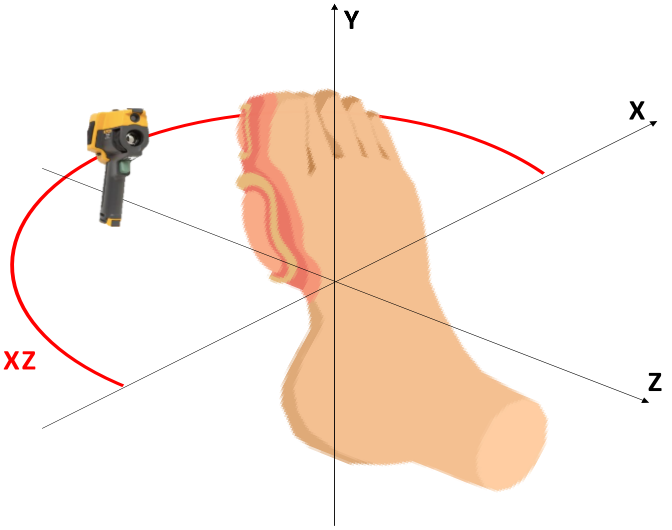

Figure 44: The sequence trajectory in the XZ plane is represented by the red arc. The camera was placed in a vertical position regarding the foot.

3.2 Angular Emissivity Correction

As discussed in Section 2.1.6, a limitation in the temperature acquisition with a circular trajectory lies in the high probability of angular emissivity on curved surface parts despite the uniform temperature distribution along the skin surface. This physical factor impacts the precision of the relative temperature recording and induces errors for image acquisitions at different angles [186]. The precision requirements are substantially higher in clinical thermal imaging than in numerous non-medical applications. Thus, the temperature inaccuracies caused by the human skin viewing angles must be precisely assessed. There are currently just a few measurements of this variation that are based on a model that assumes a dielectric contact. Watmough et al. were the first to identify and evaluate this impact in 1970 [83].

It exists models to correct temperature changes due to high viewing angles. The approach proposed by Cheng et al. [130] suggests a model related to directional emissivity for the error measurement, as described in Equation (21).

$$\Delta T = \frac{T_n - T(\theta)}{T_n - T_a} \qquad (21)$$

where ΔT is the temperature error normalized to the range [0,1], T_n is the temperature measured at a normal angle (i.e., 90°), $T(\theta)$ is the temperature obtained at any viewing angle different from the normal angle, and T_a is the room temperature (i.e., 20 °C for our study).

Two factors influence the temperature of the radiation emitted by a curved surface: the travel distance and the viewing angle. Cheng et al. [130] employed a flat copper plate with dimensions of 210 mm x 157 mm and flowing water at 26.4 °C. The copper plate is first mounted perpendicular to the camera axis during the imaging session and then rotated to collect pictures at 5 angles going from 10 to 60°, with a 10° increment. Data from the central portion of the plate was evaluated at each angle to minimize edge effects and reduce noise [83]. This approach is similar to the thermal calibration presented in this thesis, with the exception that it was carried out for calibration at normal incidence angles. The approach of Cheng et al. is adaptable for the goals of this thesis.

The average temperature in a homogenous area of the images is essential due to Equation (21) may estimate the temperature correction in terms of percentiles regarding the angle view (taking the normal angle as reference). For each sample, the average temperature was retrieved between the metatarsal and heel zone since they presented a homogeneous distribution, and the area is visible within each image. The average temperature was extracted in this thesis by using the Fluke SmartView software, which is a camera file manager developed by the same manufacturer. Each file has a different extension. An IS2 file provides false color and radiometric image data that allow the point temperature of each pixel to be seen. It is possible to define rectangular regions in the software to extract the average temperature in each homogenous area. A total of 8 images were taken into account, from 0° to 90°, to compute an average temperature of a region on the sole. Figure 45 shows two of the most typical samples, one with normal incidence and the other with perpendicular incidence, in which the average temperature was computed within the marked rectangles

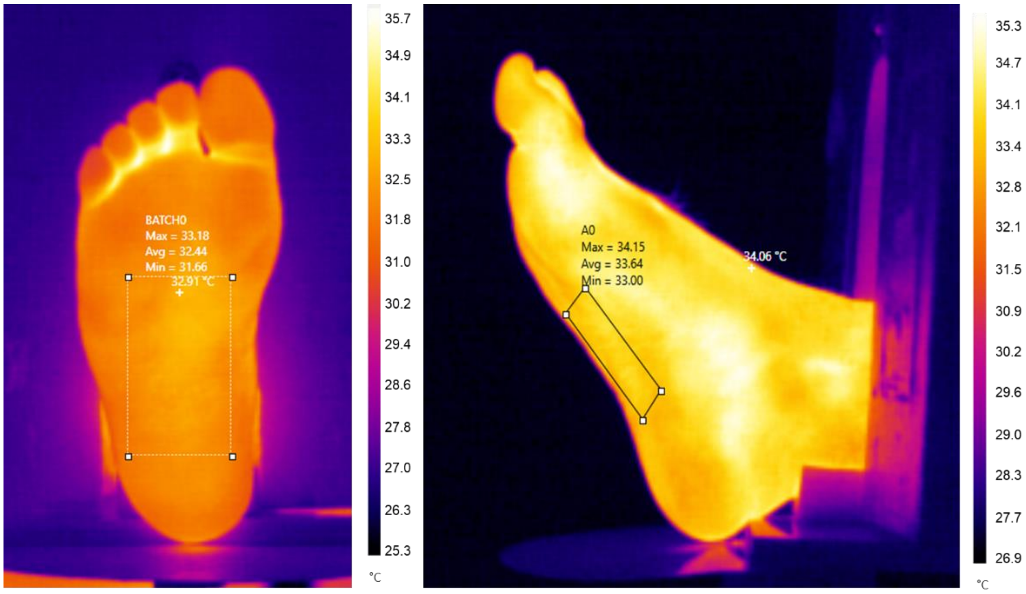

a) b)

Figure 45: Thermal images taken from different viewpoints. a) Reference image at a normal angle. b) The last image is at a 90° angle position. For each sample, the average temperature was retrieved within a marker box.

Lastly, the normalized temperature differential ΔT is given as a function of viewing angle θ. In medical IRT, the measurement errors due to curvature effects may be corrected by knowing the orientation of the thermal camera regarding the body and the ambient temperature. Thermal Camera Data Extraction

3.3 Thermal Camera Data Extraction

Thermal imagers have become more common in medical IRT as they have improved in economic and technical aspects. With the introduction of low-cost sensors (e.g., Flir Lepton), radiometric thermal images may be captured not only with hand-held measurement equipment but also with compact or mobile phone-integrated devices. Stijcsics et al. and van Doremalen et al. have employed these sensors for radiometric research objectives, and they have now devised ways to increase their accuracy [33,187]. In addition, the quality of these sensors is comparable to that of professional systems (which have a resolution of around 1 megapixel), but they are considerably smaller and less expensive. The thermal imaging information can be stored as raw data or as processed data. Uncooled array sensors are equipped with a microbolometer array that can save a file in raw format (i.e. radiometric array) without adjustment, allowing the reconstruction of a thermal image from many input images with higher resolution after post-processing.

Thermal cameras with multimodal sensors (visible light and infrared) are more prevalent, but their cost is still relatively high. In the case of visible light sensors, photogrammetry is a common solution for surveying objects with a large area because the typical hand-held camera has a resolution of 16-20 megapixels. The advantage of high-resolution images is that feature detectors and feature matching algorithms work reliably and with few errors. With the required hardware resources and minimal post-processing, a high-resolution large-scale 2D and 3D reconstruction can be carried out. However, due to the low thermal camera resolution and the lack of details seen in these data (low contrast), 2D or 3D homologous information matching is not possible since a sufficient quantity of feature points cannot be extracted from 160x120 pixel images.

The advantage of radiometric equipment, like the one described in Section 2.2.4, It is possible to extract sensor data arrays before reconstructing an image. Each value is equivalent to the quantity of IR energy measured by the bolometers, allowing for consistent temperature readings. The reading of radiometric data with a computer can be difficult depending on the chosen thermal camera or sensor. The physical (hardware) driver, for example, is used to extract data from the LWIR Lepton 2.5 and 3.5 sensors, allowing the data to be retrieved directly in MATLAB as if it were an image sensor (Figure 46).

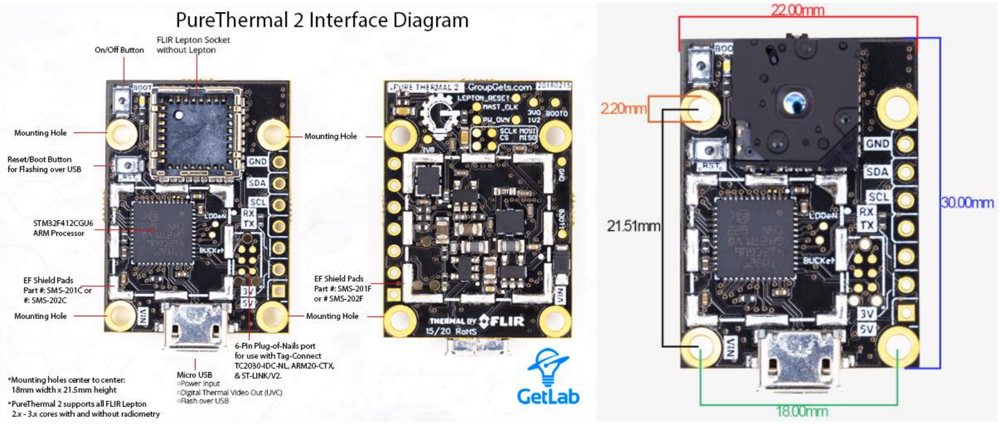

Figure 46: PureThermal 2 Smart I/O Module with USB webcam break board that works with the FLIR Lepton thermal imaging camera core. This board is capable to communicate with a computer to retrieve thermal images. The image was taken from [16].

However, in the case of the Ti32 thermal camera, the metadata of the IS2 files must be extracted. Several authors have volunteered to contribute to the development of MATLAB scripts for extracting information from the Fluke Ti series. Beauducel proposed a code for the extraction of information from Ti32 camera files such as visible light images, false-color images (thermal images), and radiometric data [16]. Although the Ti32 thermal camera has management software (SmartView), automated processing for specific purposes such as the foot segmentation in the RoI is not available. The data was extracted from each IS2 file with a version of the READIS2 MATLAB code. The code was modified for this project so that the extracted 14-bit radiometric data can be interpreted as temperatures given in Celsius degrees and exported in text format (TXT) files. The visible-light images were extracted in a Portable Network Graphics (PGN) file format. The generalities of radiometric data arrays will be discussed in the following section.

However, the extraction code is specific for the Fluke Ti32 model. For IR sensors that are composed of an array of bolometers, it is possible to extract data in the form of matrices (also known as heat maps when interpreted by a mathematical model). In particular, the image capture code can be modified to obtain a file with a different extension, including a text file with a matrix generated from the captured sample. This allows data processing to obtain a temperature distribution in the regions of interest. The IR sensor array will adjust the radiometric values concerning the warmest area detected on the scene; therefore, it is commonly suggested to keep a static environment to avoid wrong measurements when the device is not capable of refreshing the bolometers [75,188].

3.3.1 Radiometric Data Arrays

Raw sensor data is a term that refers to a collection of the radiometric array (multiple matrices structure). The Ti32 and Lepton 3.5 cameras have a 14-bit resolution to encode the signal. Figure 47 illustrates a Lepton 2.5 encoded data since this sensor is not capable of producing a false-color image before additional processing (such as a code to map each value to a color palette).

```
8056 8057 8054 8044 8049 8045 8032 8029 8026 8018 8018 8014 8012 8009 8007 8009
8002 7998 7998 7997 8014 8014 8036 8243 8284 8281 8284 8297 8331 8333 8337 8336
7997 7987 7982 7988 7998 8002 8006 8005 8008 8015 8019 8024 8027 8029 8028 8025
8056 8054 8058 8052 8057 8049 8033 8024 8023 8022 8019 8013 8012 8006 8006 8007
8001 7999 8002 8044 8208 8210 8199 8305 8292 8278 8284 8315 8323 8323 8328 8326
7991 7984 7979 7989 7997 8004 8004 8009 8006 8016 8018 8023 8026 8032 8026 8028
8042 8040 8045 8042 8050 8044 8030 8024 8021 8019 8015 8014 8009 8005 8003 8009
8004 8006 8030 8190 8321 8331 8335 8340 8311 8293 8312 8322 8320 8323 8326 8324
8014 7995 7986 7991 7997 8005 8004 8007 8008 8016 8022 8024 8030 8027 8028 8028
8030 8028 8032 8029 8032 8028 8024 8018 8017 8013 8014 8012 8007 8009 8007 8008
8024 8035 8138 8328 8341 8345 8347 8345 8328 8312 8280 8318 8319 8324 8326 8319
8150 8005 8003 8000 8000 8005 8008 8011 8010 8017 8019 8022 8027 8030 8024 8025
8021 8022 8023 8019 8021 8019 8017 8014 8012 8011 8008 8008 8004 8009 8007 8007
8159 8245 8324 8354 8348 8348 8346 8341 8323 8313 8208 8294 8328 8324 8327 8318
8183 8185 8081 8006 8003 8005 8006 8012 8013 8014 8021 8020 8022 8024 8025 8023
8010 8015 8017 8011 8015 8019 8015 8012 8012 8007 8006 8007 8002 8008 8005 8006
8361 8365 8371 8374 8359 8347 8342 8337 8314 8306 8270 8304 8337 8326 8316 8312
8163 8181 8134 8034 8007 8006 8012 8013 8012 8018 8020 8018 8020 8023 8029 8022
8002 8009 8015 8007 8009 8010 8012 8008 8011 8006 8006 8006 8006 8005 8002 8005
8376 8378 8375 8374 8373 8358 8343 8327 8309 8295 8289 8299 8322 8318 8318 8303
8157 8169 8145 8074 8007 8009 8008 8011 8011 8015 8018 8020 8020 8022 8024 8025
8003 8008 8011 8002 8005 8011 8009 8008 8009 8009 8004 8007 8007 8004 8005 8005
8382 8377 8377 8370 8369 8349 8324 8314 8306 8299 8288 8279 8288 8290 8294 8293
```

Figure 47: The Lepton 3.5 sensor digitized radiometric data is represented as a matrix. The numbers correspond to IR energy measurements in a 14-bit scale.

It is worth noticing that, since the measured value is an IR light energy, the digitized data is not directly exploitable in terms of temperatures for medical purposes. Sensors with microbolometer arrays also have a reference point based on the warmest spot in the captured frame. To avoid interference, the data collecting process must be kept in a controlled environment. When a portion of the field of view is warmer than the remainder of the field of view, contrast reduction occurs. Figure 48 shows an example of contrast reduction when a region is hotter than the rest of the capture frame.

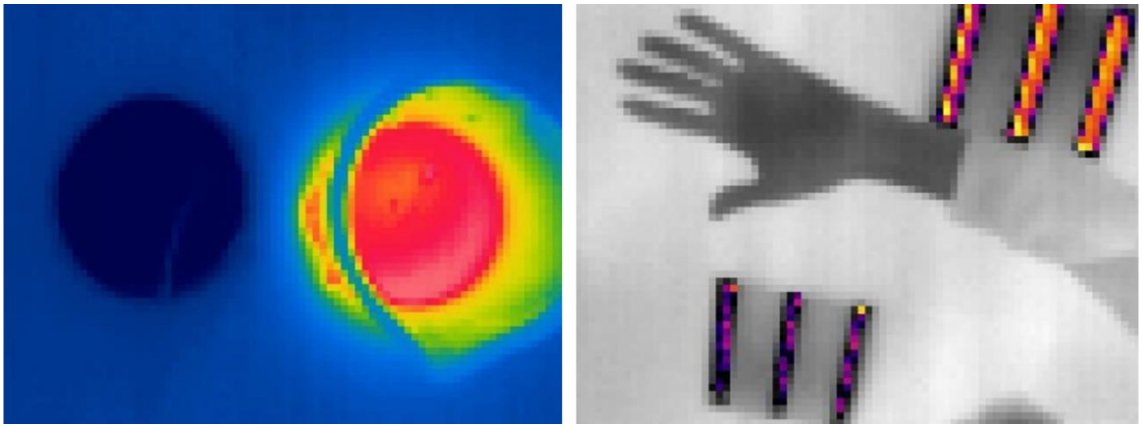

a) b)

Figure 48: False-color images reconstructed from radiometric information of the Lepton 3.5 sensor, a) thermal image of two humid phantoms, the body on the right side takes all the contrast so that the temperature distribution in the cold phantom on the left is almost imperceptible: b) thermal image in which it can be observed that the temperature distribution of the hand was strongly reduced due to the temperature of the ceiling lamps.

3.3.2 Visible Light Image Extraction

The Ti32 thermal camera is a multimodal device. In addition to IR thermal data, visible light images can be acquired with this camera. The manufacturer's SmartView software allows the manual extraction of both monochromatic images and false-color images; this manual operation must be carried out by an expert who is familiar with the camera software. However, when dealing with several files or a database's numerous acquisitions, the data extraction is very time-consuming. Beauducel [188] modified the data extraction code to automate the extraction process of visible light images and radiometric data.

Because the metadata in the IC2 files is arranged in vector form, it is important to find the exact location of the relevant data for this study, i.e. visible light images and radiometric arrays.

The vectors carrying the radiometric information, the size in pixels of the thermal images, and the images in the visible light spectrum are shown below in lines of the updated Beauducel code.

```
% get IR parameters
emissivity = double(typecast(d(2940:2941),'single'));
transmission = double(typecast(d(2942:2943),'single'));
backgroundtemp = double(typecast(d(2944:2945),'single'));

% IR image size
irsz(1) = double(typecast(d(7984:7985),'uint32'));  % 320
irsz(2) = double(typecast(d(7986:7987),'uint32'));  % 240

% visible image size
visz(1) = double(typecast(d(2930:2931),'uint32'));  % 640
visz(2) = double(typecast(d(2932:2933),'uint32'));  % 480
vsz = [visz(2),visz(1),3];      % [480,640,3]
```

3.4 IR Radiometric Data Processing

Commonly, when an IRT study is carried out, the object of interest is warmer than the scene under certain conditions. [189,190]. This fact enables a high contrast between the RoI (including the pixels with the temperatures to measure) and the background, leading to a relatively easy way to segment the RoI. However, the capture may be affected by heat interferences due to various external factors, such as lamps, electronic equipment, surrounding people, thermal shadows, reflections, or even the volunteer body heat. The flowchart presented in Figure 49 summarizes the overall process for extracting and processing the information. The input is a temperature matrix, while the output is an IR false-color image with the segmented RoI in the jet colormap code (blue to red). Each radiometric array was converted to a false-color image in which the colors have a direct correlation to the temperature intensity measured in each frame.

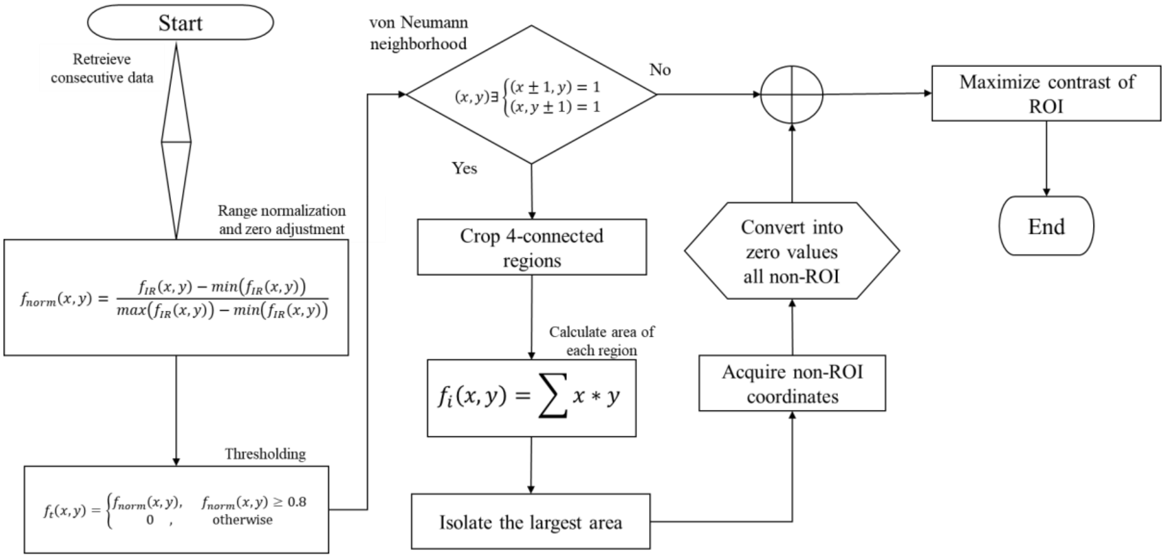

Figure 49: Flowchart of the radiometric data processing to obtain a segmented IR image. This flowchart was proposed for IR data without interferences or non-desirable artifacts.

The main idea of this chapter is to describe the management of radiometric data from a signal processing point of view and not as a reconstructed false color image. The first step is the normalization of the temperature arrays extracted directly from the sensor. Thresholding the data allows discerning between the region of interest and the scene components that are considered as thermal artifacts. However, some captures may still contain thermal artifacts which are removed by detecting connected regions and simply discarding all those that are smaller than the region of interest. The combination of these steps allows the segmentation of the region of interest without the intervention of a specialist who separates each region of the scene by hand.

3.4.1 Range Normalization

The Normalization aim is to modify data sets whose values are in intervals defined by variable limits, so the information can be rearranged within intervals (often the lower and upper bounds of the modified data sets equal 0 and 1, respectively). The data set must not be affected after normalization. Every dataset does not need to be normalized for digital image processing. This is only needed for radiometric processing when features have distinct ranges.

The first step was to perform a normalization of the radiometric data $f_{IR}(x,y)$ so that the value $f_{norm}(x,y)$ belongs to the [0,1] interval (Equation (22)).

$$f_{norm}(x,y) = \frac{f_{IR}(x,y) - min\big(f_{IR}(x,y)\big)}{max\big(f_{IR}(x,y)\big) - min\big(f_{IR}(x,y)\big)} \tag{22}$$

Also, range normalization enhances the contrast of the image in this step. Assuming a matrix of size 4 x 4 of random and independent values, Figure 50 depicts the advantages of normalization instead of employing raw data.

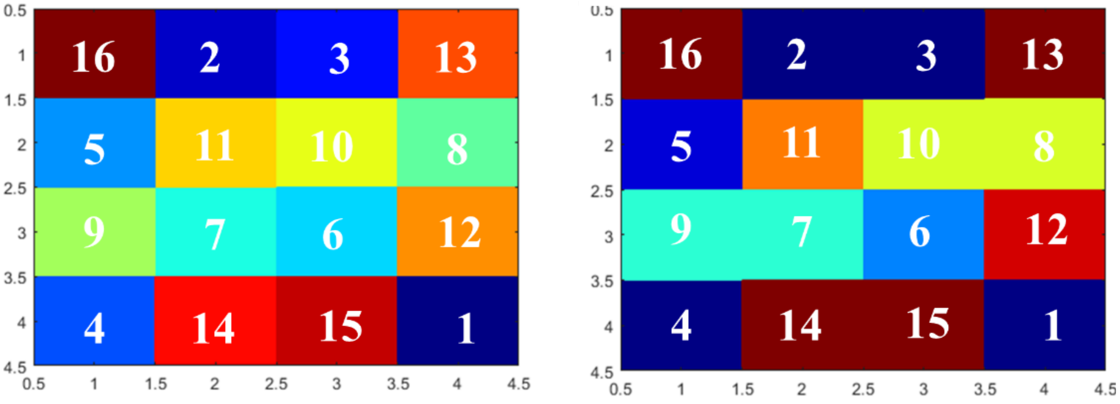

a)

b)

Figure 50: a) Matrix normalized which original values are from 1 to 16, b) matrix without normalization. It is possible to observe that in the case of values 8, 10, and 13-16 the same false colors are maintained, which may reduce the visual contrast of perceptible temperature differences. For the normalized matrix, the value 1 corresponds to 0 and 16 to 1.

3.4.2 Thresholding Segmentation

The values of the normalized matrices are typically greater than 0.8 for pixels belonging to the RoI and smaller than this threshold for background pixels. As seen in Equation (23), the values below 0.8 are set to 0, whereas the other values remain unchanged (see Figure 23).

$$f_t(x,y) = \begin{cases} f_{norm}(x,y), & f_{norm}(x,y) \geq 0.8 \\ 0 \quad , & \text{otherwise} \end{cases} \tag{23}$$

where $f_t(x,y)$ is an array with the thresholded values and $f_{norm}(x,y)$ is the normalized array. However, in the first iteration of thresholding, values greater than 0.8 are not contrasted with each other since these values are similar. For this reason, a second iteration is required to improve the contrast only of the thresholded values from the first iteration, as depicted in Figure 51.

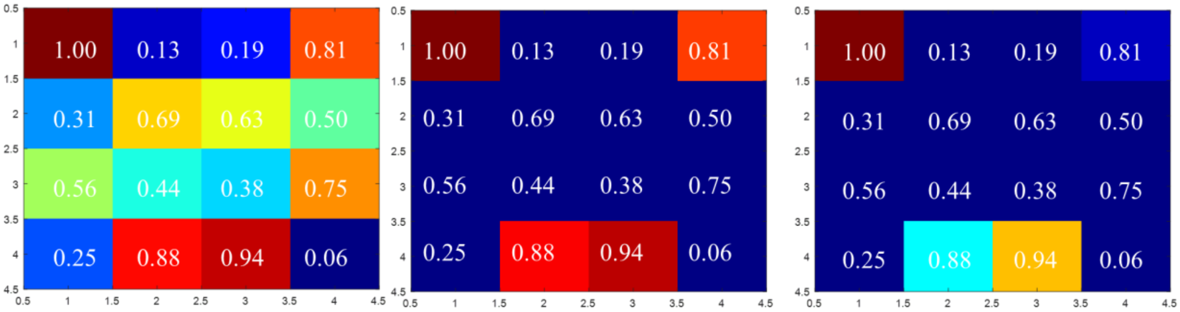

1.00	0.13	0.19	0.81
0.31	0.69	0.63	0.50
0.56	0.44	0.38	0.75
0.25	0.88	0.94	0.06

a)

1.00	0.13	0.19	0.81
0.31	0.69	0.63	0.50
0.56	0.44	0.38	0.75
0.25	0.88	0.94	0.06

b)

1.00	0.13	0.19	0.81
0.31	0.69	0.63	0.50
0.56	0.44	0.38	0.75
0.25	0.88	0.94	0.06

c)

Figure 51: a) Original matrix with normalized values in the range [0,1], b) thresholded matrix $f_{norm}(x,y)$ in which it can be observed that the values selected by the thresholding have similar colors (i.e., similar monochromatic values after the IR conversion), c) matrix thresholded a second time to achieve a maximal contrast between the thresholded values in (b).

3.4.3 Region of Interest Contrast Enhancement

In the previous step, the values below 0.8 were set to zero, converting thus the corresponding pixels in background components. The values higher than 0.8 were kept as their normalized original value. Equation (23) homogenizes the components of the background, removing several interferences in the background. Equation (24) shows how binary image $f_{bin}(x,y)$ is obtained with $f_t(x,y)$.

$$f_{bin}(x,y) = \begin{cases} 1, & if\ f_t(x,y) > 0 \\ 0, & otherwise \end{cases} \tag{24}$$

However, some IR interference may be strong enough to remain present in the background of the thresholded array $f_t(x,y)$. In the binarized image *fbin(x, y),* these artifacts correspond standardly to isolated objects with a small area concerning the RoI. The non-desirable regions and the RoI can be seen as 4 connected neighborhood regions with a Manhattan distance of r = 1. The RoI and the interferences can also be seen as islands that have a similar temperature. The RoI is always located in the center of the frame with a greater area than the non-desirable objects due to the IR interferences. For this reason, instead of using morphological operators such as erosion and dilation, the largest and central areas were segmented considering that RoI has the largest area and, commonly, it is always centered while interfaces may be located at the borders of the image (see Figure 23) to find the sub-image, i.e., the foot. The values of the pixels corresponding to non-RoI objects are simply set to 0. The binarized images are essential for retrieving the coordinates of the RoI, extracting the original values of the thresholded array $f_t(x,y)$ that correspond only to the foot. Afterward, the data of the sub-array from $f_t(x,y)$ was displayed as a false-color image with a Jet colormap range from blue to red. The blue color corresponds to the lowest value (i.e., zero) while the rest of the colors were mapped only on the RoI. Figure 52 shows the results of the thresholding segmentation with radiometric information for the reconstruction of a segmented false-color image. A sample with thermal interference was used to demonstrate the robustness of the segmentation and RoI contrast enhancement steps.

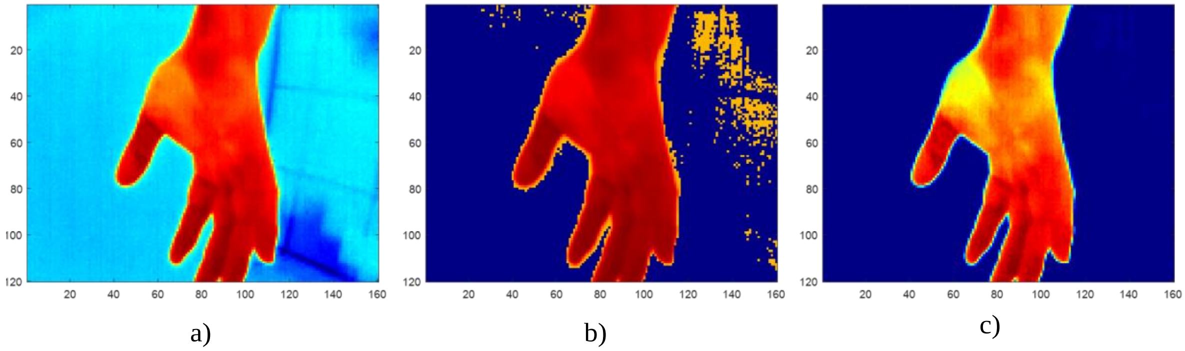

a) b) c)

Figure 52: a) thermal image reconstructed with an original IR data matrix, b) thresholded thermal image: thermal interferences remain due to the similarity of their temperatures and those of the RoI (the RoI lacks adequate contrast), c) thermal image after second thresholding which enhance the hand contrast and eliminates surrounding interferences visible in b).

3.4.4 Thermal Image Reconstruction

The figures displayed above focus on the segmentation of data relating to radiometric values. However, it has not yet been shown how an IR data matrix can be converted into a false-color image.

Let be an array $C \in \mathbb{R}$, which has radiometric values out of the sensor. The fundamental idea is to display C as an image that employs at best RGB tri-stimulus values to represent IR values by colors. The color of one pixel of the image must be fixed according to the value of the corresponding element of the matrix. C is a m x n pixel grid, where m stands for the number of rows and n defines the number of columns. The centers of the pixels are associated with the element's row and column indices. The color values are returned in a three-column array with the same number of rows as the current figure colormap. The number of rows is equal to the default length of 256. The red, green, and blue intensities for each color are shown in each row of the array. The intensities are between 0 and 1. Figure 53 depicts the process of obtaining raw data, characterization (which yields a temperature map), reconstruction (which yields an image), and ultimately segmentation.

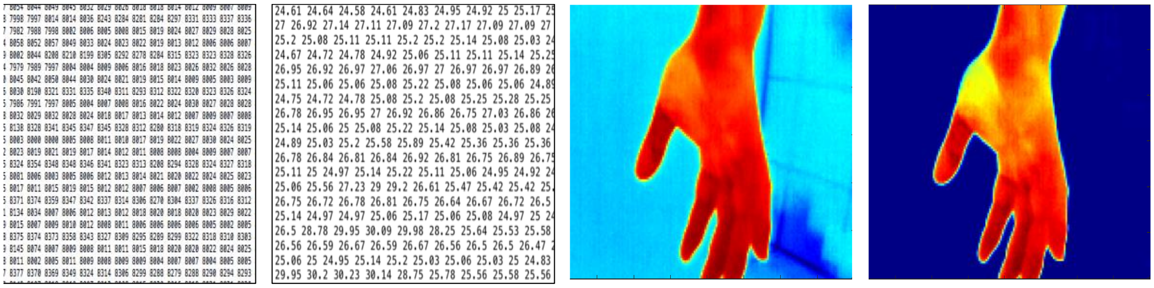

a) b) c) d)

Figure 53: a) radiometric data, b) temperature prediction in Celsius degrees using a mathematical model based on the characterization, c) reconstructed thermal image, d) segmented hand (RoI).

Figure 54 presents the algorithm to achieve a false-color image out of radiometric data. This procedure only applies to the Fluke Ti32 camera since it is equipped with two aligned cameras. If it is intended to employ independent sensors or cameras, it is then suggested to refer to the image registration described in Section 2.3.3.

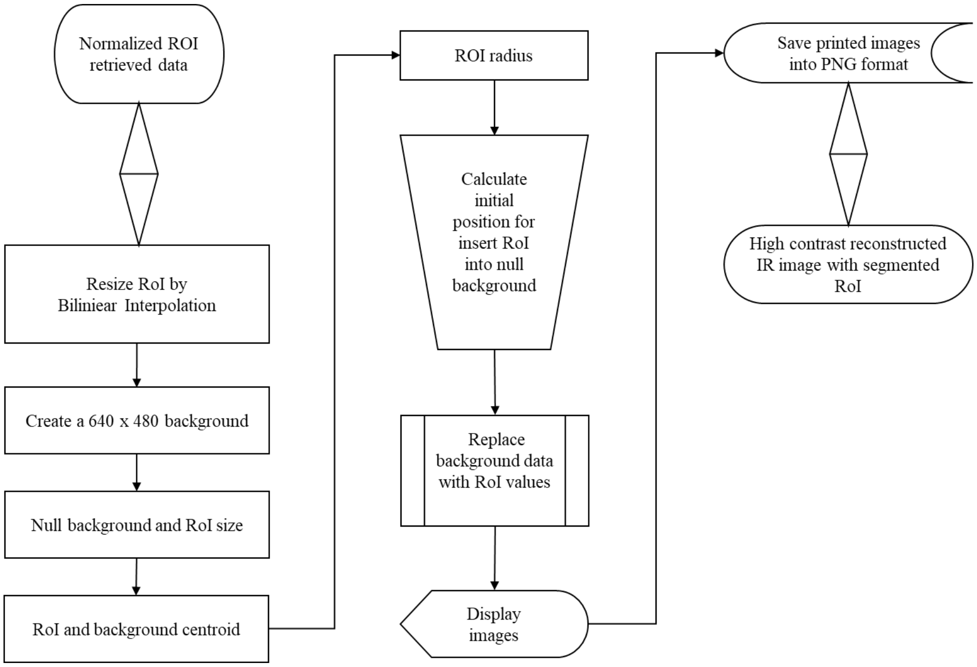

Figure 54: Image reconstruction algorithm based on radiometric data previously processed.

3.5 Image Registration

Multimodal image registration is an essential step in a variety of medical image applications for exploiting complementary data seen in several modalities. Finding correct correspondences for images acquired in diverse modalities is difficult because the images do not have the same physical content [191]. Registration is a common procedure in Computer Vision that has applications in 3D object modeling, among other applications. The process of overlaying two or more images (or 3D surfaces) obtained from different views, at different times, or by separate sensors into a common reference coordinate system is referred to as registration. Multimodal registration is a specific scenario in which the data to be matched do not belong to the same modality. It is challenging to define a similarity measure quantifying the quality of the registration due to the different nature of the modalities involved. A wide number of multimodal registration systems have been proposed in a variety of sectors, including medical and archaeology, due to the enormous number of conceivable modality combinations and application fields [108,151,163].

3.5.1 Background Transparency

The automatic segmentation of false-color images is still a challenge due to the lack of features that could separate the objects from the image background. This problem can be solved by exploiting, for the registration, the radiometric images directly provided by the sensor instead of the image [156]. The segmented information can be fitted to an image in the visible spectrum, such that only the region of interest will contain the color map corresponding to the IR energy intensity recorded by the sensors. Although the accuracy of segmentation through radiometric information has not yet been reported, there have been some advances reporting the accuracy of multimodal image registration with manual segmentation [108]. Multimodal segmentation solves the problem of point cloud estimation by adding more features that are detectable in a scene in the visible spectrum, making multimodal fusion relevant for these purposes [157].

Considering that the background of the IR images is blue color, the color triplet RGB = (0,0,131) was searched in each pixel and replaced by the black value color triplet (Figure 55), i.e., RGB = (0,0,0), since the alpha mask described in Equation (25) will make only black pixels fully transparent. Therefore, after applying the alpha mask on all pixels, the output will be an image with a perfect segmented RoI and transparent background (the artifacts are not visible and treated).

$$img_{IR}(x,y) = a \cdot img_{IR-original}(x,y) + (1-\alpha) \cdot img_{black}(x,y), \text{ with a=1} \tag{25}$$

where $img_{IR}(x,y)$ is the IR image with transparent background, $img_{IR-original}(x,y)$ is the IR with a black background, $img_{black}(x,y)$ is the background base color, and a is the transparency factor $a \in [0,1]$.

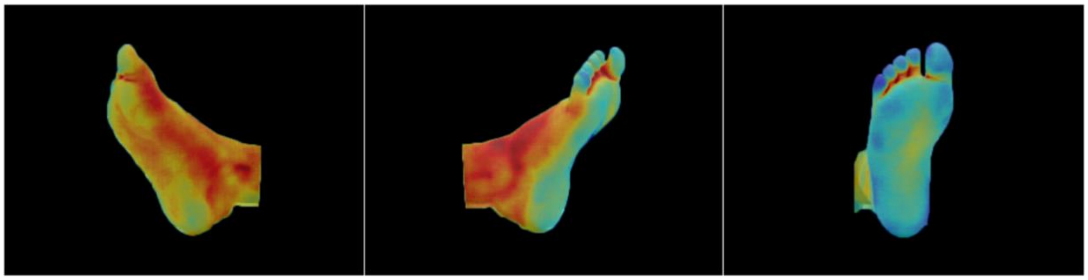

Figure 55: Segmented RoI with black background (scene). The following step is to clear the black pixels to get a transparent background.

3.5.2 Image Scale Transformation

The following treatment was performed to register the IR image (source image) with the visible-light image (target image). Since the thermal camera is equipped with two sensor arrays and dedicated optics, the foot can be captured simultaneously in the IR modality and the visible light modality. The main interest of visible light images is, that contrary to the IR images, these data contain natural texture and structure information, which can be used to extract feature points and descriptors. These features can lead to a robust and accurate surface reconstruction using an SfM approach. Thus, the estimation of the 3D surface of an object should exploit visible-light images, instead of using only IR images. Figure 56 describes the registration process between both modalities (IR and visible light images).

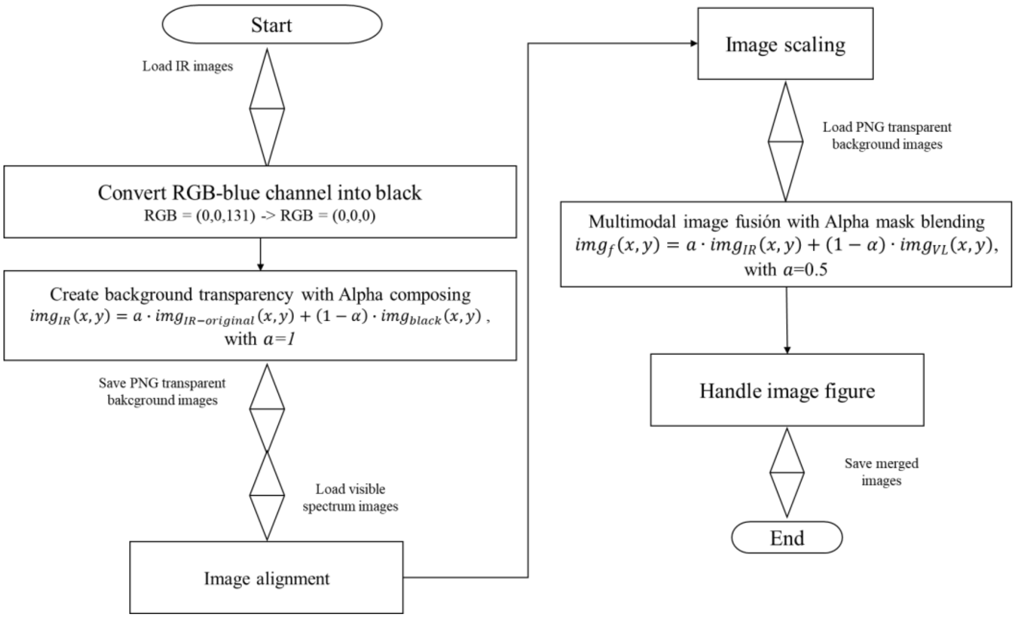

Figure 56: Flowchart of the multimodal registration. For each IR image, the blue background was transformed into black to apply the alpha mask transformation. The visible-light images were co-registered with the IR images by alignment, scaling, and merging.

The purpose of the processing described in Figure 56 is to align the data of the region of interest in the same original position after the segmentation process.

3.5.3 Image Alignment and Scaling

Once the RoI was retrieved with a transparent background, the following step was performed to register the source image (IR image) onto the visible-light target image. Image registration is the method of placing two datasets into a common coordinate system. The source and target images are monomodal data acquired at different times or were acquired by different sensors (multimodal data). In both cases, the images are acquired from different viewpoints.

An advantage of a bifocal system based on sensors fixed in approximatively the same position is that the scales of the images will be comparable. This is also the case for the thermal camera Ti32. The visible-light images were resized 1.25 times to match the resolution of the IR images (240 x 360 pixels). Then, the source images were cropped to rectangular images of 400 × 300 pixels since the image centers of the images of both modalities are superimposed (see Figure 57).

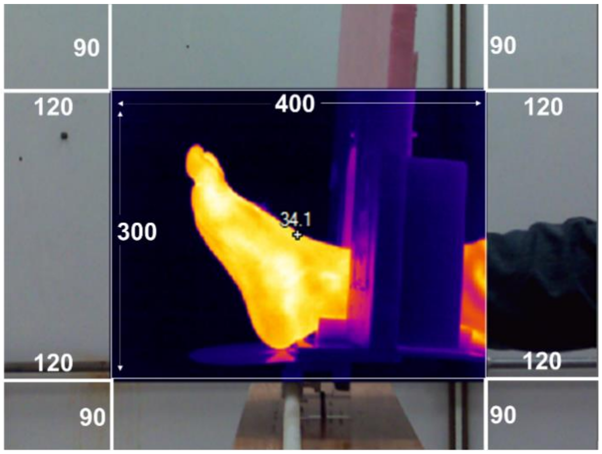

Figure 57: Multimodal superimposed images without RoI segmentation.

Figure 58 describes the multimodal image registration pipeline.

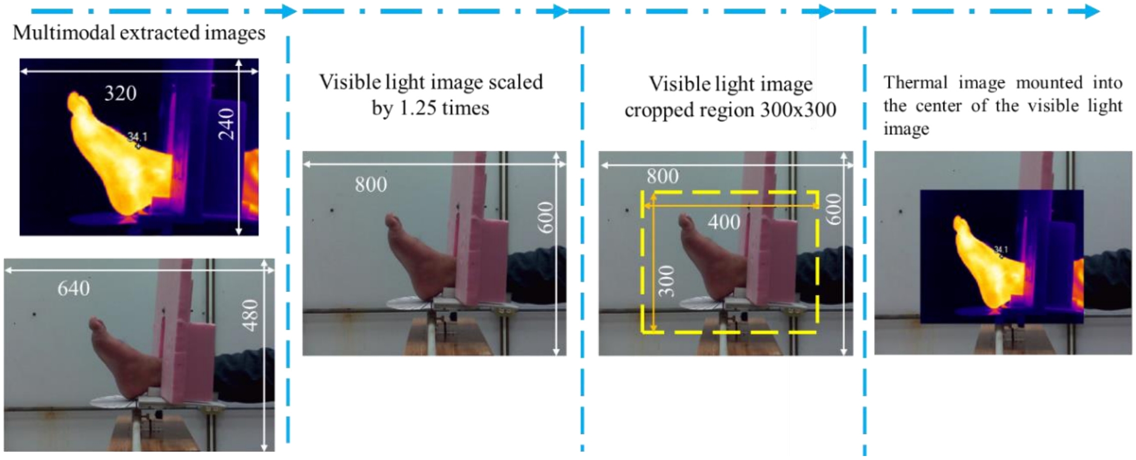

Figure 58: Multimodal (visible light and thermal) image registration. The visible-light image was cropped and scaled to fit the thermal image. In this way, it was possible to mount both images in the center of each image.

3.5.4 Image Saving

Once the images in both modalities were superimposed, they were saved in PNG format sequentially to be used in the 3D point estimation stage which will be explained in the next chapter. By providing regions of the visible light scene, it is possible to enhance the feature tranking and keypoints matching to obtain a 3D sparse point cloud. Exploiting only false-color images leads to a wrong approach since the 3D surface may be qualitatively wrong in the best case, or not generate any point cloud in the worst case.

3.6 Conclusions

The advantage of exploiting radiometric information that can be extracted from images of thermal cameras equipped with a microbolometer array was highlighted in this chapter, which is one of the main contributions of this thesis.

Indeed, it is worth noticing that the methods used in this chapter are rather classical digital image processing algorithms, notably in terms of interference removal and segmentation. However, to automate the procedure, contrast enhancement and temperature uniformity of the array data have an advantage over traditional approaches stated (e.g. manual segmentation for thermal images). Furthermore, due to the nature of the original data source, contrast enhancement in an RoI is a task that can only be accomplished using radiometry processing. Furthermore, no database is required to train shape recognition-based segmentation algorithms. The fundamental drawback of this method is that it was conceived for particular acquisition conditions, (a strictly controlled environment in terms of inference protection and object/background contrasts). Under specific conditions, large areas of thermal interference can appear and induce a failure of the automatic RoI segmentation, despite the algorithm's robustness. This is why it was suggested to maintain a controlled environment to enhance the image acquisition

For the multimodal image fusion step, robust approaches for point matching have yet to be investigated. The use of multimodal sensor equipment in this thesis represented an advantage because the images were only rescaled and translated. However, because such equipment (the Fluke Ti32 thermal camera) is specialized and designed to high-quality standards, it can be an economic disadvantage.

Chapter 4

Foot Surface Reconstruction, Texturing and Temperature Correlation

Contents

Given a sequence of images of an object or a scene, the purpose of an image-based 3D reconstruction algorithm is to estimate the most likely 3D shape (or surface) based on observed materials, perspectives, and lighting settings. The challenge is highlighted by the assumption that materials, perspectives, and lighting are all well recognized. If this information is undetermined, the task is often unsolvable, as numerous combinations of geometry, materials, views, and lighting can yield identical images such as the case of exploiting only false-color images. However, under a set of additional assumptions or information, state-of-the-art techniques can produce highly detailed reconstructions even from millions of images. Several information can be used to reconstruct a 3D surface from a set of images such as texture, defocus, shading, contours, and stereo correspondence. The latter three have been highly effective, with stereo correspondence being the most robust and having the greatest implementations.

This chapter presents the methods employed for the reconstruction of the 3D surface of the foot and the assignment of the thermal information to the sidebar in the display of the 3D model. It is important to emphasize that, at this point, the input data will be the superimposed multimodal images (thermal and visible spectrum images). These images will be processed by the detection of descriptive features (i.e. SIFT), the matching of key points, the generation of a 3D point cloud, the generation of a dense point cloud, and finally the reconstruction of a 3D surface and texture.

4.1 Multimodal Image for Surface Reconstruction

This chapter describes the treatment chain required for achieving a 3D model of the foot from a collection of fused multimodal images. The approach described in this chapter exploits multimodal images to represent a 3D foot surface. The visible-light images are used to reconstruct the 3D shape of the foot since in this modality feature points and vectors associated with a matching technique allow to reconstruct of the surfaces. On the other hand, the false colors representing IR values were superimposed only on the foot region. This section starts with the presentation of the different tests made to tend toward the final solution.

First, it was tried to directly use IR data in the SfM method. Thus, the extraction of descriptive key-point features from false-color images was the initial challenge. The low resolution of the LWIR Lepton 3.5 sensor was a major restriction for the project, as stated in Chapter 3. SIFT features, which are classically used by SfM approaches, were impossible to be extracted in an appropriate amount. The radiometric data were converted into false color values using several color scales (grayscale, rainbow or JET, sepia scale, etc.). However, no false color representation was appropriate since the extracted feature amount was systematically too low. Consequently, the Ti32 thermal camera was chosen because of its smaller pixel size. The comparison of images acquired with the two sensors can be visually done in Figure 59.

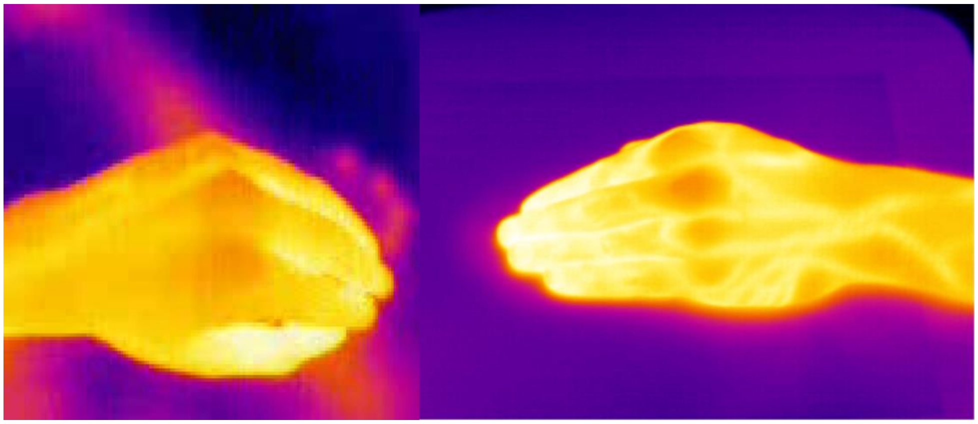
a) b)

Figure 59: Thermal images of a hand, a) LWIR Lepton 3.5 thermal image, b) Ti32 thermal image.

In Figure 60 b) it is possible to observe that some edges are visually identifiable. These, and especially corner points, allowed the extraction of features vector and the matching of the corresponding key points. This extraction led to preliminary surface reconstructions, as shown in Figure 61.

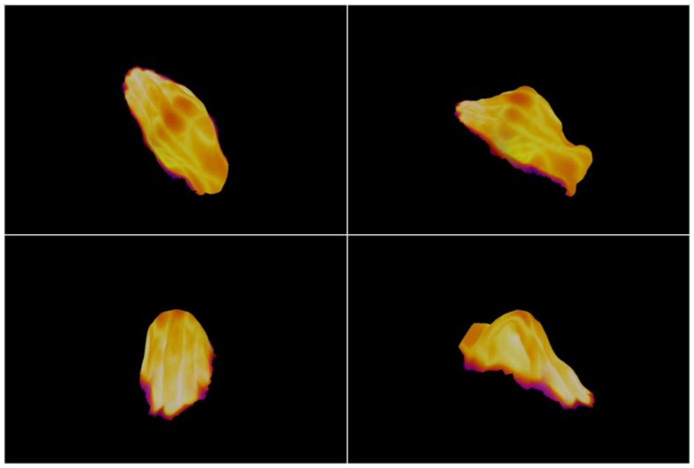

Figure 60: only false-color images with an "iron" color palette were used in the first preliminary reconstruction (yellow corresponds to the hottest regions while the coldest regions are in purple).

As with the Lepton 3.5 sensor, an attempt was made to reconstruct the surfaces by modifying the color palette of the color rainbow scale, also known as the Jet scale, the aim of these modifications being to maximize the number of point correspondences and to accurately reconstruct the objects. Figure 61 allows us to compare the number of successful point matchings obtained with the Jet color palette and grayscale scale palette. Also, with the Jet scale values (Figure 61 b)), more correspondences can be found than for the grey-level values (Figure 61 a)). Figure 61 highlights that the reconstruction of the hand surface is not qualitative and precise. The model is based on 25 images acquired from an arc trajectory around a hand.

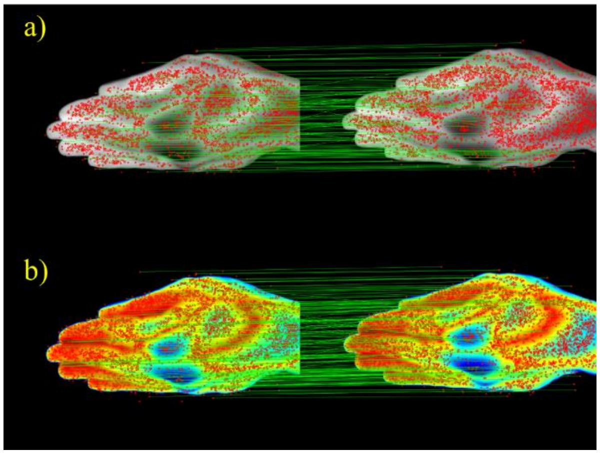

Figure 61: a) Point correspondences (represented by green lines) obtained for a pair of consecutive images encoded by grayscale values, b) Correspondence representation for the same pair of images whose pixel values are given in the Jet scale palette, where there are more accurate matching vectors.

Figure 62: Preliminary 3D reconstruction result.

Although the reconstruction in Figure 62 seems satisfactory, the 3D model is not qualitatively accurate enough. One reason which limits the 3D surface accuracy lies in the lack of precision in the matching step. The point correspondences should ideally be completely horizontal between the two consecutive images with minimum change in camera displacement. That might be due to the fact in the IR modality there is less contrast and structure/texture information than in white light images for which SIFT was initially designed. The smaller number of matches of homologous points, and the smaller location accuracy of feature points explain probably why the following SfM and MVS (Multiview stereo step) led to less precise surfaces. In a collection of primarily false-color images, it is a significant limitation. Therefore, similarly to the work of several other authors, it was decided in this thesis to make use of multimodal fusion to increase the amount of image information which should lead to an accurate feature matching (i.e., the surface reconstruction could be improved when the visible light scene is jointly used with IR images).

4.2 3D Sparse Cloud Estimation

One of the main goals of computer vision is to use images to recover the 3D structure of a scene. The joint use of images for the reconstructed of a stationary scene is a particularly successful method of construction of sparse point clouds. Several contributions (notably [198]) provide a comprehensive and in-depth overview of this massive collection of research

Bundle adjustment strategies, which aim to maximize a cost function defined by a total reprojection error (average of the distances between the 2D point positions and the reprojections of the reconstructed 3D points into the images), are commonly used to handle the multiview SfM problem in modern approaches. The goal of this cost function is to simultaneously adjust the structure (3D coordinates of scene points) and calibration parameters of each of the *n* cameras) to minimize the disparity between image measurements (extracted 2D points used for the reconstruction) and the positions of the reconstructed 3D points which are reprojected in the *n* images of a stationary scene [145,175].

SfM is the technique of reconstructing a three-dimensional structure from projections into a series of images acquired from multiple viewpoints. A sequential processing pipeline containing an iterative reconstruction component is known as incremental SfM.

Feature extraction and matching keypoints are the first steps in which the correspondences between images belonging to the same scene are obtained. This step is followed by geometric verification aimed at verifying those pairs that are considered a potential match, given that in the previous stages there is no guarantee that the matching is correct since they are based on appearance features. The generated scene structure is used to initialize the sparse point cloud with a two-view reconstruction method, before incrementally registering, with the growing surface, additional 3D points extracted from the images containing numerous feature points. At each iteration, the 2D points are triangulated with 2D key points of other points which were already reconstructed, the outliers are filtered (Figure 63). After a given number of iterations (i.e., images) the 3D surface under construction is refined using bundle adjustment (BA). The sections that follow go over the technique in further detail.

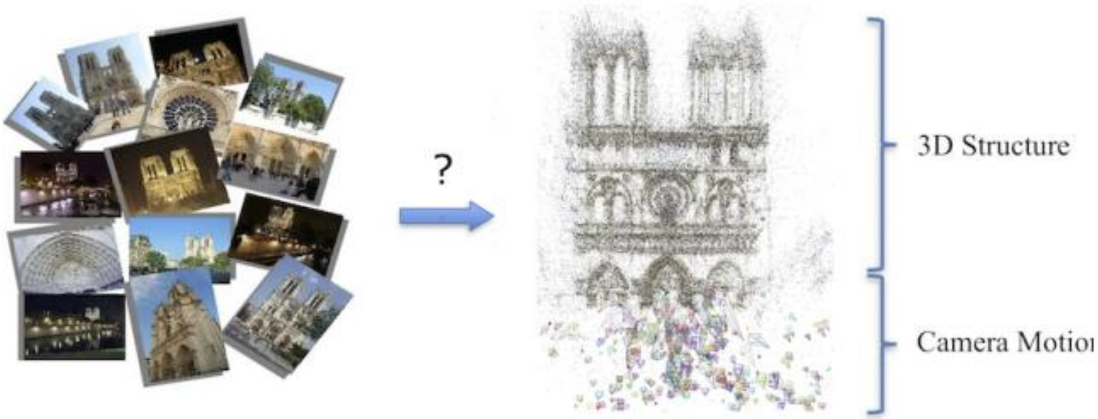

Figure 63: A goal of an SfM algorithm, in which the input is a set of images taken from different viewpoints, is to deliver a sparse point cloud, as well as the camera pose trajectory as output information. This image was taken from [175]

The 3D reconstruction accuracy of the SfM algorithm used in this contribution was assessed in [101,102] using a phantom with known dimensions and shape. This phantom was covered with paper sheets on which human skin images were printed to realistically simulate the texture of a healthy foot or a hand skin. The 3D surface of this skin textured phantom was reconstructed using the SfM algorithm. For a surface having the size of a foot, the mean distance between real and reconstructed point positions is systematically less than a millimeter. This 3D point reconstruction error is low enough to ensure an accurate shape reconstruction. It is fundamental in SfM methods to select two images linked accurately by a great number of successfully matched point pairs to initiate the SfM method (before the first iteration adds the points of the third image to the 3D point cloud) with an accurate two-view reconstruction (one of the two camera positions of these two first poses will act as a common coordinate subsystem of for 3D points). For an image pair, the relative position and orientation of the camera between two viewpoints are determined only with image information. The camera position of the first image serves as a reference and the extrinsic parameters link with the coordinate system of the second image. The 3D points are obtained based on the homologous points that are matched between a pair of images (in fact between an image and images whose 2D points were already reconstructed). Intrinsic and extrinsic parameters are commonly required to determine de 3D point cloud. These latter parameters are obtained through the calibration of the visible light camera exploiting a checkerboard on a flat surface. However, the SfM algorithm determines the optimal intrinsic and extrinsic parameter values, in such a way that calibration was not required for our purpose.

4.2.1 Scale-Invariant Features Transform (SIFT)

In the field of computer vision, 3D reconstruction is a classic challenge. People are increasingly in need of 3D models, such as for medical applications, as information technology advances. The basis of reconstruction based on image sequences is the ability to extract and match feature points accurately and stably, which is a fundamental stage in 3D reconstruction. SIFT is a reliable feature detection and matching approach [199]. The SIFT method processes the information and extracts a list of descriptors. SIFT descriptors have also been shown to be invariant to a wide range of image alterations, including moderate changes in viewpoint, noise, blur, contrast shifts, and scene distortion while remaining discriminative enough for matching. The SIFT technique is formed by two subsequent tasks: detecting interest points (keypoints) and extracting a descriptor for each of them. These descriptors are commonly used to match pairs of images since they are robust. Other popular applications include object identification and video stabilization [200].

Local features are used to decide if each point of interest should be selected as a key point used for the matching step. The local futures are specific structures of an image [201]:

- Corners are the intersection of two edges with different orientations or a point with two different edge directions in its neighborhood.
- Edges correspond to a boundary between two regions denoted by color intensity. Edge detectors are usually achieved by detecting grey-level transition limits.
- A blob is a region with textures associated with a bright area in a dark background. This region differs in properties like brightness or color compared to the background or scene.

A robust method for detecting features and matching method is Scale-Invariant Feature Transform (SIFT) [202]. The SIFT algorithm is used to detect and describe local features. The detected features (keypoints) are retrieved as quantitative data known as descriptors. The key points are independent of image rotations, scale changes, affine transformations, intensity variations, and viewpoint changes.

The SIFT algorithm consists of four steps [204]: First, the detection of grey-level extrema is searched in a scale space given in the form of a Difference of Gaussian (DoG) image pyramid. It generates progressively blurred images, then resizes the original image by half. The mathematical operator (Equation (26)) is defined as the convolution of the Gaussian operator and the image.

$$L(x, y, \sigma) = G(x, y, \sigma) * I(x, y) \tag{26}$$

where * is the convolution operator. $G(x, y, \sigma)$ is the Gaussian of the invariant scale. $I(x, y)$ is the input image (as a two-dimensional function). Figure 64 illustrates the blurred images when the Gaussian operator increases.

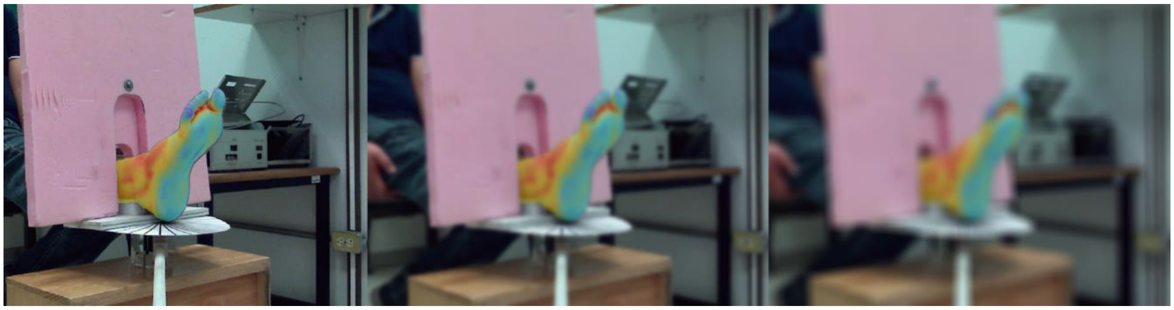

a) b) c)

Figure 64: Gaussian filter, a) original image, b) blurred image with a standard deviation of 3, c) blurred image with a standard deviation of 5. This technique is frequently used for simulating the loss of focus due to the distance between the object and the focal length.

The second step is to determine the corners and the keypoint by discarding the features with low contrast. Figure 65 depicts the concept.

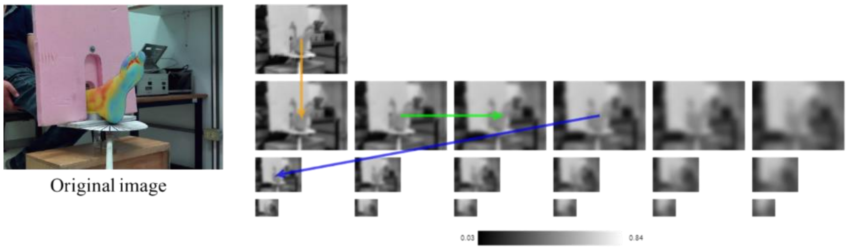

Figure 65: The original image remains intact. The first gray image is blurred by a Gaussian convolution, as indicated by the orange arrow. Sequential images are convolutions with increasing standard deviation. Each rightmost image is the result of the convolution of its left neighbor, as indicated by the green arrow. Finally, the image at the end of each row is down-sampled (see blue arrow). This starts another row of convolutions. This process is repeated until the images are too small to continue.

Images that have the same size but on a different scale are called octaves. The difference of Gaussian (DoG) is a technique for locating the extreme of the scale-space $D(x, y, \sigma)$ by calculating the difference between two images, one with a scale of k times the other (Equation (27)), Figure 66 shows the octave DoG.

$$D(x, y, \sigma) = L(x, y, k_i\sigma) - L(x, y, k_j\sigma) \tag{27}$$

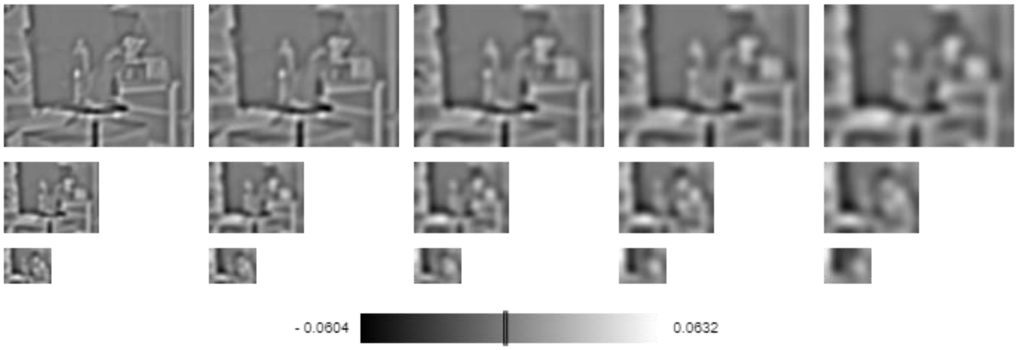

Figure 66: Each octave of our scale space is a space with three dimensions L(x,y,σ) and each row is the Gaussian difference discrete approximation of this space.

In some cases, the image resolution is not enough to find stable key points, i.e., at the same location in multiple images under multiple conditions. Given this problem, Lowe et al. proposed the second-order Taylor expansion of the octave DoG to better locate each key point (Equation (28)). Figure 67 depicts the result with the latter image examples.

$$D(\vec{x}) = D + \frac{\partial D^T}{\partial \vec{x}} x + \frac{1}{2} \vec{x}^T \frac{\partial^2 D}{\partial \vec{x}^2} \tag{28}$$

where $\vec{x}$ is the vector $(x, y, \sigma)^T$ corresponding to the pixel location of the candidate keypoint, $D(\vec{x})$ is the second order Taylor expansion to locate candidate points and D is the Gaussian difference.

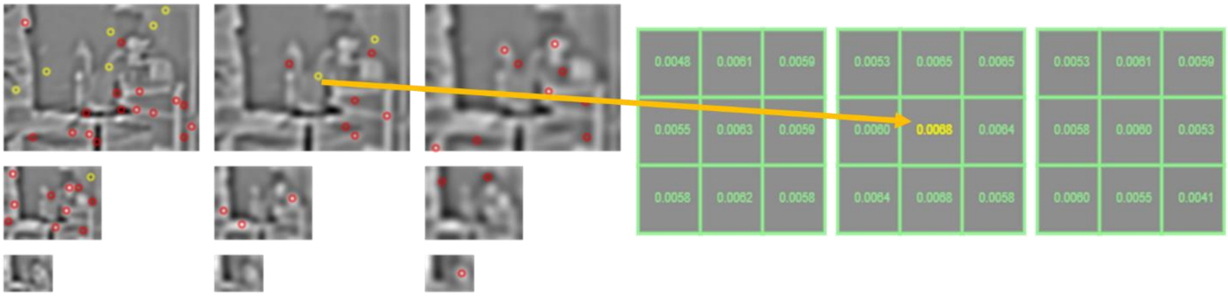

0.0048	0.0061	0.0059	0.0053	0.0065	0.0065	0.0053	0.0061	0.0059
0.0055	0.0063	0.0059	0.0060	0.0068	0.0064	0.0058	0.0060	0.0053
0.0058	0.0062	0.0058	0.0064	0.0068	0.0058	0.0060	0.0055	0.0041

Figure 67: the red dots are Keypoints while the yellow dots are also Keypoints but are almost homogeneous values. The red value in the center corresponds to the keypoint located on the left eye.

The values of the yellow dots recall that these points may be a candidate for being a region invariant to scale, which means that can be used to track the next image even if it was taken from a different point of view or even a different sensor. Then, the coordinates of each located keypoint must be refined. To eliminate points that could be false, the algorithm implements the Hessian matrix to find local maxima and minima. Given a point $p = (x, y)$ in an image I, the Hessian matrix $H(p, \sigma)$ at point p with scale σ is defined in Equation (29).

$$H(p,\sigma) = \begin{bmatrix} D_{xx}(p,\sigma) & D_{xy}(p,\sigma) \\ D_{yx}(p,\sigma) & D_{yy}(p,\sigma) \end{bmatrix} = \begin{bmatrix} \frac{\partial^2 D}{\partial x^2}(x,y,\sigma) & \frac{\partial^2 D}{\partial x \partial y}(x,y,\sigma) \\ \frac{\partial^2 D}{\partial y \partial x}(x,y,\sigma) & \frac{\partial^2 D}{\partial y^2}(x,y,\sigma) \end{bmatrix} \tag{29}$$

Then, it is obtained the determinant of $D_H = |H(p, \sigma)|$ and evaluated for (0,0), (1,0), (0,1) and (1,1). The following conditions are used to determine which points should not be considered key points. Figure 68 depicts the elimination of key points.

- If D_H>0, the point (x,y) is a local maximum, it is a candidate for being a blob.
- If D_H<0, the point (x,y) is a local minimum, and the point is rejected for being a blob.
- If D_H is undefined, (x,y) is an inflection point.

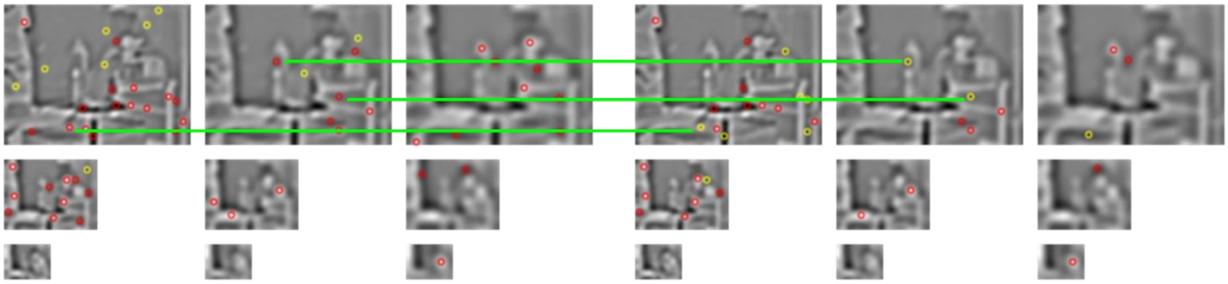

Figure 68: several key points were eliminated due to their correspondence as an undefined condition.

To determine the estimated orientation for a point of interest, a circular histogram of gradient directions is accumulated over a neighborhood around the point of interest. For each point of interest, a reference orientation will be assigned. The point is to observe if there are more gradients around the neighborhood around the point of interest to compute if they have also the same direction. The approximation is computed based on finite difference, in which the result will indicate the direction of the greatest increment and the slope magnitude. The circular histogram will be divided in an interval from 0 to 360 degrees fixed to 36 bins [200]. The gradient direction is defined by the magnitude times a Gaussian weight. If the value of this histogram's extrema exceeds a particular threshold, they are detected and chosen. The best approximation of the orientation is obtained by the quadratic interpolation of the bins. Figure 69 illustrates the orientation with the latter example.

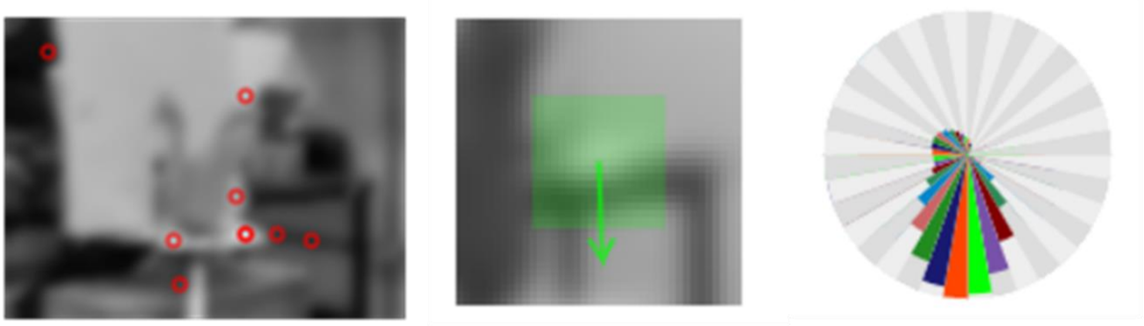

Figure 69: The gradient points in the direction of the largest increment and its magnitude is the slope in that direction.

The example presented above resumes briefly how SIFT method for detect blobs (keypoints) ins a single image. These key points are used later for finding corresponding vectors between two consecutive images. To summarize, key points are extracted at a variety of scales and blur levels, with all subsequent computations taking place within the scale-space framework. The descriptors will be invariant to image scaling and tiny changes in perspective. The descriptors should be invariant to the rotation if they are computed concerning a reference orientation. Similarly, descriptor information is retrieved according to the key point position and is hence translation invariant. If they are considered unstable or difficult to find precisely, several prospective important points are rejected. As a result, the remaining crucial points should be largely noise-free.

The first process in SfM lies in a robust and accurate point correspondence determination, which searches for the 2D projections of the same 3D in two images acquired from two viewpoints. Such points are called homologous points (or key points) which are seen in two images including common scene parts. Let the input images be $\mathcal{I}$, where $\mathcal{I} = \{I_i \mid i = 1 \ldots N_I\}$.

For each single image I_i, SfM finds a cluster of local features at certain regions in each image using a feature descriptor, which should be invariant by geometrical changes such as scale. In terms of robustness, SIFT, constitute the gold standard [169,200]. Let the local features detected by SfM be denoted by $\mathcal{F}_i = \left(x_j, f_j\right),\ j = 1 \ldots N_{F_i}$, and the regions where features are detected are denoted by x_j which contains a descriptor f_j.

The computed descriptors $\mathcal{F}_i$ are the input data for the following stage, which is the matching keypoints between a pair of images.

4.2.2 Correspondance of Homologous Points

SfM determines the group of images that belongs to the same scene region, based on the detected keypoints $\mathcal{F}_i$. These detected keypoints are compared to find homologous keypoints between two images I_a and I_b. The result is a set of groups of possibly overlapping images pairs denoted by $\bar{C}$ and the feature correspondences that link the images of each group visualizing a common region. SfM uses the features $\mathcal{F}_i$ as an "appearance description of a small image that contains the same scene part. The overlapping images are denoted by $\bar{C} = \{(I_a, I_b) \mid I_a, I_b \in \mathcal{I}, a < b\}$where images I_a and I_b belongs to the set $\mathcal{I}$ and the descriptors are compared regard to I_a. These set of overlapping images are preliminary outputs based on optical features. Therefore, it is required to perform a geometrical verification. The matching process is detailed in Figure 70. The preliminary correspondences (i.e., obtained for a false-color image) can be observed in Figure 71, which gives an example of keypoint matching on two consecutive images.

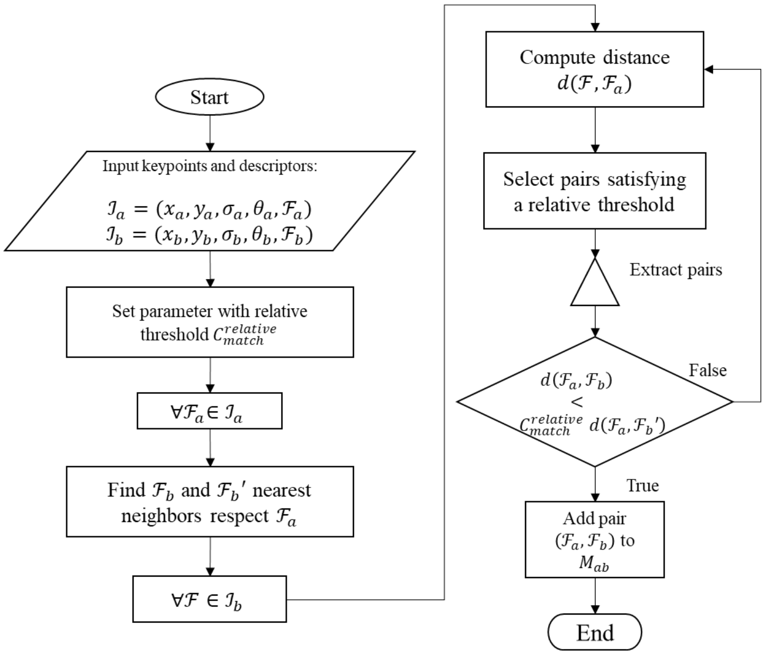

Figure 70: Algorithm for matching key points, which consists of pair key points correspondences and verifying the reliability.

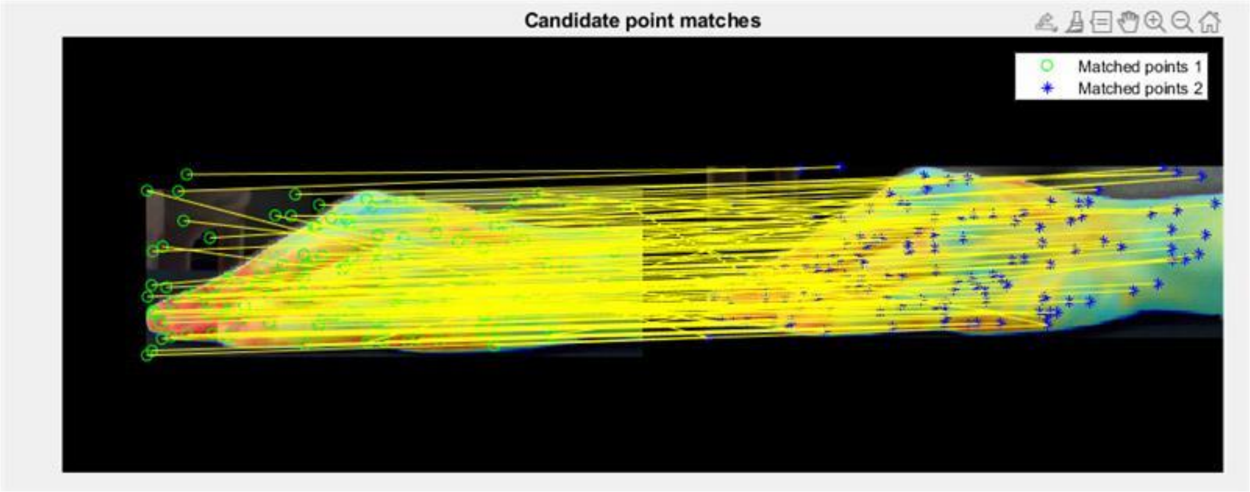

Figure 71: Two images in which the green circles and blue dots represent key points, and the yellow lines represent the correspondence between feature points.

4.2.3 Geometric Verification

The output of the latter step is a set of overlapping images $\bar{C}$ and their future correspondences denoted by $M_{ab} \in \mathcal{F}_a \times \mathcal{F}_b$.

Because the first correspondence search is simply based on relative feature similarity (appearance), matched feature points may not always link true homologous points at the same scene point. For this reason, SfM methods must verify the accuracy of matched points. Therefore, SfM carries out a geometric verification exploiting the set of matched keypoint between image pairs. The geometric verification uses. different mathematical models to define the geometric relationship between image pairs. The transformation of a fully rotating or shifting camera capturing planar scene parts is defined by homography matrix H. The essential matrix E (which can be calibrated or determined using solely the image data) or the fundamental matrix F (uncalibrated) define the relationship between two camera positions.

Consider a vector as (x_w, Y_w, Z_w) of a point in 3D world-view space. As shown in Equation (30), we may map this 3D point to a point in other 3D coordinate system.

$$\begin{bmatrix} x_a \\ y_a \\ z_a \end{bmatrix} = C_{int} C_{ext} \begin{bmatrix} X_w \\ Y_w \\ Z_w \\ 1 \end{bmatrix} \tag{30}$$

where C_{int} and C_{ext} are the intrinsic and extrinsic parameters of the camera and (x_a, y_a, z_a) is a point in another 3D coordinate system. This point can be projected onto an image plane using Equation (31).

$$\begin{bmatrix} x_a \\ y_a \\ 1 \end{bmatrix} = \frac{1}{z_a} \begin{bmatrix} x_a \\ y_a \\ z_a \end{bmatrix} \tag{31}$$

Once a point in arbitrary space is found, it may simply scale its coordinates to obtain 2D coordinates in image space. The intrinsic matrix transforms 3D point coordinates into 2D homogenous image coordinates. The ideal pinhole camera is used to model this viewpoint projection.

Consider a camera with a focal length of f, a sensor size of (x_s, y_s) commonly in μm, and a captured image width and height of (w, h) in pixels. Consider the optical center of the camera as (o_x, o_y),k. The intrinsic matrix C_{int} is given by Equation (32).

$$C_{int} = \begin{bmatrix} \frac{fw}{xs} & 0 & o_x \\ 0 & \frac{fh}{ys} & o_y \\ 0 & 0 & 1 \end{bmatrix} \tag{32}$$

C_{ext}, on the other hand, is formed by two matrices: a rotation matrix R and a translation vector T, as shown in Equation (33).

$$C_{ext} = [C \mid T] = \begin{bmatrix} r_{11} & r_{12} & r_{13} & T_x \\ r_{21} & r_{22} & r_{23} & T_y \\ r_{31} & r_{32} & r_{33} & T_z \end{bmatrix} \tag{33}$$

The translation vector T is given by $(T_x, T_y, T_z)^T$, where this tuple indicates the space coordinates. For example, in a particular situation where the camera has no x or y translation, it can be considered $T_x = T_y = 0$ while T_z can be equated to the camera position regarding the ground in mm. Equation (34) represents the link between a 3D-view point and an arbitrary space

$$C_{int}\, C_{ext} = \begin{bmatrix} \frac{fw}{xs} & 0 & {}^{w}\!/_{2} \\ 0 & \frac{fh}{ys} & h/2 \\ 0 & 0 & 1 \end{bmatrix} \begin{bmatrix} r_{11} & r_{12} & r_{13} & T_x \\ r_{21} & r_{22} & r_{23} & T_y \\ r_{31} & r_{32} & r_{33} & T_z \end{bmatrix} \tag{34}$$

Epipolar geometry is related to the projective geometry of two cameras (or of a moving camera) which observe a scene point from two viewpoints. It is independent of the scene content (planar surfaces or not) and is completely defined by the intrinsic (optical parameters) and extrinsic (displacement between two viewpoints) parameters of the camera. Fundamental matrix F can be determined with the information of two images. If a 3D point $\boldsymbol{X}$ is projected on 2D position x in the first view and x' is the projection in the second image, then these image points fulfill the relation $x'^T F x = 0$, where F is the fundamental matrix. When two sensors capture the same scene from different perspectives, the relationship between the two viewpoints is described by the epipolar geometry. The search for corresponding points in stereo imaging is frequently the motivation for exploiting the epipolar geometry properties [205]. The algebraic representation of epipolar geometry is the fundamental matrix. The fundamental matrix F is derived from the mapping between a point and its epipolar line, and the parameters of the matrix are then specified. Given a pair of images, the epipolar line l′ in the second image and the epipolar line l' that corresponds to each point x in the first image will be found. Any point x′ matching the point x in the second image must be on the epipolar line l′. The epipolar line is the projection of the ray from point x through the camera center C of the first camera in the second image. As a result, a link x → l′ exists between a point in one image and its matching epipolar line in the other image. This mapping turns out to be a single correlation, or a projective mapping from points to lines, which is represented by the fundamental matrix F.

Consider a plane π that does not intersect the camera centers (see Figure 72). The ray passing through the optical center of the first camera (point x), intersects and reaches the plane π at point **X**. In the second image, 3D point **X** is projected to a point x′ and passes through the optical center of the second camera. Because **X** is on the ray that passes through x, the projected point x′ must be on the epipolar line l′ projected in the same ray in the right image. Both the points x and x′ are projections of the 3D point **X** on a plane. Because they are both rays projected to the same plane through the planar point set $\mathbf{X}_i$, the set of all such points x_i in the first image and the corresponding points x′ in the second image are projectively identical. Thus, there is a 2D homography H_π which maps the point x_i to x′. The fundamental matrix F may be written as in Equation (35).

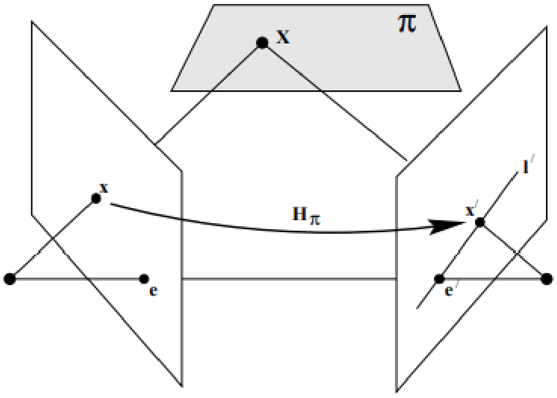

Figure 72: A point x in the first image (left image) is linked to a matching point x′ in the second image (right image) through the homography H_π, linking x′ to the epipole e′ yields the epipolar line via x′. The image was taken from [205].

$$F = [e'] \times H_\pi \tag{35}$$

where H_π is the displaces a point x from one image plane to its corresponding point in the image on the other image plane. The epipole $[e']_\times$ vector is of rank 2 and H is a rank 3 matrix, therefore, F is a matrix of rank 2.

A homography describes a complete geometrical transformation between the pixel coordinates of two images. The fundamental matrix F describes the relationship for a moving camera and takes the epipolar geometry of an uncalibrated sensor into account The values of the fundamental are confirmed as geometrically exact when the transformation effectively links a significant number of homologous features of two images. Because feature matching methods also frequently deliver outliers in terms of correspondence, matching verification approaches such as RANSAC are essential [162].

The RANSAC algorithm is used given a data fitting problem. That is, to find a slope that best fits a set of scattered points. The parameter vector $\vec{x}$ will be estimated from N data from the total set of points M. Let P_g be the probability of a selected data set, assuming that it will be the best fitting model. Also, let P_f be the probability of failing, i.e. that algorithm exists without finding an acceptable fitting model. The algorithm starts by randomly selecting N data and performs the first estimation of the vector $\vec{x}$. Then, it finds the number of elements in the set M that were fitted to the vector $\vec{x}$, given a tolerance k. If k is large enough, the fitting model is accepted. Otherwise, the selection of N data is iterated L times by randomly fitting the model with the parameter vector $\vec{x}$. The value of k depends on the percentage of data estimated to belong to the sets that can be fit, i.e. it is the maximum number of iterations that the algorithm can repeat. The number of iterations L is defined by Equation (36).

$$L = \frac{\log(P_f)}{\log\left(1 - (P_g)^N\right)} \tag{36}$$

The output of this algorithm is a set of outliers, which previously the distance error was calculated to consider a valuable outlier. Figure 73 illustrates the result of the geometrical verification on a pair of images.

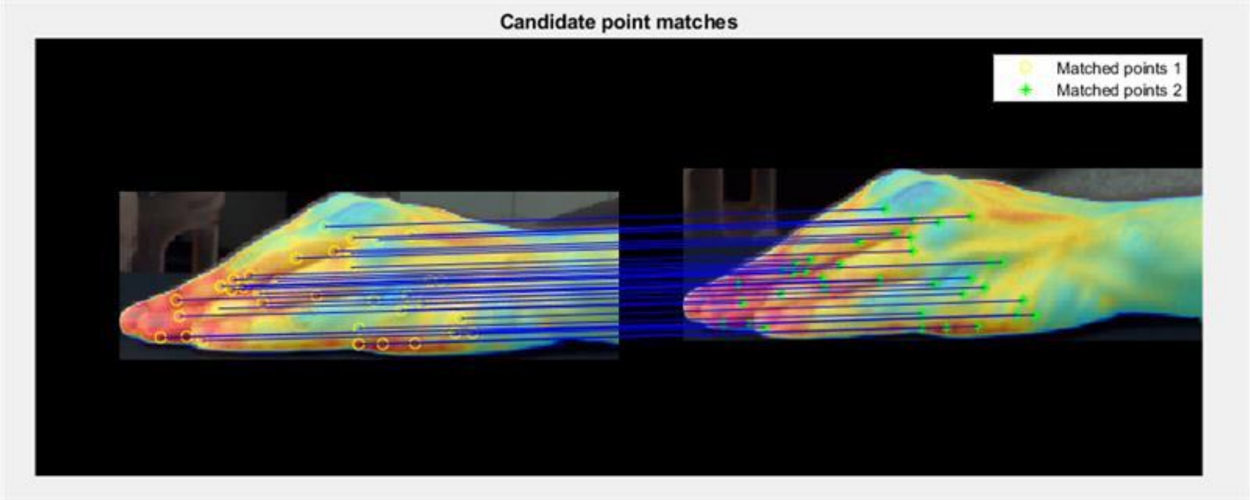

Figure 73: matching result (blue lines) after RANSAC outlier rejection method. A visual comparison with Figure 10 shows that numerous outliers were rejected.

The following steps are the initiation of incremental reconstruction, in which a refined set of matched key points is exploited to obtain a sparse 3D point cloud. At this point, the selection of the initial pair of images is essential, since the accuracy of the surface and performance of the reconstruction depend on the initial coordinates of the incremental process.

4.2.4 Image Registration

This stage is based on a Perspective-n-Point (PnP) problem when new images are registered to the previously computed model, in which feature correspondences are used to triangulate points that have been previously calculated in the previous stages. The PnP problem entails estimating the pose $P_{\bar{C}}$ (the orientation and position of a set of overlapping images $\bar{C}$), and the intrinsic parameters for uncalibrated cameras such as the case of this thesis.

The estimated pose for registered images $\boldsymbol{P}$ is a set of individual poses belonging to Rigid Body Motion, whose set of overlapping images are true $\boldsymbol{P} = \{P_{\bar{C}} \in SE(3) \mid \bar{c} = 1 \dots N_P\}$, For every new registered image, the estimated pose $\boldsymbol{P}$ will be extended by the individual pose $P_{\bar{C}}$. The correspondences computed between 2D images, and also the ones obtained for 3D images, maybe often be contaminated with wrong matched keypoints (outliers) [169]. To correct these errors in uncalibrated cameras, several approaches are employed such as minimal solvers or sampling-based algorithms presented in [207,208] respectively.

4.2.5 Triangulation

For each new registered image in the previous step, new points in the scene must be observed to provide information about the scene. The scene is reconstructed from a set of points, i.e. the 3D cloud of scattered points, denoted by $\boldsymbol{X} = \{X_k \in \mathbb{R}^{\mathbf{3}} \mid k = \mathbf{1} \dots N_{\boldsymbol{x}}\}$**,** where X_k is a point of the sparse cloud. The point X_k will be triangulated and added to the scattered points $\boldsymbol{X}$**.**

This step is fundamental because the stability is increased through redundancy providing additional correspondences (images that repeatedly belong to the same scene but with a different perspective). Commonly, this step requires high computational resources, therefore timing. However, efficient triangulation is presented in [169] based on RANSAC in which the points can be estimated within a wrong outlier.

4.2.6 Bundle Adjustment

Even if image registration and triangulation are separate steps, they are correlated, since triangulation can hence initial camera pose through redundancy while uncertainties of the camera pose lead to triangulated poses. However, without further correction, SfM may lead to a wrong structure or unsolvable reconstruction. Therefore, bundle adjustment is required, which task is to joint non-linear overlapped images $P_{\bar{C}}$ and 3D scene point X_k to minimize the projection error, given by Equation (37).

$$E = \sum_{j} \rho_j \left(\left\| \pi(P_{\bar{C}} X_k) - x_j \right\|_2^2 \right) \tag{37}$$

where π is the function that projects image keypoints into a 3D space and ρ_j is the loss function to remove possible wrong outliers. In other words, the position of a local feature on a 2D image is compared concerning a set of is a point of the sparse cloud with their respective overlapped image. According to Schonberger and Frahm [169], the employed method in SfM algorithm is based on Levenberg-Marquardt [177,209]. Bundle adjustment is based on the following steps.

The first step is to perform a parameterization, which consists in estimating potential outliers. Although there are several methods regard to the number of cameras, unordered internet image set, or complexity, the Cauchy function can be employed for this thesis as a robust loss function ρ_j for local bundle adjustment. However, some projections may not correspond to the model so filtering must be carried out. Post-processed images that may cause a model distortion are checked in this stage, which typically only have outliers observations but not projections. Camera poses with distortion or irregular field of view are filtered after a global bundle adjustment [169]. Drift effects may occur before performing a global bundle adjustment, therefore a triangulation must be carried out. This step consists in improving the sparse point cloud by tracking 3D points that failed due to an inaccurate pose before the triangulation stage. The projections error before the filtering step is tracked instead of increasing the triangulation threshold. Also, redundancy is increased to improve 3D points by merging tracks of previous discarded points. Lastly, since the first bundle adjustment can affect desired outliers, a second iteration may improve the results filtering by iterative optimization until the number of filtered observations is minimized.

4.3 Dense 3D Point Cloud

Multi-View stereo refers to a set of methods that exploits stereo correspondences to obtain a dense 3D point cloud. The algorithm assumes as input a 3D cloud point obtained by the SfM method, a set of images, and the camera parameters. Although different applications may apply different approaches, the main idea of MVS is still the same, obtain a dense 3D point cloud provided by the SfM stage. The reconstruction of the materials of the scene is optional (texturing) [178]. It is also noteworthy that the MVS algorithm result will be qualitatively acceptable to the quality of the input images and the camera parameters. Therefore, exploiting only false color images may be considered a wrong approach. Given a set of images (e.g. superimposed images of false color and visible light) as input, MVS will exploit stereo correspondences to increase the 3D point number, and eventually refine the camera poses.

The 3D dense point cloud generates each 3D point based on merging and splitting techniques on the set of images. The point cloud is expanded by spatial consistency assumption during the process of each image. In such a way, redundancy is increased. The model is based typically on three steps: initial feature matching, expansion, and filtering [178].

The initial feature matching step is referred to in Section 4.2.2, in which the goal is to detect corner features in each image based on the DoG operator. Consider a patch as ρ which is a local tangent plane approximation of a surface, and c(ρ) is the center geometry with normal vector unit n(ρ). Let be a pair of local features (f, f') where f is a detected feature of the image I and f' is a feature that lies within two pixels in the same epipolar line and is triangulated to a 3D point. The triangulation from f and f' is assigned to the center geometry c(ρ), and a patch optimization is carried out to refine the latter information.

The next step is the expansion, which consists in reconstructing patches in every image cell denoted by $C_i(x, y)$. These patches will be generated on empty spaces based on neighbor existing patches. The expansion will create a new patch ρ' for every collected image cell initializing a new normal vector n(ρ'). The new center geometry c(ρ') and normal vector will be then optimized by Normalized Cross-Correlation (NCC) method. This process is repeated until every patch is covered (or reconstructed).

However, filtering must the carried out since the expansion step may produce wrong patches, due to image consistency. To address this problem, two filtering steps are carried out. The first filter is based on visibility consistency, while the second stage will retrieve adjacent cells in the set of images removing them as an outlier when the neighbors of the patch ρ are lower than 0.25. The filtering algorithms are explained in detail in [178].

4.4 Surface Meshing and Texturing

At this point of the process, a dense 3D point cloud is generated. However, the model still is not considered as a surface. A meshed surface is built using the dense point cloud computed in the MVS stage. The meshed surface is often made up of triangular facets defined by three vertices corresponding here to 3D points of the dense point cloud. The meshed surface computation begins with a statistical outlier elimination that smooths the point cloud. The Poisson surface reconstruction technique then creates a mesh based on the surface normal of the facts and 3D point coordinates. A refinement stage that improves the representation of the meshed surface leads to the final surface [170,179,210].

Texture mapping is a crucial last step in the process of rendering 3D surfaces with consistent colors and structures. A precise superimposition of 2D image texture information onto the meshed surface is critical to perform visually consistent scene rendering; however, due to noise in the depth data, geometrical reconstruction errors of surface parts, substantial variation in the scale of the images in the video-sequence, image blur, exposure differences from one image to another, and occluded surface portions, texture mapping on meshed surfaces is a difficult step. Several techniques based on per-vertex colors have been developed to address this issue. Image registration is a typical approach, in which the pixel's correspondence between registered images aids the surface texturing process. This texturing method, combined with efficient SfM and MVS phases, resulted in the reconstruction of precise extended 3D surfaces with excellent texturing coherence. That is why, in this thesis, texturing techniques as those proposed in [180,211], are used to map the textures on extended

3D foot surfaces. Figure 74 depicts a surface reconstruction example carried out by an MSV technique based applied to a video sequence of images of a hand.

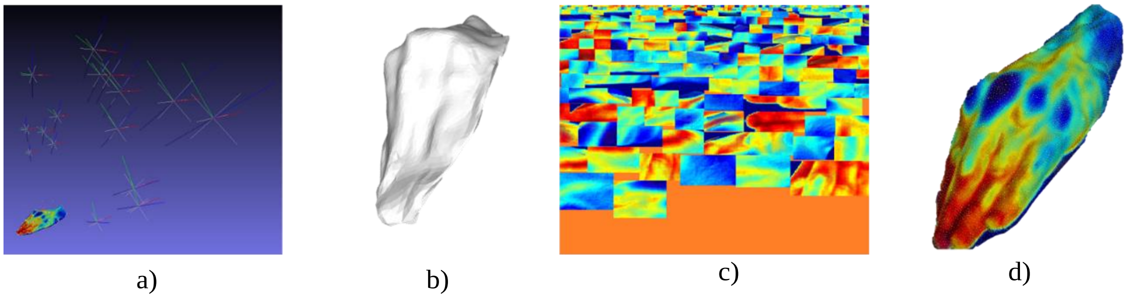

Figure 74: a) In the MVS stage, the camera trajectory is refined and a dense 3D point cloud is computed using the sparse cloud provided by the SfM method b) generation and refining of a mesh leading to a gapless surface of the hand, c) 2D sequence of false-color images that are employed as textures, d) texture mapping result on the surface using the known camera positions.

4.5 Colmap and Open-MVS Software

The generation of the sparse 3D point cloud was obtained using the COLMAP software, which is a set of algorithms to retrieve the point cloud and camera poses designed for visible light images. However, the input in this thesis was superimposed images where the temperature values were used to texture the surface. An advantage of the COLMAP software lies in the robustness and accuracy of its SfM implementation for the sparse point cloud reconstruction, even if the intrinsic camera parameters are unknown [174]. For our application, the exact scale of the surface is not relevant for the 3D foot representation. During the surface construction, the COLMAP software computes intrinsic camera parameters (notably the focal length and the radial camera distortion parameters), the 3D camera trajectory (the camera poses are given by the external camera parameters), and a sparse set of 3D points located on the surface of the objects. The parameter settings for COLMAP software are provided in Table 13.

Table 13. COLMAP parameters for feature detection, matching, and point cloud estimation.

Parameter	Value/Option
Camera model	Simple Radial
Guided Matching	Activated
Edge threshold	50
Peak threshold	0.00067

The first parameter is the simple radial camera model, which is suitable when there are different camera calibrations, or the parameters are unknown. This model is preferred since the images input are multimodal with different origins, and none of them was calibrated a priori. The second parameter is the activated guided matching, which is recommended for increasing the number of nearest neighbors or the overlap in sequential matching; if this option is selected as deactivated, the initial image pair should be manually chosen and set the images from the database to ensure enough correspondences. The third and fourth parameters are the edge and peak threshold, which refer to the SIFT detectors (Section 2.4.4), where the edge threshold eliminates peaks of the DoG space which yields wrong localized frames (small curvature) and the peak threshold eliminates (filters) small peaks of the DoG scale space. The sparse 3D point cloud and camera positions were imported into the Open-MVS libraries proposed by Cernea [171]. The dense point cloud delivered by the MVS stage is used to construct a mesh using the Poisson surface reconstruction method to retrieve a 3D surface model. The input for this MVS-process consists of the camera poses and the point cloud obtained in the SfM-step. This pipeline ends with the projection of the image textures onto the meshed surface.

4.6 Thermal Data Correlation

One of the objectives of this work lies in displaying, in an interactive way, the 3D surface with temperature information. The 3D model provided by the reconstruction stage with MVS has a PYL format (Polygon File Format) with a texture map in PNG format. Thus, as a proof of concept, MATLAB (MathWorks Inc., Natick, MA, USA) was an appropriate option for displaying the results along a color bar relating to the temperature information extracted from the radiometric arrays.

The first task was to convert the PYL model into an OBJ format so that the triangulated mesh could be imported into MATLAB. The transformation was carried out employing the code proposed by Abayowa [212], which converts vertices, faces, and texture information coded in a specified OBJ file. The displayed model can be seen from any viewpoint, i.e., rotations and scale transformations can be performed, while a color sidebar, indicates the relationship between the colors and the temperature values. The mapped colors of each IR image are scaled depending on the hottest point. Figure 75 describes the latter characteristic of the IR thermography technique, which is a disadvantage under uncontrolled background conditions causing thermal interferences. However, due to this property, only the maximum and minimum temperature values contained inside the region of the foot were considered as a reference for adjusting the parameters in the color sidebar. The values are scaled into red color tones being for the highest temperature and blue tones for the minimum temperature.

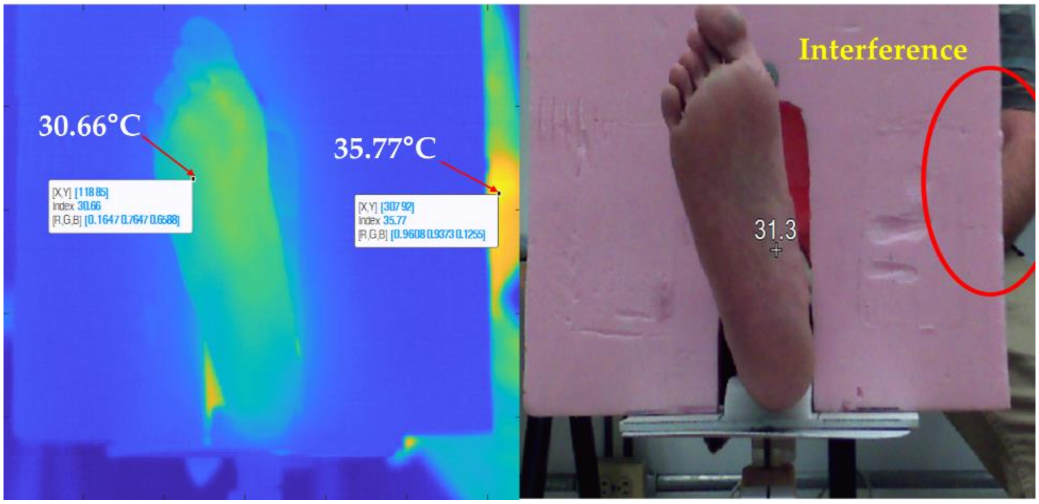

(a) (b)

Figure 75. Color contrast mapping according to the warmest spot on volunteer 1 (a sitting position in which the upper limb is partially captured on the right side of the image). (a) The hottest spot of the picture frame is located on the upper limb, which decreases the color contrast of the foot image. (b) The image was acquired by a wrongly aligned camera since the foam background should completely cover the volunteer body.

The color sidebar can be configured with numerical limits, which are represented as a two-element vector of the type, i.e., minimum and maximum values, with all values in between being translated to the colormap intermediate rows. As a result, the entire set of data must be analyzed to determine the highest and lowest temperatures. The segmentation technique can be used to locate all the values that differ from the background (i.e., zero). In this approach, each of the coordinates of the values of interest associated with the model can be determined. Due to systematic mistakes in the acquisition process, each region of interest has a varied size and intensity in the same region between two different temperature matrices At this point, the temperature retrieved from the foot is not considered as a matrix, but as a vector with temperature values in which the size of the vector differs from the following captured image.

A challenge in associating the temperature with the model was to analyze the radiometric data that only belong to the RoI and discard the background values. Therefore, the structured data were built with non-background values in which every coordinate was retrieved regarding the original temperature matrix. However, each RoI has a different size and temperature value from one array to another (i.e., from one viewpoint to another). An approach to solve this problem was to retrieve the minimum and maximum limits for each thermal array. Then, the average of the limits was calculated and assigned to the sidebar scale data input and represented by the Jet colormap. Figure 76 summarizes the procedure.

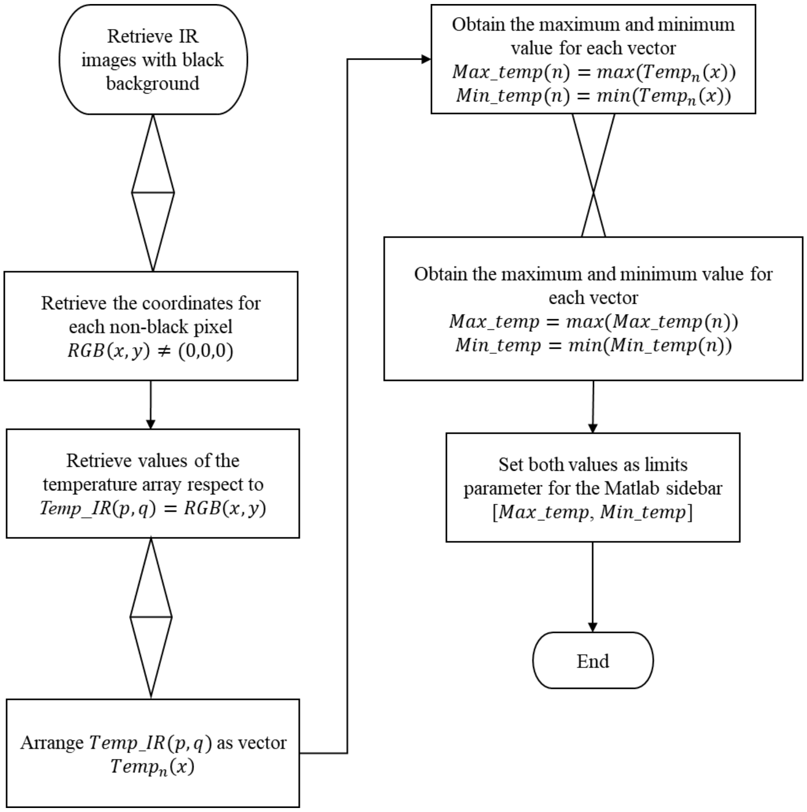

Figure 76: Flowchart for obtaining the limits of the color bar function for the temperature matrix set.

Figure 77 depicts a 3D surface lined by false color textures which are derived from the intensity of IR energy captured by the thermal camera, along with a temperature sidebar whose values correspond to the RoI temperatures. The values in the bar do not accurately represent the absolute temperature of the object but are only an approximation of the relative temperature measured by an indirect method by the thermographic camera. Also, it remains to find a way to display the temperature by a pointer to observe punctual information from a perspective. Furthermore, a loss in the quality of the model was observed. This loss is possible due to the conversion from PLY to the OBJ format. Perhaps it is possible to modify the code to save the result in OBJ format at the stage of reconstruction with MVS.

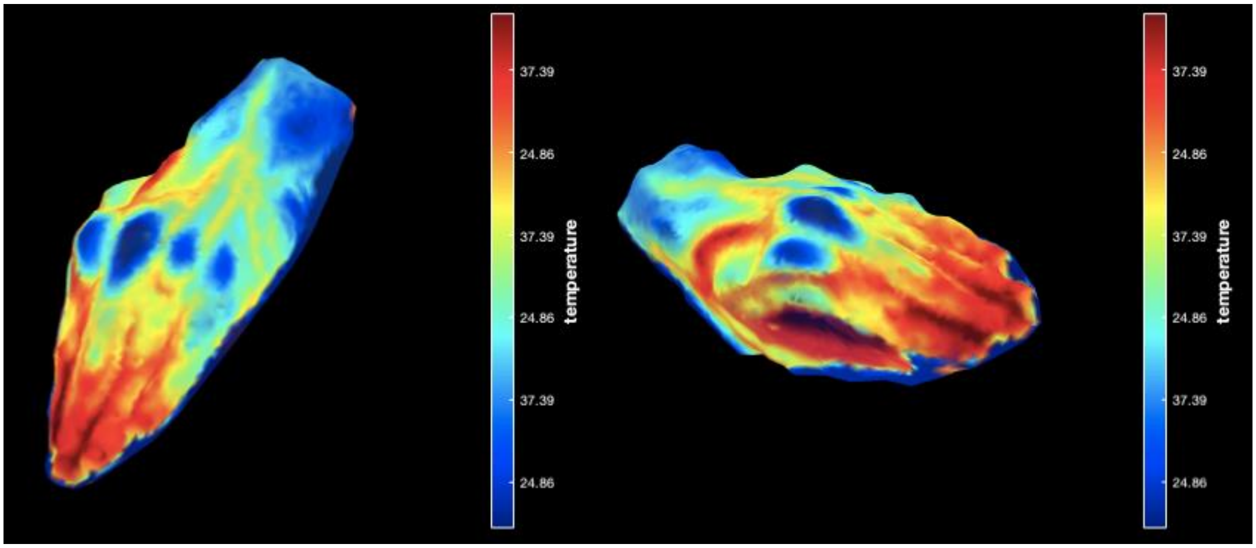

Figure 77: Thermographic 3D model with temperature scaled color bar

4.7 Conclusion

The different stages of a pipeline consisting of an incremental SfM method, the MVS step, the surface meshing, and the object texturing were presented in this chapter. Iterative point cloud building using incremental SfM techniques yields sparse point clouds lying on an extended surface. These sparse point clouds can be densified in the MVS step, which is a reliable and accurate method for a variety of applications, including those relating to multimodal image reconstruction [101,180,213].

Every region of interest in the image should have contrasted textures and/or structures. This is a strong motivation to jointly use multimodal images (thermal and visible light images), with the visible light images providing adequate features for 3D reconstruction. The used points of view should allow the acquisition of images from perspectives ensuring a large disparity in terms of angles between the camera axis. The objects should be viewed from various angles and distances, and under different scales both to cover the object surface and to facilitate the SfM and MVS steps. The scene may comprise surface parts or objects with high 3D structural information, such as surface shape variations, which enhance the performance of the SfM approach (visible light scene). Finally, while the lighting conditions vary between frames, they are generally moderate for the scene. Thermal interferences, on the other hand, should be avoided at all costs to improve RoI color contrast.

Since images in natural or industrial scenes contain rich information in terms of textures, and acquisition conditions can usually be controlled, or at least partially controlled, most of the acquisition conditions in the previous paragraph have been verified for a variety of applications. However, this may differ in the case of thermal 3D modeling since the combination of visible light images and thermal images is required to obtain a sparse 3D point cloud. Just employing only thermal images will lead to qualitatively incorrect models of a null point cloud.

In conclusion of the proposed method in this thesis, it is not the best solution to ascertain the temperature by region. This way to proceed makes the result dependent on the user's interpretation of a specific area's hue. Nevertheless, even in 2D IRT, where the images are displayed alongside a temperature sidebar, this technique is frequently used. This approach was also used in this thesis because IRT is a relative and indirect measurement that is dependent on the temperature prediction concerning the amount of IR energy recorded. Furthermore, because the RoI temperature array elements are of different sizes, normalizing the temperature regarding the minima and maxima detected in each frame provides an adequate approximation for displaying thermal information alongside the model.

Chapter 5

Thermal Surface Foot Reconstruction

Contents

5.1 Thermal Images for a Robustness Test

To test the robustness and limitations of the segmentation method, samples of IR radiometric information were obtained in uncontrolled environments on surfaces and backgrounds that would cause thermal interferences. The data were obtained by hand for the simplicity of having immediate samples in scenarios with possible errors in the capture protocol. The method described in Section 3.4.3 was tested with these samples to remove thermal interferences and segment the RoI maintaining the original scale, and then reconstructed as a false-color image. The data were obtained sequentially by holding the hand motionless while the thermographic equipment was rotated in the normal plane around the hand. Three collections of samples were obtained for different background scenarios and thermal interferences. Figure 78 shows some representative samples, in which the radiometric information was used to recreate a false-color image for illustration purposes. However, at this point, still, thermal interferences can be observed in the background.

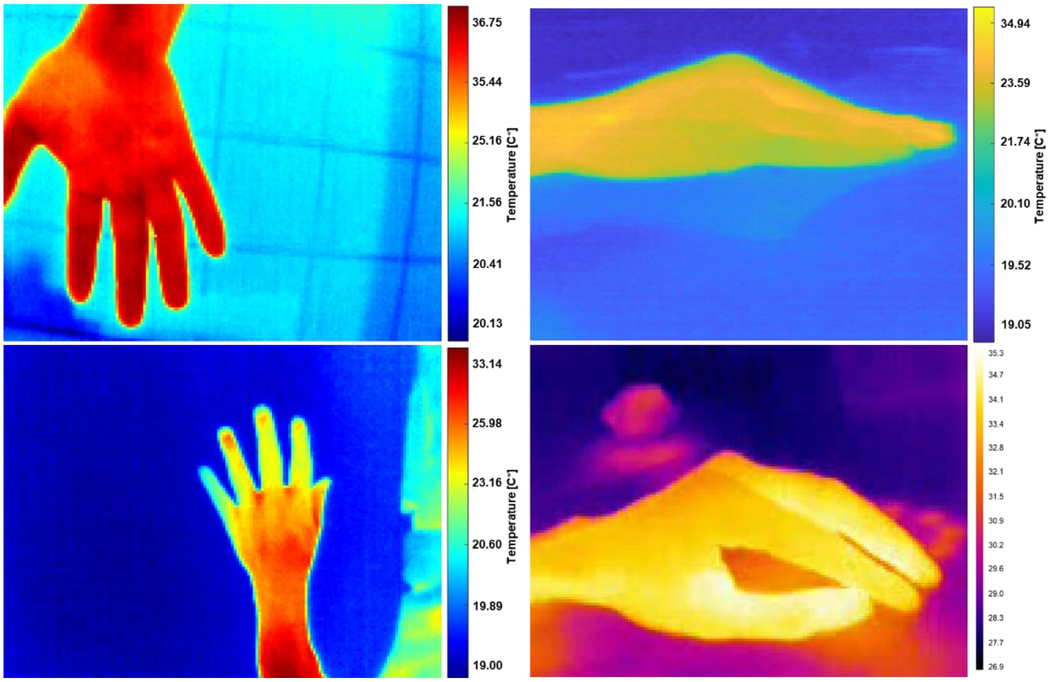

Figure 78: Samples of radiometric information in an uncontrolled environment are represented in false-color images. These samples were used to test the robustness of the automatic segmentation method

5.2 Thermal Calibration Results

A Calibration with a blackbody (radiator) was carried out to ensure precise temperature measurements. The goal is to match the temperature measurements to a gold standard thermometer. The data recorded of the blackbody by the thermal camera is depicted in Figure 79. The average error was 0.4 °C with a standard deviation of 0.2°C, which is considered acceptable to detect variations on a diabetic foot [71]. The ΔT was adjusted directly on the temperature matrix.

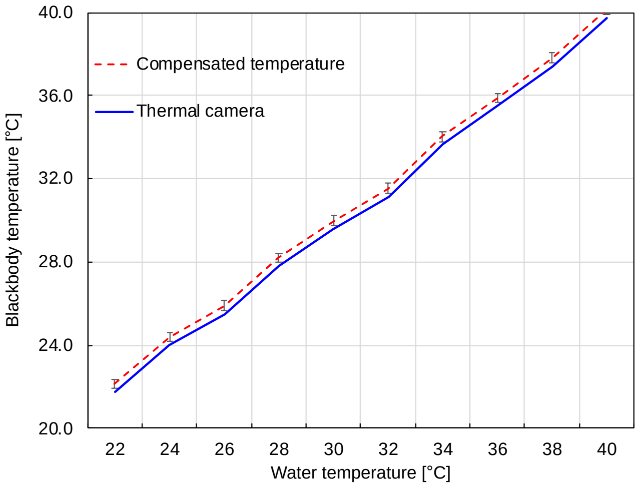

Figure 79: Temperature differences between the thermal camera and the thermometer values. The ground truth values are shown by the blue solid line which corresponds to the thermometer, while the values measured by the calibrated camera are represented by the red dashed line.

5.3 Segmentation Test Based on Radiometric Processing

Once the ΔT was adjusted, to establish the algorithm robustness, the segmentation approach was evaluated in uncontrolled conditions. Radiometric data including thermal interference and reflections were collected for this purpose. Figure 80 a) depicts a raw infrared image with thermal shadows and border blurring on the fingers and hand border, respectively. The result of the normalizing and thresholding methods mentioned in Section 3.4.2 is shown in Figure 80 b). The background in this image is uniform, and the RoI has low contrast. The outcome of normalizing the RoI values is shown in Figure 80 c). To illustrate the results, each temperature matrix was represented as a false-color image.

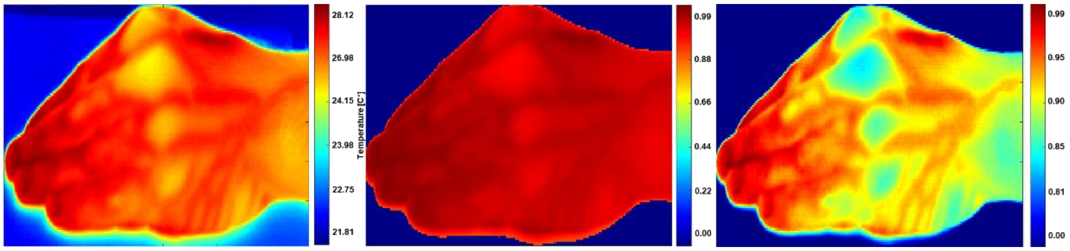

a) b) c)

Figure 80. Normalization and segmentation obtained in Section 3.4.2, **a**) False-color image with thermal interferences, b) IR image after thresholding step at 0.8. The image background is homogeneous as a result of the thresholding, and c) Color contrast on the RoI results in segmentation.

There is still the potential for interferences after the segmentation and contrast stages because of warm and large objects that are (accidentally) in the field of vision, resulting in strong intensity signals in the images. The method described in Section 3.4.2, on the other hand, allows for the removal of interference, which is always present at the image boundaries and is smaller than the RoI. (Figure 81). As shown in Figures 81 b), and c), smaller thermal interferences around the edges can also be recognized and deleted from the images.

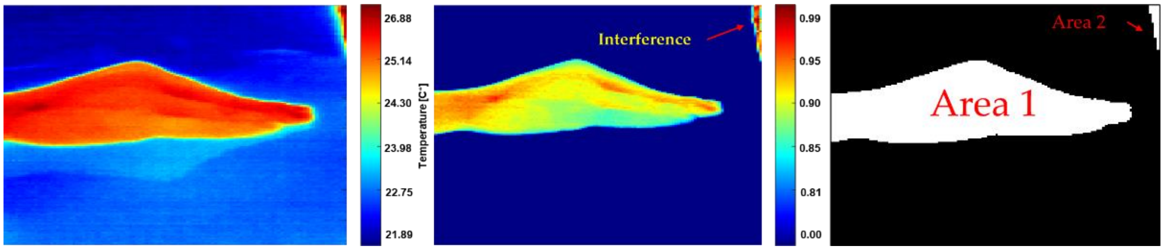

a) b) c)

Figure 81. The inference treatment is depicted in this image. (a) Raw infrared images with thermal interference and reflection, (b) normalized radiometric data with corner interference, and (**c**) areas 1 and 2, correspond to warm and large areas with ΔT < 2.6%, but only area 1 should be labeled as RoI.

Instead of processing a raw IR image, IR sub-data offers an RoI that includes a homogenous background, as seen in Figure 82. The color distribution associated with the temperature intensity measured by the sensors is interpreted in the reconstructed images using radiometric data.

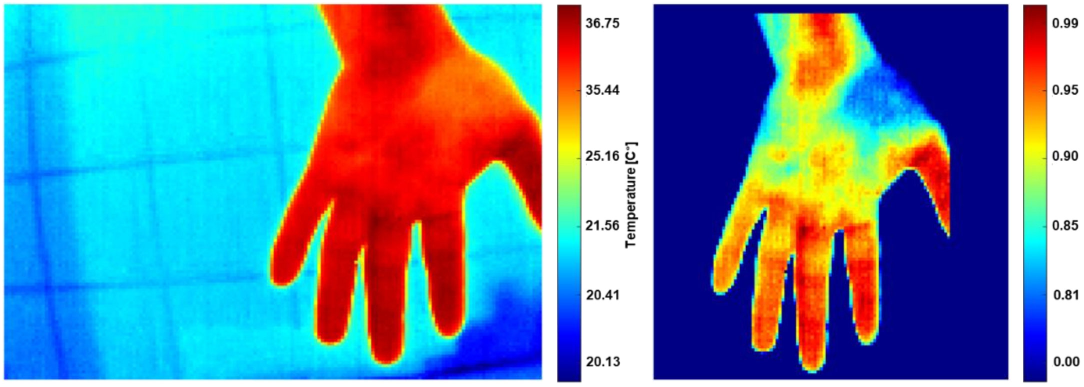

a) b)

Figure 82: a) Raw IR image, b) segmentation of the RoI, and removal of artifacts.

Even though the proposed method accurately segments the RoIs, it has certain limitations. After normalization, the temperatures in RoIs correspond to values greater than 0.8, resulting in intervals of 0 to 1, while the remaining temperatures (scene temperature) are set to zero. If interference has a temperature at least 2.6% higher than the RoI, this will be considered a background region by the segmentation method described in Section 3.4.2. Otherwise, they will be removed by discriminating the larger region in the capture frame. The background of the sub-image was turned into a transparent zone after RoI segmentation. Every pixel in the blue channel with a value of 131 was converted to a black pixel and then masked with maximum transparency (Figure 83 a) and b)).

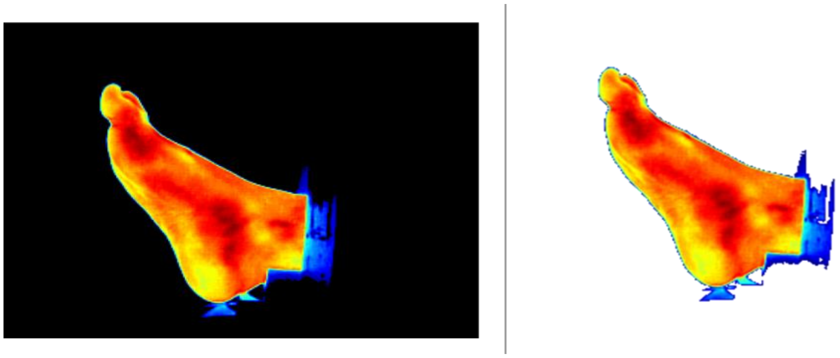

a) b)

Figure 83**.** Illustration of the transparency process. **a**) IR image with a black background and **b**) IR image with a transparent background.

5.4 Multimodal Image Registration Results

The Ti32 camera software offers a Picture-In-Picture feature that superimposes the images of both modalities, as depicted in Figure 84 a). Even when both common fields of vision are overlapped in the center, the IR image background remains, which is unnecessary for our purposes. Figure 84 b) indicates that, unlike the SmartView software, the suggested superimposition method enables the observation of only the foot in the IR image modality from any angle, while the rest of the scene retains the usual white light information.

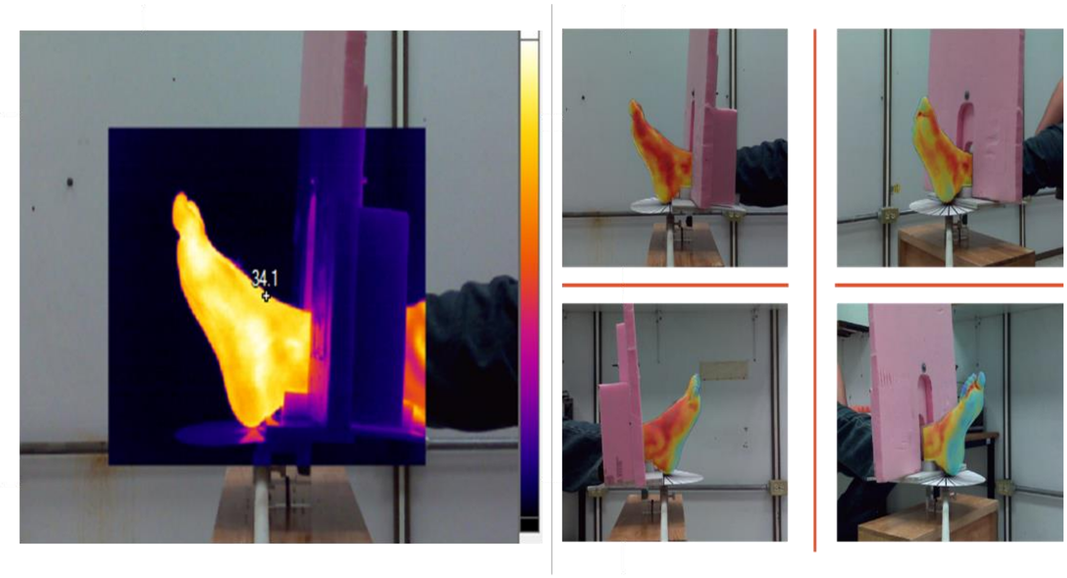

a) b)

Figure 84: Multimodal image representation: a) SmartView Picture-In-Picture image in which the IR is superimposed on the center of the visible-light image. b) Results of the merged stage, provided by an IR image with a transparent background and the visible-light image as the scene.

Figure 85 depicts a sample of 15 multimodal merged images in which the IR-RoI was precisely superimposed at all viewing angles about the corresponding region in the visible-light image, without the use of manual software mounting or RoI detection by classification.

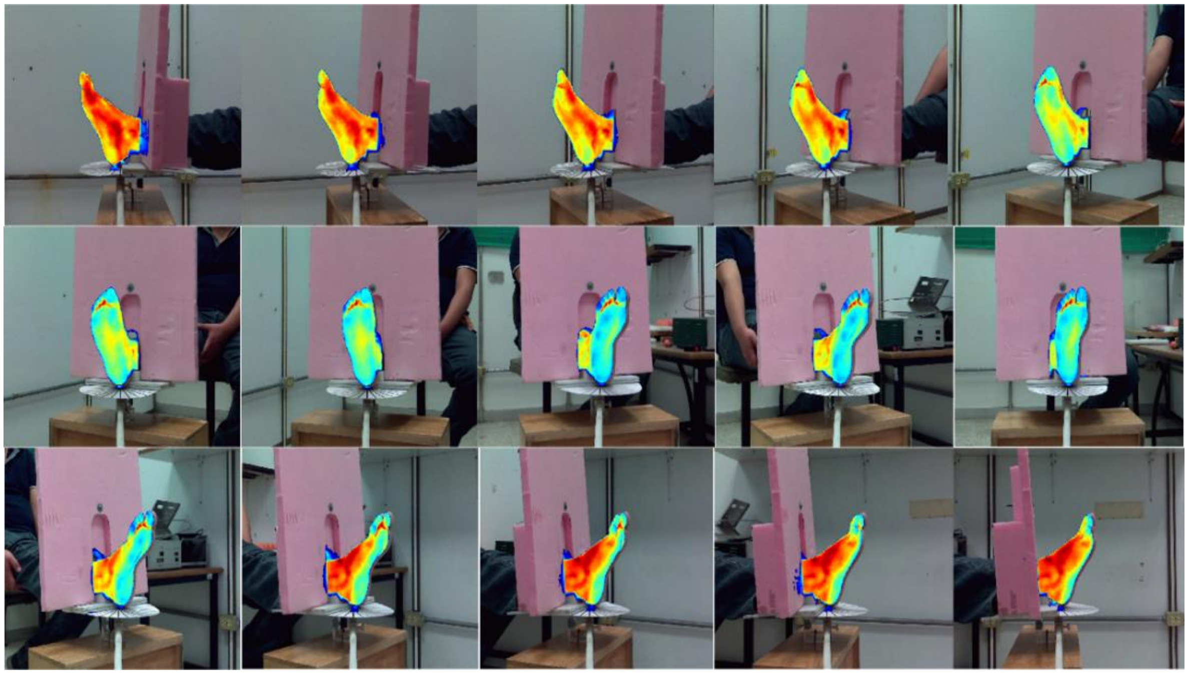

Figure 85: Set of 15 merged image pairs used for determining the 3D point cloud.

5.5 3D Surface Reconstruction

Even though each radiometric data array has a dimension of 320 x 240 pixels, the RoI differs depending on the angle of capture, as seen in the first columns of Table 14 "Image set S1" and "Image set S2". The RoI pixels consist of less than a third of the original matrix size.

Table 14. RoI elements from the S1 and S2 image collections It is also noteworthy that not every region of interest has the same number of elements.

Image N°	**Image Set S1 (Volunteer 1 Foot)**		**Image Set S2 (Volunteer 2 Foot)**	
	RoI Elements	**RoI %**	**RoI Elements**	**RoI %**
1	14,361	18.7	18,084	23.55
2	16,020	20.86	17,175	22.36
3	15,681	20.42	15,952	20.77
4	15,677	20.41	17,981	23.41
5	13,567	17.67	16,850	21.94
6	12,740	16.59	15,943	20.76
7	11,770	15.33	14,718	19.16
8	13,004	14.32	14,442	18.97
9	16,069	20.92	13,311	17.33
10	12,100	15.76	15,268	19.88
11	12,341	16.07	16,005	20.84
12	13,173	17.15	16,337	21.27
13	14,476	18.85	14,632	19.05
14	14,079	18.33	12,496	16.27
15	13,641	17.76	10,298	13.41

The SIFT algorithm is used to detect feature points, while their feature descriptors are used to find homologous points between image pairs. Figure 86 depicts that the correspondences are well refined in both multimodal regions (IR and visible light region). Even if COLMAP ultimately uses only homologous IR point pairs to reconstruct the sparse point of the foot surface, the determination of visible-light homologous point pairs (spread across the entire image, except in the center) is required for a precise camera displacement determination (external camera parameters) that affects the 3D point reconstruction accuracy. Table 15 presents the number of features per image modality, in which the superimposed images had fewer key points due to the false-color regions.

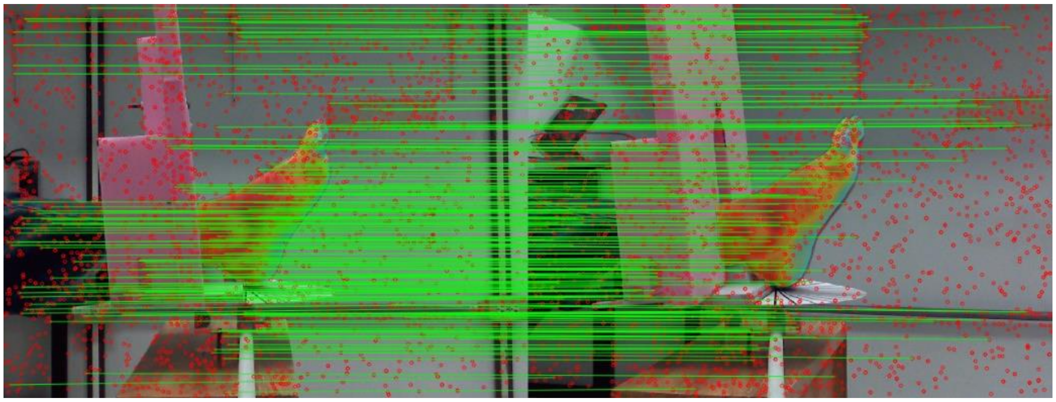

Figure 86. Detected feature points (red dots) and their correspondence visualized (the green lines represent the link between homologous points). This graph shows 202 matches between images 6 and 7 from set S1, with most of the critical points discarded, demonstrating that the model's quality is dependent on the precision of the matching points procedure.

Table 15. Detected and matched features in the two consecutive multimodal images.

Modality	**Image Set S1 (Volunteer 1 Foot)**	**Image Set S2 (Volunteer 2 Foot)**
	Detected Features	**Detected Features**
IR	307,404	99,887
Visible light	465,777	255,421
IR + Visible light	440,978	243,440

With SIFT data and potentially overlapping image pairings, as well as RANSAC as a robust technique for estimating suitable correspondences, the accuracy of a revolving camera gathering on a planar scene was determined in [101,102]. The sparse point cloud determination required robustly matched and correctly homologous point pairs from visible-light pictures. Indeed, for dense point cloud estimation and 3D reconstruction using MVS, the camera positions must be precisely specified. The placements of the rotating cameras are depicted in Figure 87. The statistics of COLMAP's surface reconstruction are shown in Table 16.

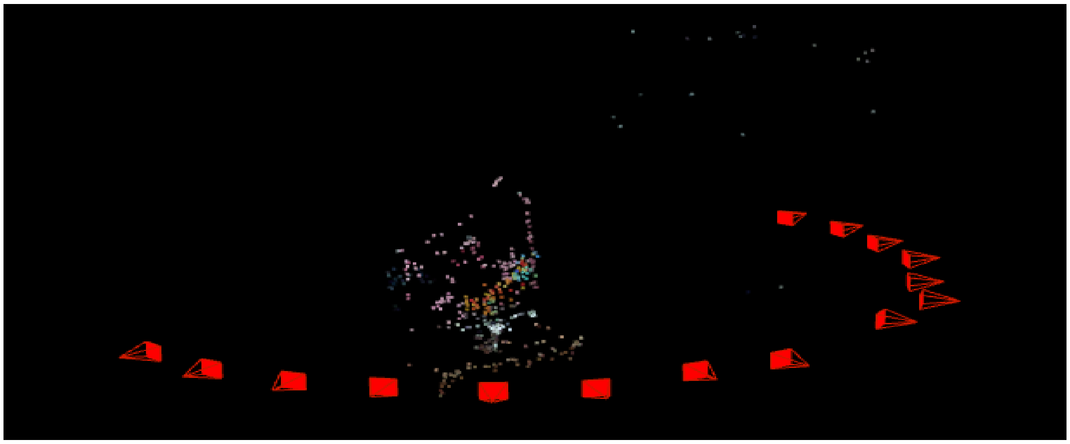

Figure 87: Successive camera poses (the vertex of the red tetrahedron indicates the camera optical center position while the complete tetrahedron represents the camera orientation). This figure also shows the sparse 3D point cloud determined by COLMAP.

Table 16. Statistics data retrieved by COLMAP.

Statistics	**Image Set S1 (Volunteer 1 Foot)**	**Image Set S2 (Volunteer 2 Foot)**
Cameras	15	15
Images	15	15
Registered images	15	15
Points	907	1573
Observations	2731	4649
Mean track length	3.01103	2.9555
Mean observations per image	182.067	309.933
Mean reprojection error	0.916495	0.955175

After obtaining the 3D point cloud, the model was transferred from the COLMAP software as an NVM file to the Open-MVS software, which was used to generate the dense 3D point cloud, meshing, and texturing. The point cloud is used to determine the reconstruction, refining, and texturing of a meshed surface. A PLY format model is obtained at the end of the process, along with its related texture in PNG format. The total computation time for this entire processing chain was:

- Image set S1: 2.47 min
- Image set S2: 3.12 min

5.6 Angular Emissivity Correction

The temperature error caused by the angular trajectory was adjusted once the 3D reconstruction of the foot model was completed. Table 17 displays the percentage errors for the reference sample when seen from a normal angle. As the angle increased, the average temperature between the metatarsal zone and the heel increased. Near 90°, the inaccuracy was approximately 10% for both samples.

Table 17. ΔT regarding the angle of measurement. The temperature in the original thermal arrays was corrected with the computed delta.

Angle of Acquisition (°)	**Image Set S1 (Volunteer Foot 1)**		**Image Set S2 (Volunteer Foot 2)**	
	Average Temperature (°C)	**ΔT (%)**	**Average Temperature (°C)**	**ΔT (%)**
0	32.44	0.00	31.01	0.00
12	32.84	3.22	31.19	1.63
24	32.88	3.54	31.28	2.45
36	33.16	5.79	31.63	5.63
48	33.24	6.43	31.83	7.45
60	33.31	6.99	31.89	7.99
72	33.24	6.43	32.02	9.17
84	33.64	9.65	32.24	11.17

The error calculated for each angle was adjusted in the thermal map, resulting in the most accurate temperature for each array, as if recorded at a normal angle. The maximum and minimum temperatures for each pair of images were obtained after correction. Because the standard deviation is less than 1°C, the results prove that this approach could be an adequate technique for associating temperature intensity with a color scale. Table 18 shows the average temperature estimated from the radiometric data arrays for image sets S1 and S2.

Table 18. For image sets S1 and S2, the average maximum and minimum temperatures were calculated. The temperature standard deviations were less than one degree, which is acceptable for using passive thermography as a reliable method of gathering data.

Image Set	Average Maximum Temperature (°C)	Standard Deviation (°C)	Average Minimum Temperature (°C)	Standard Deviation (°C)
S1	36.54	0.24	29.89	0.67
S2	35.04	0.56	30.12	0.78

5.7 3D Model Viewing and Thermal Data Correlation

The surfaces of volunteer 1 and volunteer 2 feet are shown in Figure 88. On the right side of each model, a color bar with temperature data is provided, associating each color with the surface temperature. The 3D model only reveals temperatures for the foot as wrapping textures, allowing for a quick examination of the foot's anatomical and physiological health.

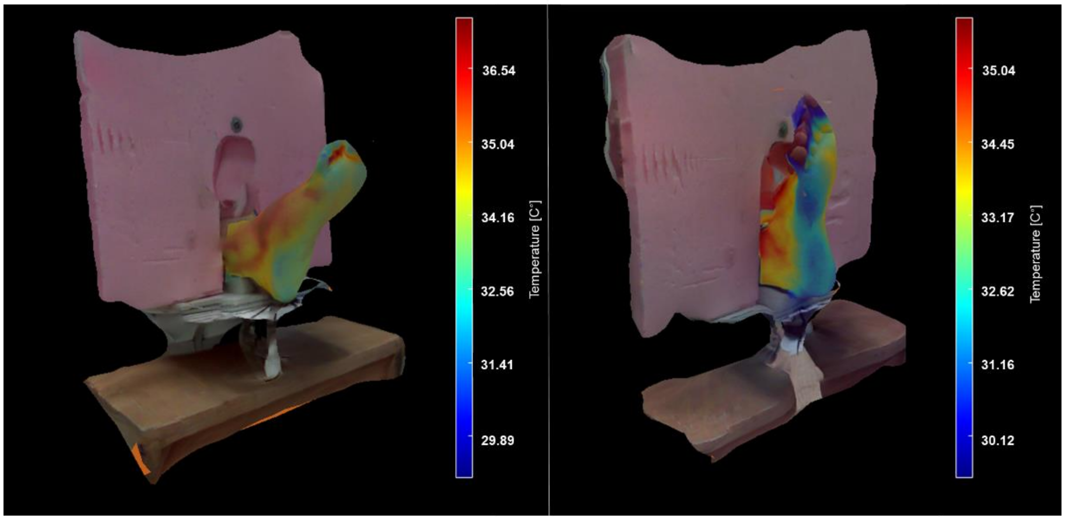

a) b)

Figure 88. 3D models of the foot in a thermal surface and a visible-light environment. a) Volunteer 1 and b) Volunteer 2.

5.8 Conclusions

The results demonstrate the feasibility and utility of extracting and processing radiometric data to retrieve a segmented IR image combined in a textured visible-light scene. Before interpreting thermal maps as images, an IR radiometric processing approach can remove background thermal interference using thresholds as segmentation criteria. Under particular conditions, such as a controlled environment and the elimination of heat sources in which the $\Delta T < 2.6\%$ relative to the RoI, this strategy leads to the automation of the process regardless of the targeted RoI. Thermal array segmentation would be inadequate under other circumstances. Medical thermography protocols, on the other hand, recommend sampling in a controlled environment to prevent interfering factors. Our research shows that the proposed method is accurate when these guidelines are followed.

The thermal equipment solves the parallax problem; therefore, no additional thermal/spatial calibration was needed. Furthermore, the size would allow for future clinical validation by allowing the gadget to be carried to health centers for testing. Only a thermal calibration against a reference thermometer on a body with known thermal distribution was performed, with $\Delta T = 0.4°C$ corrected. Furthermore, the ΔT inaccuracy due to the angular emissivity factor was adjusted (error $\approx 10\%$ near 90°), which is a common difficulty in 3D thermography research. Without angle adjustment, both sets had a distribution error of 4.74°C on average.

It is indeed important to note that the RoI detection was not based on a specific foot segmentation or the implementation of a neural network. As a result, one of the benefits of this method is that it may be applied to additional RoI segmentation using radiometric data applications, such as portable IR thermography devices and prototypes based on embedded systems. Both sensors, however, will require a registration and calibration technique. For instance, this study was conducted using thermographic equipment built for general/industrial use, with dimensions and handling that could allow future investigations to be carried out in research laboratories or health facilities.

The COLMAP process requires an accurate feature recognition and matching step for surface reconstruction, which cannot be guaranteed when just IR images with few textures are employed. As a result, the visible-light images were required as extra data for the SfM approach to generate surfaces reliably and precisely. As the 3D model for the S2 set has demonstrated, the qualitative accuracy of a 3D surface is determined by the quality of the images rather than the number of key points. Although S1 featured 42% fewer important features than S2, the reconstruction was visually correct (see Table 17). Improving the visible-light sensor by using newer cameras with higher resolution and smaller pixel sizes could be one approach. However, because they only cover the surface of the model where the color distribution is directly proportional to the temperature intensity, the IR radiometric arrays were critical in determining IR pictures that were used as a "wrapping texture" method. Because the model is displayed with a temperature scale, it is important to allocate the color distribution appropriately to the RoI temperature intensity. Since angular emissivity is an issue in thermography, the temperature was corrected for the angle of capture. The ΔT according to the reference sample was suggested to be a linear problem, so the temperature matrix accuracy was compensated by using Equation (18). The error adjustment did not influence the color distribution in the RoI but did influence the scale along with the 3D model.

Conclusions and perspectives

IR medical thermography is widely accepted as a reliable method for detecting temperature changes and assessing the progression of diseases, such as diabetic foot issues. The advantages of medical IRT are based on the exploration of abnormal and asymmetry temperature patterns, thus providing a 3D model of the foot textured with thermal information may be considered a valuable tool for anticipated diagnosis. Studies related to IR modeling have proven that the input images are required to be a multimodal fusion between images in the visible and IR spectrum. Although multimodal fusion is solved by image registration, segmentation in thermal imaging remains done manually.

Automatic processing has the advantage of treating all data and image arrays with the same segmentation criteria, avoiding time-consuming and individual manipulation that is frequently vulnerable to user interpretation. The contribution of this thesis, in terms of the most often stated methodologies in the state-of-the-art, is the automatic processing of IR radiometric data without relying on manual manipulation which approaches the thermal information as a signal instead of an image prior to the 3D reconstruction stages. Under particular conditions, the segmentation approach is accurate: the RoI should be warmer than the background to threshold values higher than 0.8 in a range-normalized array [0 to 1], and background thermal interferences should be minimal by $\Delta T < 2.6\%$, regarding the RoI (otherwise, the RoI would be transformed into a background component). Because of this constraint, it is recommended that either a thermal insulating background be used or that thermal artifacts such as light sources be avoided; also, personnel may induce thermal artifacts. In essence, the automatic segmentation and registration method was employed to generate multimodal merged images, in which only the RoI had false colors corresponding to the measured temperature. The 3D structure estimation technique would then use the foreground components (visible light) as a reference to determine the 3D sparse point cloud, and the RoI would be used as a "wrapping texture" approach. Otherwise, it is impossible to achieve a correct correspondence using only false-color images, therefore the retrieved point cloud would be inaccurate or null.

The perspective of this work lies in analyzing the spatial and thermal accuracy, which spatial accuracy has already been studied in the work of Phan et al. on visible-light images for endoscopy images [101]. Moreover, image registration methods are starting to have more frequent applications in the biomedical area. González-Perez et al. [108] have carried out a comparative study on the accuracy of multimodal image registration. However, the segmentation in thermal imaging is still done manually, so this work complements these studies by proposing an automatic method that can be tested with the perspective of early diagnosis of diabetic foot. Furthermore, clinical validation is expected in the near future to assess the opinion of physicians at the first frontline in health centers. These studies are focused on diabetic patients without a history of DF. Some studies have been conducted on the parallel to implement a quantitative detection method that can be implemented in 3D models (so far, they have only been implemented in 2D).

In conclusion, providing a 3D model of the foot as a single entity instead of the inspection of multiple images is an advantage that offers the physician to reduce inspection and diagnosis times. The model represents the RoI only with a color map corresponding to the temperature providing the physiological state of the foot that can hardly be perceptible from the surface. In this way, the physician will have an additional diagnostic tool to help prevent issues like the diabetic foot. The 3D model may come in handy to assess the physiological status of the foot by evaluating for asymmetry or regional temperature abnormalities, as well as providing additional diagnostic criteria.

Bibliography

1. Cho, N.H. IDF Diabetes Atlas Ninth Edition 2019; www. inisco.; 2019; ISBN 978-2-930229-87-4.
2. Federation World Health Organization and International Diabetes Definition and Diagnosis of Diabetes Mellitus and Intermediate Hyperglycaemia.
3. Fendler, W.; Borowiec, M.; Baranowska-Jazwiecka, A.; Szadkowska, A.; Skala-Zamorowska, E.; Deja, G.; Jarosz-Chobot, P.; Techmanska, I.; Bautembach-Minkowska, J.; Mysliwiec, M.; et al. Prevalence of Monogenic Diabetes amongst Polish Children after a Nationwide Genetic Screening Campaign. Diabetologia 2012, 55, 2631–2635, doi:10.1007/s00125-012-2621-2.
4. Tirado, R.A. del C.; López, J.A.F.; Tirado, F.J. del C. Guía de Práctica Clínica En El Pie Diabético. Archivos de Medicina 2014, 10, 1–17, doi:10.3823/1211.
5. Jiao, F.F.; Cheung Fung, C.S.; Fai Wan, E.Y.; Chun Chan, A.K.; McGhee, S.M.; Ping Kwok, R.L.; Kuen Lam, C. Lo Five-Year Cost-Effectiveness of the Multidisciplinary Risk Assessment and Management Programme–Diabetes Mellitus (RAMP- DM). Diabetes Care 2018, doi:10.2337/dc17-1149.
6. Gómez Hoyos, E.; Levy, A.E.; Díaz Perez, A.; Cuesta Hernández, M.; Montañez Zorrilla, C.; Calle Pascual, A.L. Pie Diabético. Seminarios de la Fundación Española de Reumatología 2012, 13, 119–129, doi:10.1016/J.SEMREU.2012.06.003.
7. Ueki, K.; Sasako, T.; Okazaki, Y.; Kato, M.; Okahata, S.; Katsuyama, H. Effect of an Intensified Multifactorial Intervention on Cardiovascular Outcomes and Mortality in Type 2 Diabetes (J-DOIT3): An Open-Label, Randomised Controlled Trial. Lancet Diabetes Endocrinol 2017, 5, 951–64.
8. Izumi, Y.; Satterfield, K.; Lee, S.; Harkless, L. Risk of Reamputation in Diabetic Patients. Diabetes Care 2006, 29, 566–570.
9. Sarin, S.; Shami, S.; Shields, D.A.; Scurr, J.H.; Coleridge Smith, P.D. Selection of Amputation Level: A Review. European Journal of Vascular Surgery 1991, 5, 611–620, doi:10.1016/S0950-821X(05)80894-1.
10. Apelqvist, J.; Bakker, K.; Van Houtum, W.H.; Nabuurs-Franssen, M.H.; Schaper, N.C. International Consensus and Practical Guidelines on the Management and the Prevention of the Diabetic Foot. Diabetes/Metabolism Research and Reviews 2000, 16.
11. Viswanathan, V.; Madhavan, S.; Rajasekar, S.; Chamukuttan, S.; Ambady, R. Amputation Prevention Initiative in South India: Positive Impact of Foot Care Education. Diabetes Care 2005, 28, 1019–1021, doi:10.2337/diacare.28.5.1019.
12. Lavery, L.A.; Armstrong, D.G.; Vela, S.A.; Quebedeaux, T.L.; Fleischli, J.G. Practical Criteria for Screening Patients at High Risk for Diabetic Foot Ulceration. Archives of Internal Medicine 1998, 158, doi:10.1001/archinte.158.2.157.
13. Frykberg, R.G. Diabetic Foot Ulcers: Current Concepts. Journal of Foot and Ankle Surgery 1998, 37, doi:10.1016/S1067-2516(98)80055-0.
14. Reiber, G.E.; Boyko, E.J.; Smith, D.G. Lower Extremity Foot Ulcers and Amputations in Diabetes. Lower Extremity 1995, 2.
15. Wagner, F.Jr. The Diabetic Foot. Orthopedics; 1987;
16. PREVENTIVE MEASURES FOR DIABETIC FOOT ULCERS – Valuechain Online Available online: https://www.thevaluechainng.com/preventive-measures-for-diabetic-foot-ulcers/ (accessed on 29 September 2021).
17. van Netten, J.J.; Price, P.E.; Lavery, L.A.; Monteiro-Soares, M.; Rasmussen, A.; Jubiz, Y.; Bus, S.A. Prevention of Foot Ulcers in the At-Risk Patient with Diabetes: A Systematic Review. Diabetes/Metabolism Research and Reviews 2016, 32, 84–98, doi:10.1002/dmrr.2701.
18. Armstrong, D.G.; Lavery, L.A. Diabetic Foot Ulcers: Prevention, Diagnosis and Classification. American Family Physician 1998, 57.
19. Lavery, L.A.; Armstrong, D.G.; Harkless, L.B. Classification of Diabetic Foot Wounds. Journal of Foot and Ankle Surgery 1996, 35, doi:10.1016/S1067-2516(96)80125-6.

20. Dros, J.; Wewerinke, A.; Bindels, P.J.; Weert, H.C. van Accuracy of Monofilament Testing to Diagnose Peripheral Neuropathy: A Systematic Review. Annals of Family Medicine 2009, 7, 555, doi:10.1370/AFM.1016.

21. Bayareh, R.; Maldonado, H.; Torres, I.A.; Vera, A.; Leija, L. Thermographic Study of the Diabetic Foot of Patients with Diabetes Mellitus and Healthy Patients. 2018 Global Medical Engineering Physics Exchanges/Pan American Health Care Exchanges, GMEPE/PAHCE 2018 2018, 1–5, doi:10.1109/GMEPE-PAHCE.2018.8400742.

22. Bus, S.A.; Lavery, L.A.; Monteiro-Soares, M.; Rasmussen, A.; Raspovic, A.; Sacco, I.C.N.; Netten, J.J. van IWGDF Guideline on the Prevention of Foot Ulcers in Persons with Diabetes. Diabetes/Metabolism Research and Reviews 2019, 1–36.

23. Uçkay, I.; Aragón-Sánchez, J.; Lew, D.; Lipsky, B.A. Diabetic Foot Infections: What Have We Learned in the Last 30 Years? International Journal of Infectious Diseases 2015, 40, 81–91, doi:10.1016/j.ijid.2015.09.023.

24. Liu, C.; van Netten, J.J.; Klein, M.E.; van Baal, J.G.; Bus, S.A.; van der Heijden, F. Statistical Analysis of Spectral Data: A Methodology for Designing an Intelligent Monitoring System for the Diabetic Foot. Journal of Biomedical Optics 2013, 18, 126004, doi:10.1117/1.jbo.18.12.126004.

25. Bus, S.A.; van Netten, J.J.; Lavery, L.A.; Monteiro-Soares, M.; Rasmussen, A.; Jubiz, Y.; Price, P.E. IWGDF Guidance on the Prevention of Foot Ulcers in At-Risk Patients with Diabetes. Diabetes/Metabolism Research and Reviews 2016, 32, 16–24, doi:10.1002/dmrr.2696.

26. Liu, P.Y.; Shi, Z.Y.; Sheu, W.H.H. Diagnosis and Treatment of Diabetic Foot Infections. Journal of Internal Medicine of Taiwan 2012, 23, 431–441, doi:10.7547/0950183.

27. Lázaro-Martínez, J.L.; García-Madrid, M.; García-Álvarez, Y.; Álvaro-Afonso, F.J.; Sanz-Corbalán, I.; García-Morales, E. Conservative Surgery for Chronic Diabetic Foot Osteomyelitis: Procedures and Recommendations. Journal of Clinical Orthopaedics and Trauma 2021, 16, doi:10.1016/j.jcot.2020.12.014.

28. Tronstad, C.; Johnsen, G.K.; Grimnes, S.; Martinsen, Ø.G. A Study on Electrode Gels for Skin Conductance Measurements. Physiological Measurement 2010, 31, 1395–1410, doi:10.1088/0967-3334/31/10/008.

29. Naranjo-Hernández, D.; Reina-Tosina, J.; Min, M. Fundamentals, Recent Advances, and Future Challenges in Bioimpedance Devices for Healthcare Applications. Journal of Sensors 2019, 2019, 1–42, doi:10.1155/2019/9210258.

30. Lahiri, B.B.; Bagavathiappan, S.; Jayakumar, T.; Philip, J. Medical Applications of Infrared Thermography: A Review. Infrared Physics and Technology 2012, 55, 221–235, doi:10.1016/j.infrared.2012.03.007.

31. Chen, W. Thermometry and Interpretation of Body Temperature. Biomedical Engineering Letters 2019, 9, 3–17, doi:10.1007/s13534-019-00102-2.

32. Eser Sanverdi, S.; Bilge Ergen, F.; Oznur, A. Current Challenges in Imaging of the Diabetic Foot. Diabetic Foot and Ankle 2012, 3.

33. van Doremalen, R.F.M.; van Netten, J.J.; van Baal, J.G.; Vollenbroek-Hutten, M.M.R.; van der Heijden, F. Infrared 3D Thermography for Inflammation Detection in Diabetic Foot Disease: A Proof of Concept. Journal of Diabetes Science and Technology 2019, 14, 46–54, doi:10.1177/1932296819854062.

34. Bayareh Mancilla, R.; Tấn, B.; Daul, C.; Gutiérrez Martínez, J.; Leija Salas, L.; Wolf, D.; Vera Hernández, A. Anatomical 3D Modeling Using IR Sensors and Radiometric Processing Based on Structure from Motion: Towards a Tool for the Diabetic Foot Diagnosis. Sensors 2021, 21, 3918, doi:10.3390/s21113918.

35. Anbar, M. The Emergence of a New Diagnostic Imaging Modality. International Journal of Technology Assessment in Health Care 1987, 3, 631–621.

36. Jasti, N.; Bista, S.; Bhargav, H.; Sinha, S.; Gupta, S.; Chaturvedi, S.K.; Gangadhar, B.N. Medical Applications of Infrared Thermography: A Narrative Review. Journal of Stem Cells 2019, 14, 35–53.

37. Tan, J.H.; Ng, E.Y.K.; Rajendra Acharya, U.; Chee, C. Infrared Thermography on Ocular Surface Temperature: A Review. Infrared Physics & Technology 2009, 52, 97–108, doi:10.1016/J.INFRARED.2009.05.002.

38. Boulant, J.A. Hypothalamic Mechanisms in Thermoregulation. Federation Proceedings 1981, 40.

39. Fernández-Cuevas, I.; Bouzas Marins, J.C.; Arnáiz Lastras, J.; Gómez Carmona, P.M.; Piñonosa Cano, S.; García-Concepción, M.Á.; Sillero-Quintana, M. Classification of Factors Influencing the Use of Infrared Thermography in Humans: A Review. Infrared Physics and Technology 2015, 71, 28–55, doi:10.1016/j.infrared.2015.02.007.

40. Ring, E.F.J. The Historical Development of Temperature Measurement in Medicine. Infrared Physics and Technology 2007, 49, 297–301, doi:10.1016/J.INFRARED.2006.06.029.

41. Hardy, J.D.; Muschenheim, C. RADIATION OF HEAT FROM THE HUMAN BODY. V. THE TRANSMISSION OF INFRA-RED RADIATION THROUGH SKIN. Journal of Clinical Investigation 1936, 15, 1,

doi:10.1172/JCI100746.

42. Bell, I.G. Infrared Thermography. Journal of the Japan Society for Precision Engineering 1990, 56, 1961–1966, doi:10.2493/jjspe.56.1961.

43. Ring, E.F.J. The Historical Development of Temperature Measurement in Medicine. Infrared Physics and Technology 2007, 49, doi:10.1016/j.infrared.2006.06.029.

44. Langley, S.P. The Bolometer and Radiant Energy. Proceedings of the American Academy of Arts and Sciences 1880, 16, 342, doi:10.2307/25138616.

45. Diakides, N.A.; Diakides, M.; Lupo, J.; Paul, J.L.; Balcerak, R. Advances in Medical Infrared Imaging. In Medical Devices and Systems; CRC Press, 2006; pp. 19-1-19–14 ISBN 9781420003864.

46. Bernard, V.; Staffa, E.; Mornstein, V.; Bourek, A. Infrared Camera Assessment of Skin Surface Temperature - Effect of Emissivity. Physica Medica 2013, 29, 583–591, doi:10.1016/j.ejmp.2012.09.003.

47. Bayareh-Mancilla, R.; Vera-Hernández, A.; Leija-Salas, L.; Ramos, A.; Gutierrez-Martínez, J. Characterization of a Longwave Infrared Imager for the Telemetric Measurement of Human Skin Temperature of Diabetic Foot. In Proceedings of the Pan American Health Care Exchanges, PAHCE; 2017; Vol. 2017-March, pp. 70–74.

48. Lepton LWIR Micro Thermal Camera Module | Teledyne FLIR Available online: https://www.flir.eu/products/lepton/ (accessed on 10 October 2021).

49. Anbar, M.; Montoro, J. New Modes of Data Handling in Computerized Thermography. Proceedings of the 10th Annual International Conference of the IEEE Engineering in Medicine and Biology Society 1988, 10.

50. Bhargava, A.; Chanmugam, A.; Herman, C. Heat Transfer Model for Deep Tissue Injury: A Step towards an Early Thermographic Diagnostic Capability. Diagnostic Pathology 2014, 9, 1–18, doi:10.1186/1746-1596-9-36.

51. Head, J.F.; Elliott, R.L. Infrared Imaging: Making Progress in Fulfilling Its Medical Promise. IEEE Engineering in Medicine and Biology Magazine 2002, 21, 80–85, doi:10.1109/MEMB.2002.1175142.

52. Monje-Arenas, L.; Pérez-Mallada, N. Medical Thermography. Photography in Clinical Medicine 2020, 515–526, doi:10.1007/978-3-030-24544-3_30.

53. Farooq, M.A.; Corcoran, P. Infrared Imaging for Human Thermography and Breast Tumor Classification Using Thermal Images. In Proceedings of the 2020 31st Irish Signals and Systems Conference, ISSC 2020; Institute of Electrical and Electronics Engineers Inc., June 1 2020.

54. Mota-Rojas, D.; Titto, C.G.; Orihuela, A.; Martínez-Burnes, J.; Gómez-Prado, J.; Torres-Bernal, F.; Flores-Padilla, K.; Fuente, V.C. la; Wang, D. Physiological and Behavioral Mechanisms of Thermoregulation in Mammals. Animals 2021, Vol. 11, Page 1733 2021, 11, 1733, doi:10.3390/ANI11061733.

55. Dang, J.; Lin, M.; Tan, C.; Pham, C.H.; Huang, S.; Hulsebos, I.F.; Yenikomshian, H.; Gillenwater, J. Use of Infrared Thermography for Assessment of Burn Depth and Healing Potential: A Systematic Review. Journal of Burn Care & Research 2021, doi:10.1093/JBCR/IRAB108.

56. Mazeika, E.; Jariene, V.; Valiukeviciene, S. Medical Infrared Thermography as Hidradenitis Suppurativa Diagnostic Tool: Literature Review. Postepy Dermatologii i Alergologii 2021, 38, 32–35, doi:10.5114/ADA.2021.104274.

57. Bayareh Mancilla, R.; Daul, C.; Gutierrez-Martínez, J.; Vera Hernández, A.; Wolf, D.; Leija Salas, L. Detection of Sore-Risk Regions on the Foot Sole with Digital Image Processing and Passive Thermography in Diabetic Patients. 17th International Conference on Electrical Engineering, Computing Science and Automatic Control (CCE) 2020.

58. BG, V. FPA-Based Infrared Thermography as Applied to the Study of Cutaneous Perspiration and Stimulated Vascular Response in Humans. Physics in medicine and biology 2005, 50, doi:10.1088/0031-9155/50/23/R01.

59. Toro, J.R.; Poy, P.J.E. Valoración Con Termografía Infrarrojo, de La Capacidad Vasodilatadora de Las Diferentes Corrientes Analgésicas y Factores Implicados. Rehabilitacion 2012, 46, 7–14, doi:10.1016/J.RH.2011.12.003.

60. Mneimneh, F.; Ghaddar, N.; Ghali, K.; Moussalem, C.; Omeis, I. Modeling the Effect of Cooling Vest on Body Thermal Response of People with Paraplegia during Exercise. In Proceedings of the ASME 2019 Heat Transfer Summer Conference, HT 2019, collocated with the ASME 2019 13th International Conference on Energy Sustainability; 2019.

61. Amalu, W.C.; Hobbins, W.B.; Head, J.F.; Elliott, R.L. Infrared Imaging of the Breast - An Overview. Medical Devices and Systems 2006, 25-1-25–21, doi:10.1201/9781420003864.ch25.

62. Tang, X.; Ding, H.; Yuan, Y.; Wang, Q. Morphological Measurement of Localized Temperature Increase Amplitudes in Breast Infrared Thermograms and Its Clinical Application. Biomedical Signal Processing and

Control 2008, 4, 312–318, doi:10.1016/J.BSPC.2008.04.001.

63. Borchartt, T.B.; Conci, A.; Lima, R.C.F.; Resmini, R.; Sanchez, A. Breast Thermography from an Image Processing Viewpoint - A Survey. 2013, 93, 2785–2803.

64. de Queiroz Júnior, J.R.A.; de Lima, R. de C.F. Three-Dimensional Modeling of Female Breast Based on Thermograms for Thermophysical Studies of Breast Pathologies. Research on Biomedical Engineering 2020, doi:10.1007/s42600-020-00096-2.

65. Van Netten, J.J.; Van Baal, J.G.; Liu, C.; Van Der Heijden, F.; Bus, S.A. Infrared Thermal Imaging for Automated Detection of Diabetic Foot Complications. Journal of Diabetes Science and Technology 2013, 7, 1122–1129, doi:10.1177/193229681300700504.

66. Vilcahuaman, L.; Canals, R.; Zequera, M.L.; Wilches, C. Detection of Diabetic Foot Hyperthermia by Infrared Imaging Automatic Analysis of Plantar Foot Thermal Images in At-Risk Type II Diabetes by Using an Infrared Camera. 2014, doi:10.1109/EMBC.2014.6944705.

67. Bayareh, R.; Vera, A.; Leija, L.; Gutierrez-Martínez, J. Development of a Thermographic Image Instrument Using the Raspberry Pi Embedded System for the Study of the Diabetic Foot. I2MTC 2018 - 2018 IEEE International Instrumentation and Measurement Technology Conference: Discovering New Horizons in Instrumentation and Measurement, Proceedings 2018, 1–6, doi:10.1109/I2MTC.2018.8409841.

68. Nagase, T.; Sanada, H.; Takehara, K.; Oe, M.; Iizaka, S.; Ohashi, Y.; Oba, M.; Kadowaki, T.; Nakagami, G. Variations of Plantar Thermographic Patterns in Normal Controls and Non-Ulcer Diabetic Patients: Novel Classification Using Angiosome Concept. Journal of Plastic, Reconstructive and Aesthetic Surgery 2011, 64, 860–866, doi:10.1016/j.bjps.2010.12.003.

69. Tulloch, J.; Zamani, R.; Akrami, M. Machine Learning in the Prevention , Diagnosis and Management of Diabetic Foot Ulcers : A Systematic Review. 2020, 1–44, doi:10.1109/ACCESS.2020.3035327.

70. Khodayar, F.; Sojasi, S.; Maldague, X. Infrared Thermography and NDT: 2050 Horizon. Quantitative InfraRed Thermography Journal 2016, 13, 210–231, doi:10.1080/17686733.2016.1200265.

71. Wijlens, A.M.; Holloway, S.; Bus, S.A.; van Netten, J.J. An Explorative Study on the Validity of Various Definitions of a 2·2°C Temperature Threshold as Warning Signal for Impending Diabetic Foot Ulceration. International Wound Journal 2017, doi:10.1111/iwj.12811.

72. Armstrong, D.G.; Holtz-Neiderer, K.; Wendel, C.; Mohler, M.J.; Kimbriel, H.R.; Lavery, L.A. Skin Temperature Monitoring Reduces the Risk for Diabetic Foot Ulceration in High-Risk Patients. American Journal of Medicine 2007, 120, 1042–1046, doi:10.1016/j.amjmed.2007.06.028.

73. Mori, T.; Nagase, T.; Takehara, K.; Oe, M.; Ohashi, Y.; Amemiya, A.; Noguchi, H.; Ueki, K.; Kadowaki, T.; Sanada, H. Morphological Pattern Classification System for Plantar Thermography of Patients with Diabetes. Journal of Diabetes Science and Technology 2013, 7, 1102–1112, doi:10.1177/193229681300700502.

74. Bayareh Mancilla, R.; Daul, C.; Gutierrez-Martínez, J.; Vera Hernández, A.; Wolf, D.; Leija Salas, L. Detection of Sore-Risk Regions on the Foot Sole with Digital Image Processing and Passive Thermography in Diabetic Patients. 17th International Conference on Electrical Engineering, Computing Science and Automatic Control (CCE) 2020.

75. Maldonado, H.; Bayareh, R.; Torres, I.A.; Vera, A.; Gutiérrez, J.; Leija, L. Automatic Detection of Risk Zones in Diabetic Foot Soles by Processing Thermographic Images Taken in an Uncontrolled Environment. Infrared Physics and Technology 2020, 105, 103187, doi:10.1016/j.infrared.2020.103187.

76. Torres, I.A.; Leija, L.; Vera, A.; Maldonado, H.; Bayareh, R.; Gutierrez, J.; Ramos, A. Computational Support System for Early Diagnosis of Diabetic Foot. 2018 Global Medical Engineering Physics Exchanges/Pan American Health Care Exchanges, GMEPE/PAHCE 2018 2018, 1–5, doi:10.1109/GMEPE-PAHCE.2018.8400743.

77. Netten, J.J.V.; Clark, D.; Lazzarini, P.A.; Janda, M.; Reed, L.F. The Validity and Reliability of Remote Diabetic Foot Ulcer Assessment Using Mobile Phone Images. Scientific Reports 2017, 7, 1–10, doi:10.1038/s41598-017-09828-4.

78. Jones, B.F. A Reappraisal of the Use of Infrared Thermal Image Analysis in Medicine. IEEE Transactions on Medical Imaging 1998, 17, 1019–1027, doi:10.1109/42.746635.

79. Webb, S. The Physics of Medical Imaging. 2010, 633.

80. Steketee, J. Spectral Emissivity of Skin and Pericardium. Physics in Medicine and Biology 1973, 18, doi:10.1088/0031-9155/18/5/307.

81. Martínez, H.R.; Rangel-Guerra, R.A.; Marfil-Rivera, A.; Muñiz, C.E.; Sagastegui, A. Cost of Stroke in Mexico. Journal of Stroke and Cerebrovascular Diseases 1995, 5, 244–247, doi:10.1016/S1052-3057(10)80198-3.

82. Muniz, P.R.; Cani, S.P.N.; da S. Magalhaes, R. Influence of Field of View of Thermal Imagers and Angle of View on Temperature Measurements by Infrared Thermovision. IEEE Sensors Journal 2014, 14, 729–733, doi:10.1109/JSEN.2013.2287003.

83. Watmough, D.J.; Fowler, P.W.; Oliver, R. The Thermal Scanning of a Curved Isothermal Surface: Implications for Clinical Thermography. Physics in Medicine and Biology 1970, 15, 1–8, doi:10.1088/0031-9155/15/1/301.

84. O'Dell, W.G.; Gormaley, A.K.; Prida, D.A. Validation of the Gatortail Method for Accurate Sizing of Pulmonary Vessels from 3D Medical Images: Medical Physics 2017, 44, doi:10.1002/mp.12580.

85. Chernov, G.; Chernov, V.; Dávila-Peralta, C.; Rodriquez-Carvajal, R.; Barboza-Flores, M. 3D Dynamic Thermography System for Biomedical Applications.; 2016.

86. Moriya, T.; Roth, H.R.; Nakamura, S.; Oda, H.; Nagara, K.; Oda, M.; Mori, K. Unsupervised Segmentation of 3D Medical Images Based on Clustering and Deep Representation Learning.; 2018.

87. Sanches, I.J.; Brioschi, M.; Traple, F. 3D MRI/IR Imaging Fusion: A New Medically Useful Computer Tool. InfraMation 2007 Proceedings 2007.

88. Goudie, C.; Kinnin, J.; Bartellas, M.; Gullipalli, R.; Dubrowski, A. The Use of 3D Printed Vasculature for Simulation-Based Medical Education Within Interventional Radiology. Cureus 2019, doi:10.7759/cureus.4381.

89. Pasquali, P. History of Medical Photography. Photography in Clinical Medicine 2020, 47–72, doi:10.1007/978-3-030-24544-3_4.

90. Alfageme, F.; Pasquali, P. Doctors as Subjects: Medical Photography as Personal Branding. In Photography in Clinical Medicine; Springer International Publishing, 2020; pp. 91–95.

91. Diakides, N.A.; Bronzino, J.D. Medical Infrared Imaging; 2008;

92. Mutluoglu, M.; Lipsky, B.A. Non-Surgical Treatment of Diabetic Foot Osteomyelitis. The Lancet Diabetes & Endocrinology 2017, 5, 668, doi:10.1016/S2213-8587(16)30141-3.

93. Gao, X.W.; Qian, Y.; Hui, R. The State of the Art of Medical Imaging Technology: From Creation to Archive and Back. The Open Medical Informatics Journal 2012, 5, 73–85, doi:10.2174/1874431101105010073.

94. Bayareh Mancilla, R.; Trujillo Romero, C.; Gutierrez Velazco, M.I.; Wolf, D.; Hernandez, A.V.; Leija Salas, L. 3D Multilayer Foot Model Based on CT Medical Imaging Processing for the Study of the Diabetic Foot Complication. 2018 15th International Conference on Electrical Engineering, Computing Science and Automatic Control, CCE 2018 2018, 3–8, doi:10.1109/ICEEE.2018.8533941.

95. Bronzino, J.D.; Peterson, D.R. The Biomedical Engineering Handbook; 2018;

96. Toledo Peral, C.L.; Ramos Becerril, F.J.; Vega Martínez, G.; Vera Hernández, A.; Leija Salas, L.; Gutiérrez Martínez, J. An Application for Skin Macules Characterization Based on a 3-Stage Image-Processing Algorithm for Patients with Diabetes. Journal of Healthcare Engineering 2018, doi:10.1155/2018/9397105.

97. Sanches, I.J.; Gamba, H.R.; de Souza, M.A.; Neves, E.B.; Nohama, P. Fusão 3D de Imagens de MRI/CT e Termografia. Revista Brasileira de Engenharia Biomedica 2013, 29, doi:10.4322/rbeb.2013.031.

98. Abreu de Souza, M.; Krefer, A.G.; Benvenutti Borba, G.; Mezzadri Centeno, T.; Remigio Gamba, H. Combining 3D Models with 2D Infrared Images for Medical Applications. In Proceedings of the 2015 37th Annual International Conference of the IEEE Engineering in Medicine and Biology Society (EMBC); IEEE, August 2015; pp. 2395–2398.

99. Negrín Díaz, M.L. 3D Photography. In Photography in Clinical Medicine; Springer International Publishing, 2020; pp. 527–536.

100. Reiter, O.; Halpern, A.C. Imaging Archives for Teaching, Learning, and Research. In Photography in Clinical Medicine; Springer International Publishing, 2020; pp. 585–590.

101. Phan, T.B. On the 3D Hollow Organ Cartography Using 2D Endoscopic Images, University of Lorraine, 2020.

102. Phan, T.B.; Trinh, D.H.; Wolf, D.; Daul, C. Optical Flow-Based Structure-from-Motion for the Reconstruction of Epithelial Surfaces. Pattern Recognition 2020, doi:10.1016/j.patcog.2020.107391.

103. Wulf, J.; Vitt, K.D.; Gehl, H.B.; Busch, L.C. Anatomical Accuracy in Medical 3D Modeling. In Proceedings of the Studies in Health Technology and Informatics; 2001; Vol. 81, pp. 584–586.

104. Rayner, J.E.; Laino, A.M.; Nufer, K.L.; Adams, L.; Raphael, A.P.; Menzies, S.W.; Soyer, H.P. Clinical Perspective of 3D Total Body Photography for Early Detection and Screening of Melanoma. Frontiers in Medicine 2018, 5, 152, doi:10.3389/FMED.2018.00152.

105. Jinnin, M.; Fukushima, S.; Masuguchi, S.; Tanaka, H.; Kawashita, Y.; Ishihara, T.; Ihn, H. Evaluation of

Usefulness of 3D Views for Clinical Photography. BioScience Trends 2011, 5, 211–216, doi:10.5582/BST.2011.V5.5.211.

106. Phan, T.B.; Trinh, Di.H.; Lamarque, D.; Wolf, D.; Daul, C. Dense Optical Flow for the Reconstruction of Weakly Textured and Structured Surfaces: Application to Endoscopy. In Proceedings of the Proceedings - International Conference on Image Processing, ICIP; 2019; Vol. 2019-Septe, pp. 310–314.

107. Miranda-Luna, R.; Daul, C.; Blondel, W.C.P.M.; Hernandez-Mier, Y.; Wolf, D.; Guillemin, F. Mosaicing of Bladder Endoscopic Image Sequences: Distortion Calibration and Registration Algorithm. IEEE Transactions on Biomedical Engineering 2008, 55, 541–553, doi:10.1109/TBME.2007.903520.

108. González-Pérez, S.; Ström, D.P.; Arteaga-Marrero, N.; Luque, C.; Sidrach-Cardona, I.; Villa, E.; Ruiz-Alzola, J. Assessment of Registration Methods for Thermal Infrared and Visible Images for Diabetic Foot Monitoring. Sensors 2021, 21, doi:10.3390/s21072264.

109. Loredo, R.A.; Garcia, G.; Chhaya, S. Medical Imaging of the Diabetic Foot. Clinics in Podiatric Medicine and Surgery 2007.

110. Speakman, J.R.; Ward, S. Infrared Thermography: Principles and Applications. Zoology 1998, 101, 224–232.

111. Bayareh, R.; Vera, A.; Leija, L.; Gutierrez-Martinez, J. Programming of a System for the Acquisition of Images and Thermographic Data for the Diabetic Foot Analysis. 2017 14th International Conference on Electrical Engineering, Computing Science and Automatic Control, CCE 2017 2017, 2–8, doi:10.1109/ICEEE.2017.8108866.

112. Kaczmarek, M.; Nowakowski, A. Active IR-Thermal Imaging in Medicine. Journal of Nondestructive Evaluation 2016, 35, 1–16, doi:10.1007/s10921-016-0335-y.

113. Rogalski, A. History of Infrared Detectors. Opto-electronics Review 2012, 20, 279–308, doi:10.2478/s11772-012-0037-7.

114. Pascoe, D.D.; Mercer, J.B.; De Weerd, L. Physiology of Thermal Signals. In Medical Devices and Systems; 2006; pp. 21-1-21–20 ISBN 9781420003864.

115. Nowakowski, A. Quantitative Active Dynamic Thermal IR-Imaging and Thermal Tomography in Medical Diagnostics. In Medical Infrared Imaging: Principles and Practices; 2012; pp. 7-1-7–30 ISBN 9781439872505.

116. Electro-Optical System (Part I) – Aircraft 101 Available online: https://basicsaboutaerodynamicsandavionics.wordpress.com/2017/02/22/electro-optical-systems/ (accessed on 28 October 2021).

117. Prototipo Para La Cuantificación Térmica de Zonas de La Planta Del Pie Diabético Available online: https://repositorio.cinvestav.mx/handle/cinvestav/2673 (accessed on 28 October 2021).

118. Oxide, V.; Silicon, A.; Titanate, B.S. Uncooled Detectors for Thermal Imaging Cameras Uncooled Detectors : A Brief History. Read 1970.

119. Rogalski, Antoni. Infrared Detectors. 2011, 876.

120. Ring, F. The Herschel Heritage to Medical Thermography. Journal of Imaging 2016, 2, doi:10.3390/JIMAGING2020013.

121. Ma, J.; Ma, Y.; Li, C. Infrared and Visible Image Fusion Methods and Applications: A Survey. Information Fusion 2019, 45, 153–178, doi:10.1016/j.inffus.2018.02.004.

122. PureThermal 2 - FLIR Lepton Smart I/O Module by GetLab | GroupGets Available online: https://groupgets.com/manufacturers/getlab/products/purethermal-2-flir-lepton-smart-i-o-module (accessed on 15 November 2021).

123. Ring, E.F.J. The Historical Development of Thermal Imaging in Medicine. Rheumatology 2004, 43, 800–802, doi:10.1093/rheumatology/keg009.

124. Ring, E.F.J.; Ammer, K.; Jung, A.; Murawski, P.; Wiecek, B.; Zuber, J.; Zwolenik, S.; Plassmann, P.; Jones, C.; Jones, B.F. Standardization of Infrared Imaging. Annual International Conference of the IEEE Engineering in Medicine and Biology - Proceedings 2004, 26 II, 1183–1185, doi:10.1109/iembs.2004.1403378.

125. Fidali, M.; Mikulski, M. An Inexpensive Blackbody Model. 2008, doi:10.21611/qirt.2008.14_01_04.

126. Watmough, D.J.; Oliver, R. Emissivity of Human Skin in Vivo between 2.0 and 5.4 Measured at Normal Incidence. Nature 1968, 218, 885–886.

127. Bernard, V.; Staffa, E.; Mornstein, V.; Bourek, A. Infrared Camera Assessment of Skin Surface Temperature – Effect of Emissivity. Physica Medica 2013, 29, 583–591, doi:10.1016/J.EJMP.2012.09.003.

128. Pavelek, M.; Janotkova, E. Teorie a Praxe Termovizních Merení (Theory of Thermovision Measurement). Brno: TESTO 2008, 1–49.

129. Arnon, B.; Oria, K.; Arieli, Y. Correction of the Angular Emissivity of Human Skin for Clinical Thermal Imaging. Imaging Medicine 2017, 9, 103–108.

130. Cheng, T.Y.; Deng, D.; Herman, C. Curvature Effect Quantification for In-Vivo IR Thermography. In Proceedings of the ASME International Mechanical Engineering Congress and Exposition, Proceedings (IMECE); American Society of Mechanical Engineers, November 9 2012; Vol. 2, pp. 127–133.

131. Arnon, B.; Oria, K.; Arieli, Y. Correction of the Angular Emissivity of Human Skin for Clinical Thermal Imaging. Imaging Medicine 2017, 9, 103–108.

132. Stefan–Boltzmann Constant. In The IUPAC Compendium of Chemical Terminology; 2008.

133. Liu, C.; van der Heijden, F.; Klein, M.E.; van Baal, J.G.; Bus, S.A.; van Netten, J.J. Infrared Dermal Thermography on Diabetic Feet Soles to Predict Ulcerations: A Case Study. Advanced Biomedical and Clinical Diagnostic Systems XI 2013, 8572, 85720N, doi:10.1117/12.2001807.

134. Fraiwan, L.; AlKhodari, M.; Ninan, J.; Mustafa, B.; Saleh, A.; Ghazal, M. Diabetic Foot Ulcer Mobile Detection System Using Smart Phone Thermal Camera: A Feasibility Study. BioMedical Engineering Online 2017, 16, 1–19, doi:10.1186/s12938-017-0408-x.

135. Do I Need a Blackbody for Skin Temperature Screening? | Teledyne FLIR Available online: https://www.flir.com/discover/public-safety/do-i-need-a-blackbody-for-skin-temperature-screening/ (accessed on 17 August 2021).

136. Ring, E.F.J.; Ammer, K. Infrared Thermal Imaging in Medicine. Physiological Measurement 2012, 33.

137. Nowakowski, A.; Kaczmarek, M.; Renkielska, A.; Grudziński, J.; Stojek, J. Heating or Cooling to Increase Contrast in Thermographic Diagnostics. Annual International Conference of the IEEE Engineering in Medicine and Biology - Proceedings 2002, 2, 1137–1138, doi:10.1109/iembs.2002.1106314.

138. Renkielska, A.; Nowakowski, A.; Kaczmarek, M.; Ruminski, J. Burn Depths Evaluation Based on Active Dynamic IR Thermal Imaging-A Preliminary Study. Burns 2006, 32, 867–875, doi:10.1016/j.burns.2006.01.024.

139. Edis, E.; Flores-Colen, I.; De Brito, J. Passive Thermographic Detection of Moisture Problems in Façades with Adhered Ceramic Cladding. Construction and Building Materials 2014, doi:10.1016/j.conbuildmat.2013.10.085.

140. Bücking, T.M.; Hill, E.R.; Robertson, J.L.; Maneas, E.; Plumb, A.A.; Nikitichev, D.I. From Medical Imaging Data to 3D Printed Anatomical Models. PLoS ONE 2017, 12, 1–10, doi:10.1371/journal.pone.0178540.

141. Gonzalez, R.C.; Woods, R.E.; Masters, B.R. Digital Image Processing, Third Edition. Journal of Biomedical Optics 2009, doi:10.1117/1.3115362.

142. Gonzalez, R.C.; Woods, R.E.; Eddins, S.L. Digital Image Processing Using Matlab - Gonzalez Woods & Eddins.Pdf. Education 2004.

143. Muthukrishnan R; Radha, M. EDGE DETECTION TECHNIQUES FOR IMAGE SEGMENTATION. International Journal of Computer Science & Information Technology (IJCSIT) 2011, 3, doi:10.5121/ijcsit.2011.3620.

144. Maier, A. (Andreas K.); Steidl, S.; Christlein, V.; Hornegger, J. Medical Imaging Systems : An Introductory Guide. 264.

145. Szeliski, R. Computer Vision : Algorithms and Applications. 2011, 812.

146. Assignment: Compare the Techniques of Different Region. | Image Processing and Pattern Recognition 2012 Available online: https://imageprocessing2012.wordpress.com/2012/05/01/147/ (accessed on 31 October 2021).

147. Schindelin, J.; Arganda-Carreras, I.; Frise, E.; Kaynig, V.; Longair, M.; Pietzsch, T.; Preibisch, S.; Rueden, C.; Saalfeld, S.; Schmid, B.; et al. Fiji: An Open-Source Platform for Biological-Image Analysis. Nature Methods 2012, 9, 676–682, doi:10.1038/NMETH.2019.

148. Otsu, N. THRESHOLD SELECTION METHOD FROM GRAY-LEVEL HISTOGRAMS. IEEE Trans Syst Man Cybern 1979, doi:10.1109/TSMC.1979.4310076.

149. da Silva, I.N. Artificial Neural Networks: A Practice Course; 1st ed.; Springer Publishing Company, 2016; ISBN 3319431617.

150. Hernández, A.; Arteaga-Marrero, N.; Villa, E.; Fabelo, H.; Callicó, G.M.; Ruiz-Alzola, J. Automatic Segmentation Based on Deep Learning Techniques for Diabetic Foot Monitoring through Multimodal Images. In Proceedings of the Lecture Notes in Computer Science (including subseries Lecture Notes in Artificial Intelligence and Lecture Notes in Bioinformatics); Springer Verlag, 2019; Vol. 11752 LNCS, pp. 414–424.

151. González-Aguilera, D.; Rodriguez-Gonzalvez, P.; Armesto, J.; Lagüela, S. Novel Approach to 3D Thermography and Energy Efficiency Evaluation. Energy and Buildings 2012, 54, 436–443, doi:10.1016/j.enbuild.2012.07.023.

152. Wu, L.; Zhou, W.; Wan, X.; Zhang, J.; Shen, L.; Hu, S.; Ding, Q.; Mu, G.; Yin, A.; Huang, X.; et al. A Deep Neural Network Improves Endoscopic Detection of Early Gastric Cancer without Blind Spots. Endoscopy 2019, doi:10.1055/a-0855-3532.

153. Goyal, M.; Reeves, N.D.; Rajbhandari, S.; Yap, M.H. Robust Methods for Real-Time Diabetic Foot Ulcer Detection and Localization on Mobile Devices. IEEE Journal of Biomedical and Health Informatics 2019, doi:10.1109/JBHI.2018.2868656.

154. Vardasca, R.; Magalhaes, C.; Seixas, A.; Carvalho, R.; Mendes, J. Diabetic Foot Monitoring Using Dynamic Thermography and AI Classifiers.; 2019.

155. Magalhaes, C.; Vardasca, R.; Mendes, J. Classifying Skin Neoplasms with Infrared Thermal Images. 2018, doi:10.21611/QIRT.2018.013.

156. Mancilla, R.B.; Lorraine, U. De; Hernández, A.V.; Wolf, D.; Lorraine, U. De Detection of Sore-Risk Regions on the Sole with Digital Image Processing and Passive Thermography in Diabetic Patients.

157. Cardone, D.; Pinti, P.; Di Donato, L.; Merla, A. Warping-Based Co-Registration of Thermal Infrared Images: Study of Factors Influencing Its Applicability. Infrared Physics and Technology 2017, 83, 142–155, doi:10.1016/j.infrared.2017.04.020.

158. Flir Lepton - Grupos de Google Available online: https://groups.google.com/g/flir-lepton?pli=1 (accessed on 1 July 2021).

159. The Benefits and Challenges of Radiometric Thermal Technology | Teledyne FLIR Available online: https://www.flir.com/discover/security/radiometric/the-benefits-and-challenges-of-radiometric-thermal-technology/ (accessed on 1 November 2021).

160. Villa, E.; Arteaga-Marrero, N.; Ruiz-Alzola, J. Performance Assessment of Low-Cost Thermal Cameras for Medical Applications. Sensors (Switzerland) 2020, 20, doi:10.3390/s20051321.

161. Yang, M. Der; Su, T.C.; Lin, H.Y. Fusion of Infrared Thermal Image and Visible Image for 3D Thermal Model Reconstruction Using Smartphone Sensors. Sensors (Switzerland) 2018, 18, doi:10.3390/s18072003.

162. Fischler, M.A.; Bolles, R.C. Random Sample Consensus: A Paradigm for Model Fitting With. Communications of the ACM 1981.

163. Saiti, E.; Theoharis, T. An Application Independent Review of Multimodal 3D Registration Methods. Computers and Graphics (Pergamon) 2020, 91, 153–178, doi:10.1016/j.cag.2020.07.012.

164. Zhang, Y.; Zhang, X.; Maybank, S.J.; Yu, R. An IR and Visible Image Sequence Automatic Registration Method Based on Optical Flow. Machine Vision and Applications 2013, 24, 947–958, doi:10.1007/s00138-012-0465-x.

165. Dice, L.R.; Dice, L.R. Measures of the Amount of Ecologic Association Between Species. Ecology 1945, 26, 297–302, doi:10.2307/1932409.

166. Chung, N.C.; Miasojedow, B.Z.; Startek, M.; Gambin, A. Jaccard/Tanimoto Similarity Test and Estimation Methods for Biological Presence-Absence Data. BMC Bioinformatics 2019, 20, 644, doi:10.1186/s12859-019-3118-5.

167. Ju, X.; Nebel, J.-C.; Siebert, J.P. 3D Thermography Imaging Standardization Technique for Inflammation Diagnosis. Infrared Components and Their Applications 2005, 5640, 266, doi:10.1117/12.577055.

168. Short, D.J.; Zgonis, T. Medical Imaging in Differentiating the Diabetic Charcot Foot from Osteomyelitis. Clinics in Podiatric Medicine and Surgery 2017.

169. Schonberger, J.L.; Frahm, J.-M. Structure-from-Motion Revisited. In Proceedings of the 2016 IEEE Conference on Computer Vision and Pattern Recognition (CVPR); IEEE, June 2016; pp. 4104–4113.

170. Kazhdan, M.; Hoppe, H. Screened Poisson Surface Reconstruction. ACM Transactions on Graphics 2013.

171. Cernea, D. Multi-View Stereo Reconstruction Library Available online: https://cdcseacave.github.io/openMVS.

172. Torres, J.; Arroyo, G.; Romo, C.; Haro, J. De 3D Digitization Using Structure from Motion. Academia.Edu 2012.

173. Bianco, S.; Ciocca, G.; Marelli, D. Evaluating the Performance of Structure from Motion Pipelines. Journal of Imaging 2018, 4, 1–18, doi:10.3390/jimaging4080098.

174. Schoenberger, J.L. Camera Models Available online: https://colmap.github.io/cameras.html.

175. Özyeşil, O.; Voroninski, V.; Basri, R.; Singer, A. A Survey of Structure from Motion. Acta Numerica 2017, 26, 305–364, doi:10.1017/S096249291700006X.

176. Fischler, M.A.; Bolles, R.C. Random Sample Consensus: A Paradigm for Model Fitting with Applications to Image Analysis and Automated Cartography. Communications of the ACM 1981, 24, 381–395, doi:10.1145/358669.358692.

177. Triggs, B.; McLauchlan, P.F.; Hartley, R.I.; Fitzgibbon, A.W. Bundle Adjustment — A Modern Synthesis. Lecture Notes in Computer Science (including subseries Lecture Notes in Artificial Intelligence and Lecture Notes in Bioinformatics) 1999, 1883, 298–372, doi:10.1007/3-540-44480-7_21.

178. Hernández, C.; Furukawa, Y. Multi-View Stereo : A Tutorial. Computer Graphics and Vision2 2013, 9, 1–148.

179. Rakotosaona, M.J.; La Barbera, V.; Guerrero, P.; Mitra, N.J.; Ovsjanikov, M. PointCleanNet: Learning to Denoise and Remove Outliers from Dense Point Clouds. Computer Graphics Forum 2019, 39, 185–203, doi:10.1111/cgf.13753.

180. Waechter, M.; Moehrle, N.; Goesele, M. Let There Be Color! Large-Scale Texturing of 3D Reconstructions. Lecture Notes in Computer Science (including subseries Lecture Notes in Artificial Intelligence and Lecture Notes in Bioinformatics) 2014, 8693 LNCS, 836–850, doi:10.1007/978-3-319-10602-1_54.

181. Kaczmarek, M.; Nowakowski, A. Active Dynamic Thermography in Medical Diagnostics. 2017, 291–310, doi:10.1007/978-981-10-3147-2_17.

182. Bayareh Mancilla, R.; Daul, C.; Martinez, J.G.; Salas, L.L.; Wolf, D.; Hernandez, A.V. A Quantitative Method for the Detection of Temperature Differences on the Sole of the Foot in Diabetic Patients. In Proceedings of the Pan American Health Care Exchanges, PAHCE; IEEE, March 15 2021; Vol. 2021-May, pp. 1–5.

183. Fluke Ti32 Infrared Camera | Fluke Available online: https://www.fluke.com/en-us/product/thermal-cameras/ti32 (accessed on 18 May 2022).

184. Haake P5 Circulating Bath w/ Thermo C10 Controller | Marshall Scientific Available online: https://www.marshallscientific.com/Haake-P5-Circulating-Bath-w-Thermo-C10-Controller-p/h-p5.htm (accessed on 18 May 2022).

185. Research Ethics Review Committee Available online: https://www.who.int/groups/research-ethics-review-committee/guidelines-on-submitting-research-proposals-for-ethics-review/templates-for-informed-consent-forms (accessed on 19 August 2021).

186. Litwa, M. Influence of Angle of View on Temperature Measurements Using Thermovision Camera. IEEE Sensors Journal 2010, 10, doi:10.1109/JSEN.2010.2045651.

187. Stojcsics, D.; Lovas, I.; Domozi, Z.; Molnar, A. High Resolution 3D Thermal Imaging Using FLIR DUO R Sensor. In Proceedings of the INES 2018 - IEEE 22nd International Conference on Intelligent Engineering Systems, Proceedings; Institute of Electrical and Electronics Engineers Inc., November 5 2018; pp. 000311–000316.

188. Beaudducel, F. READIS2: Import IS2 Files (Fluke Infrared Camera) Available online: https://www.mathworks.com/matlabcentral/%0Afileexchange/32352-readis2-import-is2-files-fluke-infrared-camera (accessed on 10 December 2019).

189. Theodorakeas, P.; Cheilakou, E.; Ftikou, E.; Koui, M. Passive and Active Infrared Thermography: An Overview of Applications for the Inspection of Mosaic Structures. Journal of Physics: Conference Series 2015, 655, doi:10.1088/1742-6596/655/1/012061.

190. Kavuru, M.; Rosina, E. Developing Guidelines for the Use of Passive Thermography on Cultural Heritage in Tropical Climates. Applied Sciences (Switzerland) 2020, 10, 1–9, doi:10.3390/app10238411.

191. Saiti, E.; Theoharis, T. An Application Independent Review of Multimodal 3D Registration Methods. Computers and Graphics (Pergamon) 2020, 91, 153–178, doi:10.1016/j.cag.2020.07.012.

192. Fiedler, D.; Müller, H. Impact of Thermal and Environmental Conditions on the Kinect Sensor. Lecture Notes in Computer Science (including subseries Lecture Notes in Artificial Intelligence and Lecture Notes in Bioinformatics) 2012, 7854 LNCS, 21–31, doi:10.1007/978-3-642-40303-3_3.

193. Tisha, S.M. Thermal-Kinect Fusion Scanning System for Bodyshape Inpainting and Estimation under Clothing. LSU Master's Theses 2019.

194. Lachat, E.; Macher, H.; Mittet, M.A.; Landes, T.; Grussenmeyer, P. First Experiences with Kinect V2 Sensor for Close Range 3D Modelling. International Archives of the Photogrammetry, Remote Sensing and Spatial Information Sciences - ISPRS Archives 2015, 40, 93–100, doi:10.5194/isprsarchives-XL-5-W4-93-2015.

195. Rangel, J.; Soldan, S. 3D Thermal Imaging: Fusion of Thermography and Depth Cameras. In Proceedings of the Conf. Quant. InfraRed Thermogr.; 2014.

196. Posada, R.; Daul, C.; Wolf, D.; Aletti, P. Towards a Noninvasive Intracranial Tumor Irradiation Using 3D Optical Imaging and Multimodal Data Registration. International Journal of Biomedical Imaging 2007, 2007,

doi:10.1155/2007/62030.

197. Trinh, D.H.; Daul, C.; Blondel, W.; Lamarque, D. Mosaicing of Images with Few Textures and Strong Illumination Changes: Application to Gastroscopic Scenes. In Proceedings of the Proceedings - International Conference on Image Processing, ICIP; 2018.

198. Hartley, R.; Zisserman, A. Multiple View Geometry in Computer Vision; 2004;

199. Peng, K.; Chen, X.; Zhou, D.; Liu, Y. 3D Reconstruction Based on SIFT and Harris Feature Points. In Proceedings of the 2009 IEEE International Conference on Robotics and Biomimetics, ROBIO 2009; 2009; pp. 960–964.

200. Rey-Otero, I.; Delbracio, M. Anatomy of the SIFT Method. Image Processing On Line 2014, 4, 370–396, doi:10.5201/ipol.2014.82.

201. Gauglitz, S.; Höllerer, T.; Turk, M.; Gauglitz, S.; Höllerer, T.; Turk, · M; Turk, M. Evaluation of Interest Point Detectors and Feature Descriptors for Visual Tracking. Int J Comput Vis 2011, 94, 335–360, doi:10.1007/s11263-011-0431-5.

202. Low, D.G. Distinctive Image Features from Scale-Invariant Keypoints. International Journal of Computer Vision 2004, 91–110.

203. SIFT(Scale-Invariant Feature Transform) | by Minghao Ning | Towards Data Science Available online: https://towardsdatascience.com/sift-scale-invariant-feature-transform-c7233dc60f37 (accessed on 22 May 2022).

204. SIFT - Scale-Invariant Feature Transform Available online: http://weitz.de/sift/index.html (accessed on 5 September 2021).

205. Hartley, R.; Zisserman, A. Epipolar Geometry and the Fundamental Matrix. Multiple View Geometry in Computer Vision 2011, 239–261, doi:10.1017/cbo9780511811685.014.

206. Fischler, M.A.; Bolles, R.C. Random Sample Consensus: A Paradigm for Model Fitting With. Communications of the ACM 1981.

207. Bujnak, M.; Kukelova, Z.; Pajdla, T. A General Solution to the P4P Problem for Camera with Unknown Focal Length. 26th IEEE Conference on Computer Vision and Pattern Recognition, CVPR 2008, doi:10.1109/CVPR.2008.4587793.

208. Irschara, A.; Zach, C.; Frahm, J.-M.; Bischof, H. From Structure-from-Motion Point Clouds to Fast Location Recognition. 2010, 2599–2606, doi:10.1109/CVPR.2009.5206587.

209. Hartley, R.; Zisserman, A. Multiple View Geometry in Computer Vision. Multiple View Geometry in Computer Vision 2004, doi:10.1017/CBO9780511811685.

210. Vu, H.H.; Labatut, P.; Pons, J.P.; Keriven, R. High Accuracy and Visibility-Consistent Dense Multiview Stereo. IEEE Transactions on Pattern Analysis and Machine Intelligence 2012, 34, 889–901, doi:10.1109/TPAMI.2011.172.

211. Fu, Y.; Yan, Q.; Yang, L.; Liao, J.; Xiao, C. Texture Mapping for 3D Reconstruction with RGB-D Sensor.

212. Abayowa, B. ReadObj Function for Matlab Available online: https://www.mathworks.com/matlabcentral/fileexchange/18957-readobj.

213. Shen, S. Accurate Multiple View 3D Reconstruction Using Patch-Based Stereo for Large-Scale Scenes. IEEE *TRANSACTIONS ON IMAGE PROCESSING* **2013**, *22*, doi:10.1109/TIP.2013.2237921.